A STUDY OF THE EFFECT OF THE 3.10-MEV STATE OF F^{17} ON THE $O^{16}(p,\gamma)F^{17}$ REACTION

Thesis by

John J. Domingo

In Partial Fulfillment of the Requirements

For the Degree of

Doctor of Philosophy

California Institute of Technology

Pasadena, California

1963

ACKNOWLEDGMENTS

The author would like to express his gratitude to the staff of the Kellogg Radiation Laboratory for their assistance during the course of this work. He is especially indebted to Dr. Neil Tanner now of the Clarendon Laboratory, Oxford, England for suggesting the problem, and to Professor T. Lauritsen for his constant interest and guidance. The author would also like to thank Dr. T. Tombrello for providing the computer program for the computation of the capture matrix elements, and to Barbara Zimmerman for her help in the analysis of the experimental data. It is a pleasure to acknowledge the assistance of Mr. J. D. Pearson without whose unfailing aid during the weary months of accelerator maintenance this experiment could never have been brought to fruition.

The author is also grateful for the graduate fellowships received from the National Science Foundation and for the financial support of this research project by a joint program of the Office of Naval Research and the U.S. Atomic Energy Commission.

ABSTRACT

The yield of the two capture gamma rays in the $O^{16}(p,\gamma)F^{17}$ reaction has been measured at 90° to the beam for bombarding energies in the range 2.56 - 2.76 MeV. An anomaly was observed in the yield of the capture gamma ray leading to the .500 MeV $\frac{1}{2}^+$ state of F^{17} for a bombarding energy of approximately 2.66 MeV corresponding to the 3.10 MeV state of F^{17}. No anomaly was observed in the yield of the capture gamma ray leading to the $\frac{5}{2}^+$ ground state of F^{17}. The experimental results were found to be in good agreement with theoretical calculations made on the basis of the extranuclear capture model of Christy and Duck (1961). On the basis of the experimental results and the theoretical calculations, the single particle reduced widths for the $\frac{1}{2}^+$ .500 MeV state and the $\frac{5}{2}^+$ ground state of F^{17} were obtained. Using the definition of Lane (1958), these single particle reduced widths were found to be:

$$\theta^2_{\frac{1}{2}^+sp} = .57 \pm .10 \qquad \theta^2_{\frac{5}{2}^+sp} = .38 \pm .08$$

From the shape of the anomaly observed in the yield of the capture gamma ray leading to the $\frac{1}{2}^+$ state and the extranuclear calculations, an upper limit was placed upon the width of the gamma ray transition leading from the resonant $\frac{1}{2}^-$ state at 3.10 MeV to the $\frac{1}{2}^+$ .500 MeV state. This limit was: $\Gamma_\gamma < .03$ eV

TABLE OF CONTENTS

I. INTRODUCTION

In many light nuclei the cross section for the (p,γ) reaction consists of a slowly varying background upon which the various resonances in the reaction are superposed. The characteristic magnitude of this slowly varying background is approximately 1 microbarn for 1 MeV protons, and in many cases the gamma-ray angular distribution has the simple $\sin^2\theta$ form characteristic of a dipole transition with no change of magnetic quantum number. In several cases this $\sin^2\theta$ distribution can be attributed to a P to S electric dipole transition with no spin flip, and this simple angular distribution together with the smoothly varying character of the cross section leads to the description of the reaction as a direct capture process.

Christy and Duck (1961) have shown that in several cases a simple extranuclear model for the electric dipole capture shows good agreement with the experimental data. In this model the capture matrix elements are approximated by only that portion contributed by configurations in which the proton is outside the nuclear potential of the capturing nucleus. For these configurations the only interaction between the two particles is just the Coulomb one, and the wave functions involve only the well known Coulomb functions. The absence of a nuclear interaction in the initial state accounts for the smoothly varying character of the cross section and also for the absence of spin flip and the resultant $\sin^2\theta$ distribution in the case of P to S capture.

The success of the model at low bombarding energies is not surprising since calculations show that the integrand of the capture matrix element

has a maximum at a distance considerably larger than the nuclear radius. Thus, the behavior of the correct wave functions in the vicinity of the nuclear surface is not very important, and the approximation made in replacing them with Coulomb functions up to some cutoff radius is reasonably good. At higher bombarding energies the model might be expected to deviate from the experimental data since the maximum in the integrand of the matrix elements will move closer to the nuclear surface and the behavior of the correct wave functions in the vicinity of the nuclear surface will therefore become more important. Thus, once the validity of the model had been reasonably well established at low bombarding energies, it was interesting to test it at higher energies.

The extranuclear calculations are in good agreement with the low energy measurements of the $O^{16}(p,\gamma)F^{17}$ cross section (Tanner, 1959; Christy, 1961; Lal, 1962), and the possibility of clarifying a rather puzzling situation concerning the interference between the direct and resonant capture made this a particularly interesting case to investigate at a higher bombarding energy. The energy levels of F^{17} are shown in Fig. 1 which was taken from the compilation of Ajzenberg-Selove and Lauritsen (1959). Analysis of the elastic scattering of protons from O^{16} has shown (Salisbury and Richards, 1962) that the 3.10-MeV state of F^{17} has a spin and parity of $\frac{1}{2}^-$. In this analysis it was found possible to obtain good agreement with the elastic scattering data in the region of the 3.10-MeV state by using only a resonant $P_{\frac{1}{2}}$ phase shift and slowly varying $P_{\frac{3}{2}}$ and $S_{\frac{1}{2}}$ phase shifts. Capture to the .500-MeV $\frac{1}{2}^+$ state proceeds mainly by E1 radiation from the $P_{\frac{1}{2}}$ and $P_{\frac{3}{2}}$ partial waves; capture to the $\frac{5}{2}^+$ ground state proceeds

mainly by E1 radiation from the $P_{\frac{3}{2}}$, $F_{\frac{5}{2}}$, and $F_{\frac{7}{2}}$ partial waves. Thus, even on the basis of a purely extranuclear transition, one would expect an anomaly in the γ_2* cross section in the region of the 3.10-MeV state since the $P_{\frac{1}{2}}$ partial wave contains an additional term due to the resonant scattering. The γ_1* cross section, on the other hand, should show no anomaly since it does not proceed through the $P_{\frac{1}{2}}$ partial wave and there will be no additional resonant term in its matrix element.

The experimental results of Laubenstein et al. (1951), appear to be in disagreement with these conclusions since, within their experimental uncertainty, no anomaly was observed in the total capture cross section in the region of the 3.10-MeV state of F^{17}. The extranuclear model, however, predicts a definite anomaly calculable from the $O^{16}(p,p)$ elastic scattering phase shifts and the value of the F^{17} nuclear radius, and in general it is very difficult to see how some sort of anomaly could fail to be present. A preliminary calculation of the expected γ_2 anomaly showed that it would be mainly of the interference type, and that the magnitude of the anomaly should be approximately $\pm$ 25% of the nonresonant yield. The width of the 3.10-MeV state of F^{17} state as deduced from the resonance observed in the $O^{16}(p,p)$ elastic scattering at a bombarding energy of 2.66 MeV is approximately 20 keV. A study of the yield of the

---

*In the following discussion the capture gamma ray leading to the $\frac{5}{2}^+$ state of F^{17} will be denoted by γ_1; the capture gamma ray leading to the $\frac{1}{2}^+$ .500-MeV state of F^{17} will be denoted by γ_2, and the gamma ray leading from the $\frac{1}{2}^+$ state to the ground state of F^{17} will be denoted by γ_3.

two capture gamma rays at $\theta = 90°$ was therefore undertaken for bombarding energies in the range 2.56—2.76 MeV. Sufficiently long bombardments were used so that the expected statistical fluctuation in the γ_2 yield between the data points was only about 2% or less than 10% of the expected anomaly.

An anomaly of the type predicted by the extranuclear model was observed in the γ_2 yield, and, within the statistical uncertainty of approximately 10%, no anomaly was present in the measured γ_1 yield (see Figs. 8 and 9). Parts II and III of this thesis describe the measurement and analysis of the yield of the two capture gamma rays. In Part IV the experimental results are compared with the results predicted on the basis of the extranuclear model.

II. EXPERIMENTAL PROCEDURE

A. Introduction

Figure 2 shows a schematic view of the experimental arrangement. After being defined in energy and position, the beam enters the target chamber where it strikes a tungsten oxide target; the resultant radiation is detected by a NaI(Tl) scintillator set at 90° to the incident beam. In principle, the experimental procedure was quite straightforward; one simply measured the yield of the two capture gamma rays as the bombarding energy was stepped through the resonance region. In practice, however, because of the extremely small capture cross section, rather elaborate precautions had to be taken to reduce the background radiation to a sufficiently low level and to prevent target deterioration during the long bombardments required.

B. Target Chamber

The target chamber, shown in Fig. 3, consisted basically of a cylinder 3" in diameter and approximately 5" high fitted with entrance and exit beam tubes of 1" diameter. In order to increase the detection efficiency one side of the cylinder was cut away and replaced with a flat plate; this allowed the front face of the detector shield to approach to within approximately $\frac{5"}{8}$ of the center of the chamber. The use of fairly wide target blanks in order to achieve uniform oxidation and the need for a rather elaborate target support system to assure good heat transfer made closer approach to the center of the chamber difficult to achieve. To avoid the deposition of carbon on the target during the long bombardments, a relatively large liquid nitrogen cold trap was considered

necessary. The trap consisted of a semicircular chamber located directly opposite the counter face and subtending roughly the same solid angle when viewed from the target. This system proved to be quite effective, and even though the targets were held at a rather low temperature during the bombardments, there was no evidence of deposition of carbon on any of the targets.

During a preliminary study of the capture radiation, considerable difficulty had been experienced with a loss of oxygen from the targets during bombardment. This oxygen loss is thought to be due to a local heating phenomenon and will be discussed in greater detail in the section dealing with target preparation. These preliminary runs clearly demonstrated that it was desirable to cool the target during the bombardment. To provide this cooling, the target was connected by means of a $\frac{5}{8}$" diameter copper target rod with a cooling pot mounted outside the vacuum system. Several cooper cooling fins where attached to the target rod inside the cooling pot, and during the bombardments the pot was filled with a mixture of alcohol and water kept just at the freezing point by the periodic addition of liquid nitrogen. Good thermal contact between the target rod and the target blank was assured by clamping the blank firmly against the copper target support by means of a copper clamp. This clamp was provided with a rectangular opening to allow the beam to pass through it and strike the target.

The target rod assembly was held on the axis of the chamber but allowed to rotate about its own axis by means of a Lucite plug equipped with suitable O-Ring seals. This Lucite plug also served to insulate the target assembly electrically from the chamber so that the total bombarding

charge could be measured by means of a conventional current integrator. To prevent the escape of secondary electrons from the target, it was held at a positive potential of approximately 300 volts relative to the grounded chamber walls. Secondary electrons from the regulation slits were prevented from passing down the beam tube and being attracted to the positive target assembly by the use of a conventional guard electrode placed around the mouth of the beam tube and held at - 300 volts with respect to ground. A baffle was placed inside the beam tube to prevent protons scattered by the regulation slits from striking this guard electrode and creating secondary electrons which would then be attracted by the positive target potential. Careful checks of the leakage and secondary electron currents from the target assembly and the secondary electron current from the guard electrode showed that in normal operation they were all negligible.

Normally, the exit beam tube was closed by a cap containing a quartz disk upon which the beam spot could be observed. By turning the target so that it intercepted the beam edgewise, this quartz could be used to center the beam on the target. Then by means of a protractor fixed to the Lucite plug and a pointer attached to the target rod, the target—beam angle could be set to within 1°. By replacing the cap containing the quartz disk with an extension beam tube and pulling the target up out of the path of the beam, the beam could be allowed to pass through the chamber. The beam could then be stopped in some well shielded location sufficiently remote from the gamma-ray detector so that the radiation produced by stopping the beam was not detected. This procedure was very useful for determining what portion of the background radiation was due to the beam striking the target and what portion was due to the beam regulation system.

By the use of such an extension beam tube during a preliminary study, protons scattered from the target into the walls of the chamber were found to be a major source of background radiation. Lining the walls of this preliminary chamber with gold foil eliminated this background, and the interior of the final chamber was, therefore, plated with a layer of gold approximately .001" thick. In addition to plating the chamber walls, the target support system and the beam defining baffles were gold plated, and the interior of the entrance beam tube was lined with gold foil. Those portions of the beam system in the immediate vicinity of the control slits and therefore subjected to a considerable amount of scattered beam were also either gold plated or lined with gold foil. Comparison of the gamma-ray spectrum of the scattered beam background with the spectrum obtained from neutron producing reactions such as $O^{18}(p,n)$ or $Cu^{65}(p,n)$ showed that the scattered beam background was almost certainly due to the production of neutrons which were subsequently captured in the NaI(Tl) scintillator. This is clearly possible since two of the most common elements in the beam and chamber system have isotopes which undergo (p,n) reactions for protons of this energy, i.e., $Cu^{65}(p,n)$ and $Fe^{57}(p,n)$. While it certainly would have been possible to have found other heavy elements not undergoing (p,n) reactions at this energy, gold was known to produce a very low background under proton bombardment and was easily obtainable in high purity. The cost of the gold involved was quite negligible in comparison with other experimental expenses; therefore no search was made for a cheaper material. The target chamber itself was constructed of brass not only because of the ease of fabrication but also because of the excellent gold plating properties of brass.

C. Detector and Electronics

A 3"x3" (NaI(Tl) scintillation crystal mounted on a DuMont 6363 3" photomultiplier was used as the gamma-ray detector in this experiment. The crystal and photomultiplier were purchased as a permanently coupled single unit from the Harshaw Chemical Company, Cleveland, Ohio under their designation Integral Line type 12S1213. While a larger crystal would have been desirable from the standpoint of detection efficiency, these crystals had much lower resolution. Reasonably good resolution was desirable to facilitate the analysis of the data by providing adequate separation of the photopeaks of the two capture gamma rays and assuring that the 1.98-MeV gamma ray from the $O^{18}(p,p')$ reaction did not contribute significantly to the region of γ_2's photopeak.* Two resonances in the $O^{18}(p,p')$ reaction were observed for bombarding energies in the region of interest here. The lower resonance was found to have a resonant energy of approximately 2.64 MeV and a width of about 15 keV; the upper resonance was found to have a resonant energy of approximately 2.71 MeV and a width of less than 5 keV. Even though O^{18} constitutes only .198% of natural oxygen, the yield of the 1.98-MeV gamma ray in the region of the lower resonance was so high that if a detector having poor resolution had been used, this gamma ray would have made a significant contribution to the number of counts in the region of γ_2's photopeak. The detector used in this experiment had a photopeak resolution of approximately 5% (full width at half maximum) for the 2.615-MeV gamma ray of ThC". This resolution was sufficiently high to assure that the maximum contribution

---

*Reference to the pulse height spectrum shown in Fig. 4 may be found helpful in following this discussion.

of the 1.98-MeV gamma ray to the γ_2 photopeak yield was less than $\frac{1}{2}\%$; this was neglible in comparison with the 2% statistical uncertainty in the γ_2 yield.

The crystal-photomultiplier assembly contained an internal magnetic shield consisting of one layer of .004" Conetic AA alloy; this was sufficient for the earth's magnetic field. To provide additional magnetic shielding as well as shielding against low energy gamma rays, the assembly was placed in a shield consisting of two concentric steel cylinders with the intermediate space filled with lead. The outer cylinder had an outside diameter of $5\frac{1}{2}$"; the inner cylinder had an outside diameter of $3\frac{1}{2}$", and both cylinders had a wall thickness of $\frac{1}{8}$". Before pouring the lead between the cylinders, a thin walled cylinder was positioned concentrically about the inner cylinder so that a void of approximately $\frac{3}{32}$" remained between the lead and the inner cylinder. Similarly, by making the inner cylinder approximately $\frac{1}{8}$" shorter than the outer cylinder and capping the end of the former with a disk of $\frac{1}{32}$" stock, another $\frac{3}{32}$" void was formed over the end of the crystal. These voids were then filled with boron carbide so that, with the exception of the socket end of the photomultiplier, the detector was completely surrounded by a layer of boron carbide. The purpose of this layer was to absorb thermal neutrons, and thus prevent them from being captured in the NaI(Tl) crystal and producing capture radiation.* Although the gold plating largely eliminated neutron production by the scattered beam, one source of neutrons could not be greatly reduced, namely, the $O^{18}(p,n)$ reaction. This reaction was found

---

*The pulse height spectrum of this capture radiation is shown in Fig. 6.

to undergo a resonance at a bombarding energy of approximately 2.65 MeV; the width of the resonance was approximately 7.5 keV. Since oxygen highly depleted in O^{18} could not be obtained, an attempt was made to absorb the neutrons produced in this reaction before they could be captured by the crystal. Most of the absorption schemes which were investigated actually increased the level of the capture background; presumably this was due to the fact that they were more effective in thermalizing additional neutrons than in absorbing those already thermalized. It was found, however, that a thin layer of boron carbide placed between the detector assembly and the inner wall of a loosely fitting preliminary shield did decrease the capture background. Thus, in designing the final shield, a layer of boron carbide sufficiently thick to absorb thermal neutrons was placed as near to the counter assembly as was mechanically convenient. By the use of this layer of boron carbide, the capture radiation was reduced by approximately a factor of two.

In a preliminary study it was found that the low energy gamma rays produced by a typical beam current of 2-3 μa striking the tungsten target blank caused a 60%-70% dead time in the pulse height analyser. To prevent this jamming of the electronics with useless counts, a $\frac{1}{8}$" thick sheet of lead was fitted over the end of the shield so that all gamma rays entering the detector had to pass through at least this thickness of lead. This amount of lead was sufficient to reduce the dead time to less than 1% while its absorption of the capture radiation was quite small.

The shield was rigidly mounted on a carriage pivoted about the central axis of the target chamber, and this carriage was adjusted so that the central axis of the shield was perpendicular to the axis of the

chamber and intersected it at the beam spot. The inner diameter of the shield was closely matched to the counter diameter, and provisions were made for assuring that the counter face was held tightly against the end of the shield. Thus the detector assembly could be removed from the shield and replaced at a later date in so nearly the same position that the change in the detection efficiency was completely negligible. This allowed one to prevent unnecessary activation of the crystal by removing it from the target room whenever neutron producing reactions were being run on any of the other accelerators. The shield axis was set at 90° to the beam by the use of a long pointer attached to the target rod. This pointer was first adjusted to coincide with the beam direction as defined by the beam spot on the viewing quartz; then using the protractor attached to the lucite plug, the pointer was rotated through 90°, and the carriage was adjusted so that the shield axis coincided with the direction of the pointer. In this manner the shield axis could easily be located to within 1° of the desired angle.

The output of the photomultiplier was fed into a conventional Miller Integrator type preamplifier which was mounted on the rear of the shield assembly. The output of this type of preamplifier is accurately proportional to the total charge deposited on the anode of the photo-multiplier and thus, assuming linearity of the scintillator and photo-multiplier, to the energy deposited by the gamma ray in the crystal. The output of the preamplifier was amplified by a Hamner Model N-302 Chase Higinbotham type non-overloading amplifier and was then fed into a R.I.D.L. Model 34-12 400 channel pulse height analyser. The linearity of the complete system was checked with several natural gamma sources and found to be within 1% in the region of interest.

D. Beam System and Calibration

The experiment was performed using the beam from the magnetic analyser station of the 3 MV electrostatic accelerator of the Kellogg Radiation Laboratory. The magnetic analyser is a double focusing 90° type with a radius of 16"; the magnetic field in the region of the beam tube is measured by a fluxmeter of the null-reading variety. In this case the position of the fluxmeter coil is measured by means of a light beam reflected from a small mirror attached to it, and the standard torque is provided by a phosphor bronze spring. The magnet current was supplied by a semiconductor regulation system using a feedback signal obtained from a resistor in series with the magnet coil. Two sets of pickup slits were used to provide energy stabilization of the accelerator by means of a conventional corona triode feedback system. The use of two sets of slits separated by approximately 12" not only provided improved beam resolution but also allowed machine regulation to be maintained during the time the beam was deflected off the target. To provide horizontal beam stabilization in addition to the vertical stabilization provided by the energy regulation system, a steering magnet regulated by a signal from a set of vertical slits was employed. This magnet also served to deflect the beam off the target when it received a signal from the beam integrator signifying the completion of an integration cycle.

The steering magnet slits and the last set of energy regulation slits were located approximately 12" from the target; this rather large separation was employed to reduce the background due the beam halo striking the slits. The slits were adjusted so that the beam spot on

the quartz had a vertical extension of approximately 2mm and a horizontal extension of 2-3mm. The small vertical extension was required for good energy resolution, and the small horizontal extension was used to assure that the detection efficiency did not vary during a run because of a change in the beam to counter separation.

The energy resolution of the analysing system was determined by measuring the step in the yield of 9-MeV gamma rays from a thick carbon foil due to the resonance in the $C^{13}(p,\gamma)$ reaction at 1.75 MeV. Since the natural width of this resonance is approximately 75 eV, the width of the step observed in the yield of the 9-MeV gamma rays was due almost entirely to the energy spread of the beam. The beam spread measured in this manner was approximately 2 keV (full width at half maximum) for a proton energy of 1.75 MeV. In order to obtain the beam spread for the mean bombarding energy used in the present experiment, the reasonable assumption was made that the ratio $\frac{\Delta E}{E}$ was a constant of the analysing system and, hence, was independent of the proton energy. The beam spread obtained in this manner was 3.0 keV for 2.66 MeV protons. This beam spread is small compared to the thickness of the targets used in the experiment, but it was, nevertheless, included in the final comparison of the experimental results with the theoretical predictions.

During the course of the experiment, the analyser was calibrated against a local standard consisting of the narrow resonance in the $O^{18}(p,p')$ reaction located at a bombarding energy of approximately 2.71 MeV. Using this resonance, the calibration of the fluxmeter was checked several times during each day's run, and in no case was a shift greater than 2 keV observed. At the conclusion of the experiment, the fluxmeter was calibrated

absolutely using the $Li^7(p,n)$ threshold at 1.881 MeV and the $C^{13}(p,\gamma)$ resonance at 1.746 MeV; these two calibrations agreed to within $\pm$ 1 keV. Then using a very thin O^{18} enriched tungsten oxide target and the absolute calibration constant determined for the magnet, the resonant energy of the narrow $O^{18}(p,p')$ resonance was determined to be 2.709 $\pm$ .005 MeV. The width of this resonance was found to be less than 5 keV. The resonant energy of the lower $O^{18}(p,p')$ resonance was also determined and found to be 2.640 $\pm$ .005 MeV; the width of this resonance was measured as 15 $\pm$ 2 keV.

E. Targets

The targets consisted of tungsten blanks approximately 1" x $\frac{1}{2}$" which had been oxidized by heating them in an oxygen atmosphere by means of a radio frequency induction furnace. Oxygen depleted in O^{18} was used in the preparation of the targets in order to reduce the background due to the neutrons produced in the $O^{18}(p,n)$ reaction. A detailed description of the cleaning and oxidation of the tungsten blanks is given in Appendix I. Tungsten oxide was chosen as the target material since a previous study had revealed that commercial grade tungsten produced a very low gamma-ray background when bombarded with protons having energies in the range of interest for this experiment. These preliminary studies had revealed no problems with oxygen loss even though the target was often run red hot. In the first stages of the present experiment, however, considerable difficulty was experienced with a loss of oxygen from the targets unless they were cooled during the bombardments. In the final phase of the experiment, .040" tungsten stock was substituted for the .010" stock originally used, in an effort to produce more uniform

targets, and no further difficulty with oxygen loss was experienced. Because of this experience and further supporting evidence given in Appendix I, it is believed that the loss of oxygen from the targets during the bombardments was due to a local heating phenomenon.

A preliminary estimate of the target thickness was made by measuring the apparent width of the narrow $O^{18}(p,p')$ resonance which was known to have an intrinsic width of less than 5 keV. The final determination of the total oxygen content and the composition of the target was made by studying the elastic scattering of protons from it using the 16" magnetic spectrometer of the 3 MV accelerator. The detailed analysis of this procedure can be found in Appendix I; the results for the target used to obtain the capture data presented here were:

1. The oxide layer was approximately 9 keV thick for protons of the energy used in this experiment.
2. The composition at the front surface of the target was approximately $WO_{2.6}$ with the oxygen content falling off roughly exponentially toward the back of the oxide layer.
3. The number of oxygen atoms seen by a beam striking the target perpendicular to its face was $(8.9 \pm 1.3) \times 10^{17}$ per cm^2.

F. Data Accumulation

Before data accumulation could be started, it was necessary to run the machine for approximately two days with a hydrogen discharge in the ion source in order to reduce the deuteron content of the proton beam to the level of the natural deuterium content of commercial hydrogen.

This "burning out" of the ion source was necessitated by the tendency of the ion bottle to retain a considerable amount of deuterium from previous periods of deuterium operation, and the high initial deuteron contamination of the proton beam resulting from the gradual release of this deuterium caused an extremely large neutron capture background in the crystal. The neutrons were presumably produced by various (d,n) reactions taking place in the vicinity of the mass separation slits of the accelerator, and to reduce the contribution due to the C^{12}(d,n) and C^{13}(d,n) reactions as much as possible, these slits were thoroughly cleaned prior to data accumulation. The observed background due to the residual deuterons in the proton beam was much smaller than that due to the proton beam striking a clean tungsten blank in the target chamber, and thus was completely negligible for the present experiment.

Since there had been considerable difficulty with oxygen loss during the preliminary runs, the final data was taken in several short integrations at each energy, folding back and forth over the anomaly region with each series of integrations. By taking the data in this manner, the separate runs at a given bombarding energy could be checked against each other for signs of oxygen loss, and in case such a loss did occur, that portion of the data up to the time of loss could be salvaged. Using this method of data accumulation, an oxygen loss which was linearly dependent upon the total bombarding charge would tend to affect only the total yield but not the shape of the excitation curve. Any gradual change in the background during the course of a run would also affect all the data points equally in this method of data accumulation. The main disadvantage of this method of taking the data was that very little

drift could be tolerated in the electronics if the separate runs at a given bombarding energy were to be simply added together. In order to obtain the required stability, it was found necessary to "drift" the photomultiplier with the 2.615-MeV gamma ray from a ThC" source for approximately 1-2 hours before data accumulation was begun. To minimize thermal effects in the counter assembly, cooling of the target was also started at this time. With these precautions the drift of the system as determined from the position of the 1.98-MeV gamma ray from the $O^{18}(p,p')$ reaction was found to be less than 1% over the course of a typical 16-18 hour run.

Data was taken at approximately 10 keV intervals over the region of the expected anomaly; each individual integration consisted of 472 μCoul and 8 integrations were taken at each bombarding energy so that the total bombarding charge for each data point was 3.78 mCoul. The time required for each of the bombardments was recorded in order to be able to correct the data for the crystal background and the electronic dead time; the total bombarding time for each data point was approximately 30 minutes. To facilitate the subtraction of the background radiation, 250 channels of the pulse height spectrum were recorded although the capture radiation extended only to channel 110. The data was accumulated in the form of punched tape in order to reduce the print out time and facilitate later analysis.

After the accumulation of the capture data had been completed, the background radiation due to the beam striking a clean tungsten blank was measured. By means of the extension beam tube previously described, it was determined that this background was almost entirely due to the beam

actually striking the blank; only a very small fraction was found to be due to the machine and the beam analysing system. Measurements taken on various blanks of the same stock as that used to produce the oxide targets were all identical to within the experimental error, and in fact tungsten obtained from various commercial sources showed very nearly identical backgrounds. The background was measured at several energies in the anomaly region and found to increase slightly in an approximately linear manner with increasing bombarding energy. In addition to measuring the background radiation due to the tungsten blank, a thin O^{18} enriched tungsten oxide target was used to determine the spectrum of the neutron capture radiation produced by the neutrons from the $O^{18}(p,n)$ reaction. Using this very thin oxide target and the absolute calibration of the magnet, the width and energy of the resonance occurring in this reaction was also determined; the intrinsic width of the resonance was found to be approximately 7.5 keV and the resonant energy was $2.649 \pm .005$ MeV.

III. DATA ANALYSIS

A. Data Compilation and Background Subtraction

Before the analysis of the data was undertaken, the individual runs at a given bombarding energy were added in various groups of 3 and 4 and compared to each other in order to check for possible loss of oxygen from the target. Since no indications of such a loss were discovered, the individual runs at a given bombarding energy were added together, and this sum spectrum was used for all further analysis. Figure 4 shows a typical pulse height spectrum obtained by this procedure; the bombarding energy of 2.632 MeV was near the lower $O^{18}(p,p')$ resonance, and the 1.98-MeV gamma ray from this reaction is quite prominent. The .871-MeV gamma ray from the $O^{17}(p,p')$ reaction is also quite prominent even though the oxygen used to prepare the target contained only .045% O^{17}.

To extract the $O^{18}(p,n)$ and tungsten blank backgrounds from these spectra, the region above the photopeak of γ_1 was fit with the known background spectrum, and the resulting curve was then used to extrapolate the background into the region of the photopeaks of the two capture gamma rays. Since all the tungsten background spectra had the same shape to within the statistical uncertainity, they were added together to form the standard tungsten background spectrum shown in Fig. 5; the $O^{18}(p,n)$ background spectrum is shown in Fig. 6. In these two spectra the single channel counts have been added into 5-channel sums placed at the center of the 5-channel region over which the sum was taken; this summation reduces the statistical fluctuation of the counts and facilitates the representation of the spectra by the smooth curves shown in the figures. The tungsten and $O^{18}(p,n)$ spectra differ by 10-15% in the region of the capture photo-

peaks if normalized to contain the same number of high energy counts; some method of determining the relative contribution of the two types of background was, therefore, required. Since the measured width of the $O^{18}(p,n)$ resonance was only 7.5 keV and the yield off resonance was quite small, the background was assumed to be due entirely to the tungsten blank except in the region of the $O^{18}(p,n)$ resonance. In the region of this resonance the tungsten background was assumed to vary linearly between the two values used at the edges of the resonance region, and the remaining background was assumed to be due to the $O^{18}(p,n)$ reaction.

The procedure used to subtract the background from each of the capture spectra was thus to first determine that factor α which when multiplied by the tungsten background of Fig. 5 gave the best least squares fit to the capture spectrum in the region of channels 115 to 220. The various α's were then plotted as a function of the bombarding energy used to obtain the corresponding capture spectrum, and the proper linear extrapolation of α through the region of the $O^{18}(p,n)$ resonance was determined. Using the value of α determined by this linear extrapolation, the subtraction procedure was repeated for the region of the $O^{18}(p,n)$ resonance, and the remaining background was fit with the $O^{18}(p,n)$ spectrum of Fig. 6 multiplied by a second factor β. The background subtraction was performed on an electronic computer; this was programmed so that once the best choice of the two factors α and β had been determined, the corresponding background was automatically subtracted from the capture spectrum, and the resulting spectrum together with the standard deviations in the α and β least squares fits were automatically printed out. The result of

this subtraction procedure is shown in Fig. 7 for the raw spectrum previously shown in Fig. 4; more of the high energy tail has been shown in Fig. 7 in order to illustrate the subtraction.

The tungsten blank subtraction from the region of γ_2's photopeak amounted to approximately 15% of the average γ_2 photopeak yield;* the maximum $O^{18}(p,n)$ background subtraction amounted to 37% of the γ_2 photopeak yield at that bombarding energy. For γ_1 the tungsten blank subtraction amounted to approximately 70% of the average photopeak yield; while the maximum $O^{18}(p,n)$ subtraction amounted to 150% of the corresponding γ_1 photopeak yield.

B. Determination of the Raw Photopeak Yield

The photopeak yield for the two capture gamma rays was determined by simply adding the counts contained in a given interval centered about the peak of the photopeak distribution; the location of this peak was determined graphically.** The resolution of the detector was assumed to be constant, and the width of the interval over which the photopeak sum was taken was, therefore, varied linearly with the energy of the gamma ray. The resolution of the detector is, in fact, dependent upon the energy of the gamma ray, but estimates of the magnitude of this effect for the energy range considered here showed that the error made by neglecting it

---

*The photopeak yields mentioned here refer to the number of counts contained within the photopeak of the gamma ray in question after the various background subtractions had been made. The raw photopeak yields to be discussed in the next section were used in arriving at the percentage contributions given above.

**These intervals and the graphical method used to determine the center of the γ_2 photopeak distribution are shown in Fig. 7.

was a great deal smaller than the statistical uncertainty in the photopeak yield.

To determine the center of γ_2's photopeak distribution, each of the spectra was plotted, and the sides of the photopeak distribution were fit visually with straight lines. The point of intersection of these two lines was then taken to be the center of the region over which the photopeak counts were summed. Because of the very poor statistics in γ_1's photopeak counts, two methods were used to determine the center of the γ_1 photopeak. In one method the center was determined graphically as for γ_2; in the other method the center was determined from the center of the γ_2 photopeak and the known energy difference between the two gamma rays. The photopeak counts obtained by these two methods always agreed to well within the statistical uncertainty. The graphical determination of the center of the γ_2 photopeak distribution was checked by shifting the centers so as to lie along a straight line at a position given by the known bombarding energies; the required shift was always less than one channel, and the resultant change in the photopeak yield was less than $\frac{1}{2}\%$.

The interval over which the γ_1 photopeak counts were summed was taken to be 11 channels wide for a gamma-ray energy of $E\gamma_1^{o*} = 3.094$ MeV, and the interval over which the γ_2 photopeak counts were summed was taken to be 10 channels wide for a gamma-ray energy of $E\gamma_2^{o*} = 2.594$ MeV. These gamma-ray energies correspond to a bombarding energy of 2.66 MeV with a target 9 keV thick for protons of this energy. The width of these

---

*A superscript ^{o} will be used to denote the value of the quantity in question for the mean bombarding energy of 2.66 MeV and a target thickness of 9 keV.

intervals was varied linearly with the gamma-ray energy, and in the case of fractional channel limits, linear interpolation was used between the nearest two channels.

The result of this determination of the photopeak yields for the two capture gamma rays is given in Table I; the error quoted here is just that due to counting statistics plus the probable error in the individual background subtractions. The results shown in Table I will be referred to as the raw photopeak yield since the photopeak counts have been corrected for only the tungsten blank, $O^{18}(p,n)$, and crystal backgrounds.

C. Correction of the Raw Photopeak Yield

In order to obtain the counts actually due to the photopeak of γ_1, it was necessary to correct the raw γ_1 photopeak yield for those counts resulting from the detection of both γ_2 and the subsequent gamma-ray transition to the ground state of F^{17}, γ_3. If both γ_2 and γ_3 deposited nearly their full energy in the scintillator, then the resultant pulse would clearly lie within the area occupied by γ_1's photopeak. Similarly, in order to obtain the number of counts actually due to the γ_2 photopeak, the raw γ_2 photopeak yield had to be corrected for those counts belonging to the Compton distribution and the first escape peak of γ_1. Since the corrections to the γ_1 and γ_2 photopeak yields were interdependent, it was necessary to use an iterative procedure to apply them. The determination of these corrections was rather involved and required a considerable amount of additional experimental work. The description of this process has, therefore, been placed in Appendix II; the final results will simply be stated here. The correction to the raw γ_2 photopeak

yield due to Compton distribution and the first escape peak of γ_1 amounted to 818 $\pm$ 35 counts for a γ_1 energy of 3.094 MeV; this was approximately 18% of the average raw γ_2 photopeak yield. The summing correction to the raw γ_1 photopeak yield was given by .038 $\pm$ .005 of the corrected γ_2 photopeak yield; for the average corrected γ_2 results this amounted to approximately 135 counts or about 14% of the raw γ_1 photopeak yield.

Before the γ_1 and γ_2 photopeak yields could be compared with the theoretical predictions, a correction had to be made for the variation of the detector efficiency with the energy of the gamma ray. The energy range covered in the present experiment was only about 200 keV; therefore, except at the extreme ends of the range, these corrections were quite small. The change in the absorption of the various materials between the target and the scintillation crystal could be neglected over this small energy range; thus the change in detection efficiency was due almost entirely to the crystal itself. To determine the variation in the photopeak detection efficiency for the crystal used in the present experiment, the data of Heath (1957) for a free 3"x3" NaI(Tl) was used; in order to obtain the photopeak efficiency, it was necessary to combine the curves giving the peak to total ratio with those giving the total detection efficiency. Making a linear approximation to the energy dependence of these two factors, the energy dependence of the photopeak efficiency was found to be given by:

$$\epsilon_{ph.pk.}(E\gamma) = \epsilon_{ph.pk.}(E\gamma^{o}) \left(1 - .038 \pm .005 \frac{(E\gamma - E\gamma^{o})}{100 \text{ keV}}\right)$$

Where $E\gamma$ is the energy of the gamma ray, and $E\gamma^{o}$ is the reference energy. This expression holds for both γ_1 and γ_2 to within the quoted error; thus the total change in the photopeak efficiency over the energy range covered by the present experiment was approximately 7.5%.

Finally, it was, in principle, necessary to correct the photopeak yields for the dead time of the electronics. Actually, this correction was completely negligible since the maximum dead time, as computed from the known dead time per channel of the pulse height analyser and the number of counts in each channel, was found to be only .85%.

Table II gives the photopeak yields for the two capture gamma rays after the corrections discussed above had been applied; here again the error attached to each of the data points is just that due to counting statistics plus the estimated error in the background subtraction. The other significant sources of error would affect all the data points in the same manner and hence would simply add or subtract the same number of counts from each point. This common error has not been included in the error attached to the individual data points since this would indicate an additional uncertainty in the shape of the excitation curves which was not actually present. This common error is listed separately at the bottom of the table. There are other sources of error which do affect the data points individually, but these are all much too small to be significant in comparison with the individual errors due to counting statistics and the background subtraction.

Figures 8 and 9 show the corrected photopeak yields of Table II plotted as a function of the bombarding energy; the common error has been indicated here by the single error bar below the excitation curves. It is clear from Fig. 8 that an anomaly is present in the yield of γ_2; the anomaly is mainly of the interference type and has a peak to valley ratio of approximately 1.75. Figure 9 shows that, within the experimental

uncertainty of approximately 10%, no anomaly is present in the yield of γ_1. The solid curves shown in these figures are the calculated excitation curves which will be discussed in Section IV.

D. Detection Efficiency

In order to obtain a cross section from the experimental photopeak yield, it was necessary to determine the absolute detection efficiency for the photopeaks of the two capture gamma rays. These efficiencies were obtained by determining the photopeak detection efficiency for the 2.615-MeV gamma ray of ThC", and then using the free crystal data of Heath (1957) to obtain the photopeak efficiencies for the capture gamma rays relative to the 2.615-MeV gamma rays.

The photopeak detection efficiency for the 2.615-MeV gamma ray was determined by measuring the counting rate for a small ThC" source placed on the target blank at the location of the beam spot. The ThC" source was, in turn, calibrated by determining the counting rate when it was placed in a well defined free crystal situation for which the photopeak detection efficiency could be obtained from the data of Heath. The free crystal calibration of the ThC" source was carried out by placing it on a very thin Lucite support so that it was located at a precisely determined distance from the front face of the free crystal assembly. The source was also carefully positioned so as to lie on the axis of the crystal assembly. Thus the source was placed in a well determined "standard geometry," and the photopeak detection efficiency could be taken to be that given by the data of Heath. It was necessary to correct the spectra taken with the source in the target chamber for the effects of summing in the manner described in Appendix II. The free crystal data,

however, was taken with the source 10 cm from the crystal face, and the summing was, therefore, negligible. The result of this determination of the photopeak detection efficiency for the 2.615-MeV gamma ray was:

$$\epsilon_{ph.pk.}\ (2.615\ \text{MeV}) = .0111 \pm .0009^{*}$$

The error quoted above includes an additional term to represent the effect of the possible deviation of the location of the ThC" source during the calibration from the location of the beam spot during the data accumulation.

The photopeak detection efficiency for a gamma ray of energy $E\gamma_1^{o}$ = 3.094 MeV relative to that for a 2.615-MeV gamma ray, as taken from the free crystal data of Heath, is .83 $\pm$ .08; the error quoted here is simply a conservative estimate of the maximum possible deviation from the free crystal ratio. The $E\gamma_2^{o}$ energy of 2.594 MeV is so near the energy of the ThC" gamma ray that the free crystal photopeak efficiencies differ by less than 1%. The linear approximation to the photopeak efficiency previously described gives the relative efficiency as 1.008.

The photopeak efficiencies obtained by combining these relative efficiencies with the ThC" calibration refer to the number of counts contained within a Gaussian approximation to the photopeak distribution. In the analysis of the capture data, however, the photopeak yield was determined by simply summing all the counts contained within a given interval, ΔE, centered about the photopeak. Thus, to obtain the photopeak efficiencies appropriate to the capture results, it was necessary

---

*The efficiencies quoted here include the factor arising from the solid angle subtended by the detector.

to determine the ratio of the photopeak counts obtained by the two methods. The ratio of the counts obtained by the Gaussian approximation to the photopeak to the counts obtained by the sum over the interval ΔE was found to be $.97 \pm .05$ for γ_1 and $.94 \pm .04$ for γ_2.

In principle, it was necessary to correct the γ_2 photopeak efficiency for the effect of γ_2—γ_3 summing into and out of the photopeak region. It is shown in Appendix II, however, that the effect of this summing on the γ_2 photopeak efficiency is very slight; the photopeak efficiency without summing is simply multiplied by a factor of .99.

Combining these factors, one obtains for the γ_1 and γ_2 photopeak detection efficiencies:

$$\epsilon_{ph.pk.}(E\gamma_1^{\circ}) = .0095 \pm .0013 \qquad E\gamma_1^{\circ} = 3.094 \text{ MeV}$$

$$\epsilon_{ph.pk.}(E\gamma_2^{\circ}) = .0118 \pm .0011 \qquad E\gamma_2^{\circ} = 2.594 \text{ MeV}$$

The efficiencies quoted above refer to an isotropic gamma-ray distribution; the predicted angular distribution, however, for both γ_1 and γ_2 is non isotropic. It is shown in Appendix IV that the predicted angular distribution for γ_1 has the form $(1 + A \sin^2\theta)$* with the value of A being approximately .2. The predicted angular distribution for γ_2 changes in passing through the resonance region; off resonance the angular distribution has the simple $\sin^2\theta$ form characteristic of a P to S dipole transition with no spin flip. In the resonance region, however, the spin flip

---

*θ here is the polar angle with respect to the beam. That is if the z axis of a cartesian coordinate system is taken to lie along the beam direction such that the beam moves in the positive z direction, then θ is the standard polar angle of a spherical polar coordinate system.

amplitude contributed by the resonant state formation introduces an additional isotropic term. Thus, to be able to compare the experimental results with the theoretical calculations, it was necessary to determine the photopeak detection efficiency for a $\sin^2\theta$ angular distribution relative to that for an isotropic distribution.

The effect of the efficiency ratio $S(\theta)^*$ was reasonably important in predicting the shape of the γ_2 anomaly; therefore it was necessary to determine the value of this ratio fairly accurately for γ_2. For γ_1, on the other hand, a 10% change in the value of $S(\theta)$ would result in a change of only 2% in the predicted yield and no change in the shape of the predicted excitation function; hence the value of $S(\theta)$ for γ_1 was simply taken to be equal to the value of $S(\theta)$ determined for γ_2.

The description of the method used to determine $S(\theta)$ is rather lengthy; therefore it has been placed in Appendix III. $S(\theta)$ was found to be equal to $.87 \pm .01$ for the 2.615-MeV gamma ray of ThC". Since the capture data was taken with the detector centered about $\theta = 90°$, $\sin^2\theta$ was approximately equal to 1 over most of the detector, and it was consequently found that the value of $S(\theta)$ was not strongly dependent upon the exact form of the detector's angular sensitivity. $S(\theta)$ would, therefore, not be expected to be strongly dependent upon the energy of the gamma ray, and $S(\theta)$ for γ_2 should be very close to the value determined for the 2.615-MeV gamma ray of ThC". Since the exact value of

---

*$S(\theta)$ will be used as a shorthand notation for the ratio of the photopeak detection efficiency for a gamma ray having a $\sin^2\theta$ angular distribution to that for a gamma ray having an isotropic distribution.

$S(\theta)$ for γ_1 was not very important, the approximation made by using the value determined for the ThC" gamma ray should be quite good.

Thus in the comparison between the experimental results and the theoretical calculations the ratio was taken to be:

$$S(\theta) = .87 \pm .01 \qquad \text{for both } \gamma_1 \text{ and } \gamma_2$$

IV. COMPARISON WITH THEORY

A. Discussion of the Model

Calculation of the cross section for capture to the $\frac{1}{2}^+$ .500-Mev state and the $\frac{5}{2}^+$ ground state of F^{17} consists basically in evaluating the two perturbation matrix elements $\left\langle \Psi_f^{\frac{1}{2}^+} | H_{int} | \Psi_{in} \right\rangle$ and $\left\langle \Psi_f^{\frac{5}{2}^+} | H_{int} | \Psi_{in} \right\rangle$. Here H_{int} is the interaction Hamiltonian due to the electromagnetic field, and Ψ_{in} and Ψ_f are respectively the initial and final wave functions of the system. In practice, of course, these wave functions are not known so that rather drastic approximations must be made in order to evaluate the matrix elements. In the extranuclear model employed here, only those portions of the wave functions corresponding to configurations in which the proton is outside the nuclear potential of the O^{16} core are included in the calculation of the matrix elements. For these configurations where there is no nuclear interaction between the proton and the O^{16} nucleus, the initial and final wave functions are simply those of a proton in the Coulomb field of the O^{16} nucleus. Thus, in the present calculation the matrix elements were obtained by using the appropriate free and bound Coulomb functions and simply cutting off the integrals at a separation distance corresponding to the F^{17} "nuclear radius."

Actually, the calculation was not completely extranuclear since the internal* transition taking place through the resonant $\frac{1}{2}^-$ state of the compound nucleus was also included. The nonresonant contributions

---

*Throughout this discussion "internal" will refer to those configurations in which the proton is within the O^{16} nucleus; "external" will refer to the configurations for which the proton is outside this nucleus.

to the capture matrix elements arising from configurations in which the proton was within the nuclear field of the O^{16} nucleus could also have been included by the use of a suitable single particle wave function; this was not done, however, for two reasons. First, because of the small penetration of the proton into the internal region, these internal contributions would have been quite small. Calculations using a square well potential, for example, showed that the internal contribution to the capture matrix element was only about 2-3% of the external contribution; this was smaller than the variation in the external contribution produced by the uncertainty in the $O^{16}(p,p)$ elastic scattering phase shifts. Second, since the $\frac{1}{2}^-$ resonant state was treated by means of single level R matrix theory, it was not obvious how a nonresonant internal contribution could be included in a consistent manner for the $P_{\frac{1}{2}}$ partial wave. In order to treat all partial waves consistently, the nonresonant internal contributions were, therefore, simply neglected.

In calculating the capture matrix elements, it was convenient to expand the initial wave function in terms of partial waves and the interaction Hamiltonian in terms of multipole operators; only the largest terms in the resulting series of partial matrix elements were then retained in the final calculation. While the major contribution to the γ_1 and γ_2 capture matrix elements was clearly due to E1 capture from the $\ell = 1$ partial wave, it was not clear in this case that all the other contributions were completely negligible. Because of the extranuclear character of the interactions, the usual penetration arguments were not directly applicable; hence it was not apparent that the higher partial waves would not

contribute significantly to the total matrix element. It was, therefore, considered useful to determine, by means of a crude estimate, which terms should be included in the final calculation of the capture matrix elements.

In order to make such an estimate of the relative contribution of the various multipoles and partial waves, the exact expressions for the matrix elements involved were approximated by neglecting the angular momentum coupling factors and replacing the complete matrix element by an appropriate radial integral. These radial integrals were then multiplied by the appropriate energy dependent factors to yield an estimate for the capture amplitude via the multipole and partial wave in question. The amplitudes so obtained were compared with the amplitude for E1 capture from the $\ell = 1$ partial wave. Those terms which yielded an amplitude greater than 1% of this main amplitude are indicated below.

For γ_1 Capture to the $\frac{5}{2}^+$ Ground State of F^{17}

$S_{\frac{1}{2}}$	$P_{\frac{1}{2}}$	$P_{\frac{3}{2}}$	$D_{\frac{3}{2}}$	$D_{\frac{5}{2}}$	$F_{\frac{5}{2}}$	$F_{\frac{7}{2}}$	$G_{\frac{7}{2}}$	$G_{\frac{9}{2}}$
E2		E1	M1	M1	E1	E1	M1	
			E2	E2			E2	E2

For γ_2 Capture to the $\frac{1}{2}^+$ .500 Mev State of F^{17}

$S_{\frac{1}{2}}$	$P_{\frac{1}{2}}$	$P_{\frac{3}{2}}$	$D_{\frac{3}{2}}$	$D_{\frac{5}{2}}$	$F_{\frac{5}{2}}$	$F_{\frac{7}{2}}$	$G_{\frac{7}{2}}$	$G_{\frac{9}{2}}$
M1	E1	E1	M1					
			E2	E2				

The underlined terms are those which had amplitudes significantly larger than the other terms; these were the terms which definitely had to

be included in the exact calculation of the capture matrix elements. The E1 terms proceeding from the $\ell = 1$ partial wave were, of course, in this category; however in the case of γ_1 there were additional E1 terms proceeding from the $\ell = 3$ partial wave which also had to be included. The remaining terms had amplitudes of 2-5% of the E1 P wave amplitude. Thus the only significant contribution of one of these terms to the absolute square of the capture matrix would have arisen from the cross product between it and the main E1 amplitude. The maximum contribution of such a cross product term would have been approximately 10% of the main term. Since each of these additional contributions proceeded from a partial wave having even ℓ while the main E1 contribution arose from odd ℓ, the cross product term would have had an angular distribution which was odd about $\theta = 90°$. The experimental data, however, was taken with the counter centered about $\theta = 90°$; thus if the detection efficiency had been perfectly symmetric about the axis of the counter, terms which were odd about $\theta = 90°$ would not have contributed to the experimental yield. There was a small asymmetry in the detection efficiency about $\theta = 90°$ due to the asymmetric absorption of the target blank and the target holder; this asymmetry, however, was certainly less than 10-15%. The total contribution of the various cross product terms to the observed yield would thus have been of the order of 4-5% of the main contribution. Since the resonant portion of the γ_2 $P_{\frac{1}{2}}$ amplitude was itself quite small, the only appreciable cross product terms would have had a nonresonant energy dependence; thus the inclusion of these additional terms would simply have changed the predicted nonresonant yield by approximately 4-5%. Since this was of the same order as the variation in the nonresonant yield produced by the uncertainity in the $O^{16}(p,p)$ elastic scattering phase shifts, these additional terms were neglected.

In order to be able to calculate the extranuclear matrix elements, it was necessary to know the $O^{16}(p,p)$ elastic scattering phase shifts for the various partial waves involved. Since it had been decided that only the P and F partial waves were to be included in the calculation, it was necessary to obtain only the $P_{\frac{1}{2}}$, $P_{\frac{3}{2}}$, $F_{\frac{5}{2}}$, and $F_{\frac{7}{2}}$ phase shifts. In principle, these phase shifts could have been obtained from an analysis of the $O^{16}(p,p)$ elastic scattering in this energy region; however the recent paper of Salisbury and Richards (1962), in which such an analysis is carried out, clearly demonstrates that most of these quantities are too small to be extracted with any degree of accuracy from the available scattering data. In particular, the $F_{\frac{5}{2}}$ and $F_{\frac{7}{2}}$ phase shifts were much too small to be determined by Salisbury's analysis; therefore they were assumed to be given by the $\ell = 3$ hard sphere phase shift for the F^{17} radius used in the matrix element computation. The analysis of Salisbury indicates that the non-resonant portion of the $P_{\frac{1}{2}}$ phase shift is approximately equal to the $P_{\frac{3}{2}}$ phase shift and is of the order of - .05 radians in this energy range. Thus, in calculating the capture matrix elements, the $P_{\frac{1}{2}}$ potential phase shift was taken to be equal to the $P_{\frac{3}{2}}$ phase shift, and this common phase shift was denoted by $-\varphi_1$. The $P_{\frac{1}{2}}$ phase shift of Salisbury's analysis had a rather strange resonant behavior; this was undoubtedly due to the effect of the experimental error on the least squares search used to obtain the phase shifts. Therefore, in the capture calculations the $P_{\frac{1}{2}}$ resonant phase shift was taken to be that given by single level R matrix theory; the width of this level was taken to be 20 keV as quoted by Salisbury.

The internal γ_2 transition taking place through the resonant formation of the $\frac{1}{2}^-$ F^{17} state was included in the capture calculation by simply assigning a parameter to represent the transition strength for the case in which the wave function of the compound nuclear state was normalized to unit amplitude. This normalized transition strength was then multiplied by the amplitude of the compound nuclear state as given by single level R matrix theory. This is exactly analogous to the method used to include a partial width for a gamma-ray transition in ordinary R matrix theory; here, however, because transitions can occur externally as well as through the state of the compound nucleus, the phase between the two matrix elements is important. This phase is given by single level R matrix theory; see for example the review article of Lane and Thomas page 296 (1958).

B. Comparison With γ_2 Results

Using the phase shifts and the method for treating the internal transition discussed above, the derivation of the differential capture cross section for γ_1 and γ_2 is quite straightforward but somewhat lengthy; it has, therefore, been placed in Appendix IV. In this derivation the additional approximations $\sin \varphi_1 \approx \varphi_1$, $\cos \varphi_1 \approx 1$, and $\frac{\Gamma_p}{\Gamma} \approx 1$ have been made. The first two are well justified since φ_1 is of the order of .05 to .10 radians from Salisbury's analysis, and the approximation $\frac{\Gamma_p}{\Gamma} \approx 1$ is certainly valid since only the elastic scattering and capture channels are open at this bombarding energy.

For γ_2 one obtains:

$$\frac{d\sigma}{d\Omega} = K \frac{E_\gamma^3}{E_p^{\frac{3}{2}}} \left[\sin^2\theta \left[\begin{array}{l} M_1^2 - 2M_1M_2\phi_1 - \frac{2}{3}\sin^2\delta R \left\{ M_1^2 - 2\phi_1 M_1 M_2 \right\} \\ + \frac{2}{3}\sin\delta R\cos\delta R \left\{ M_1M_2 + \phi_1(M_1^2 - M_2^2) + T(M_1 - \phi_1 M_2) \right\} \\ + \frac{2}{9}\sin^2\delta R \left\{ M_2^2 + M_1^2 + 2T(M_2 + \phi_1 M_1) + T^2 \right\} \end{array} \right] \right] \quad (1)$$

Where

$$K = \frac{1}{\sqrt{2}} \frac{e^2}{\hbar c} \frac{1}{(m_p c^2)^{\frac{1}{2}}} \frac{1}{\hbar c} \left\{ 1 - \frac{8\, m_p}{m_{O16}} \right\}^2 \quad \text{For } E_p \text{ in the Lab System.}$$

M_1 and M_2 are the two capture matrix elements given by

$$M_1 = \int_{r_o}^{\infty} g_b^{\frac{1}{2}^+}(r)\, F_1(kr) r^2 dr \qquad M_2 = \int_{r_o}^{\infty} g_b^{\frac{1}{2}^+}(r)\, G_1(kr) r^2 dr$$

Where $g_b^{\frac{1}{2}^+}(r)$ is the bound Coulomb function for $\ell = 0$ and a binding energy of 98 keV corresponding to the .500-MeV $\frac{1}{2}^+$ state of F^{17}; $F_1(kr)$ and $G_1(kr)$ are the free Coulomb functions for $\ell = 1$, and r_o is the cutoff radius for the integrals corresponding to the "nuclear radius" of F^{17}.

δR is the resonant phase shift given by: $\delta R = \tan^{-1}\left\{ \frac{\frac{\Gamma}{2}}{E_R - E_p} \right\}$

φ_1 is the negative of the common $P_{\frac{1}{2}}$, $P_{\frac{3}{2}}$ potential phase shift.

T is the strength parameter for the internal γ_2 transition taking place through the resonant $\frac{1}{2}^-$ state of the compound nucleus. The definition of T in terms of the internal wave functions is given in Appendix IV; in

terms of the usual partial width Γ_γ, T is given by:

$$T = 2.23 \times 10^4 \left(\frac{E_p^{\frac{1}{2}}}{E_\gamma^3} \frac{\Gamma_\gamma}{\Gamma} \right)^{\frac{1}{2}} (\text{fermi})^{\frac{1}{2}}$$

Since the two capture integrals M_1 and M_2 involved only known functions, it was possible to compute them to any desired accuracy once the proper normalization of the bound state wave function had been determined. This normalization could have been obtained from the empirical single particle reduced width for the $\frac{1}{2}^+$ state if this had been known. Unfortunately this reduced width was not known; hence it was necessary to consider the normalization of the bound state wave function as a free parameter to be determined either empirically from the capture data or on the basis of a model wave function for the internal portion of the $\frac{1}{2}^+$ state. Except for the occurrence of the internal transition parameter, T, the predicted shape of the excitation curve would have been independent of the value of this normalization factor since it was common to both M_1 and M_2. The factor T, however, was completely unknown and could only be determined empirically or on the basis of model wave functions for the $\frac{1}{2}^-$ and $\frac{1}{2}^+$ states of the compound nucleus. Thus, it was useful to divide all the terms contained within the large bracket in Eq. 1 by M_1^2 and replace the free parameter T by another free parameter $\xi = \frac{T}{M_1}$. When the expression for the differential cross section was rewritten in this manner, the dependence of the predicted shape of the excitation curve upon the two parameters $R = \frac{M_2}{M_1}$ and ξ was explicitly exhibited.

In order to obtain an expression with which the experimental results could be compared, it was necessary to integrate the differential

cross section given by Eq. 1, rewritten in the manner described above, over the solid angle subtended by the detector. Since the photopeak detection efficiency for a $\sin^2\theta$ angular distribution had been determined to be .87 relative to the photopeak detection efficiency for an isotropic distribution, this integration could be performed by simply replacing $\sin^2\theta$ in Eq. 1 by .87 and multiplying the expression by the solid angle subtended by the counter. Denoting this integrated expression by σ_{xtal} and the solid angle of the detector by Ω_{xtal}, the result of this process was:

$$\sigma_{xtal} = .87\, K\Omega_{xtal} M_1^2 \frac{E_\gamma^3}{E_p^{\frac{3}{2}}} \left[\begin{array}{l} 1 - 2R\phi_1 \\ + \frac{2}{3} \sin\delta R \cos\delta R \left(R+\phi_1(1-R^2) + \xi(1-R\phi_1) \right) \\ - \sin^2\delta R \left[\begin{array}{l} .411 - .255R^2 - 1.33R\phi_1 \\ -.511\xi(R+\phi_1) - .255\xi^2 \end{array} \right] \end{array} \right] \qquad (2)$$

Where $R = \frac{M_1}{M_2}$ and $\xi = \frac{T}{M_1}$

The capture matrix elements M_1 and M_2 were evaluated for bombarding energies between $E_p = 2.56$ MeV and $E_p = 2.76$ MeV in 20 keV intervals and for cutoff radii r_o between 4.0 and 6.0 fermi. The method used to calculate the capture matrix elements is described in Appendix IV; the matrix elements obtained in the manner described there are estimated to be accurate to within $\pm$ 2%. The energy dependence of M_1 and M_2 was found to be approximately linear and independent of r_o over the range of bombarding energies and r_o values considered here. M_1 was found to be very nearly

constant over the energy range of interest, but M_2 decreased by approximately 9% for a 100 keV increase in bombarding energy. The penetration factor $P_1 = \frac{kr_o}{F_1^2(kr_o) + G_1^2(kr_o)}$ was also found to have a linear energy dependence which was independent of the particular value of r_o for which it was evaluated. The energy dependence of P_1 amounted to a 7% increase in P_1 for a 100 keV increase in the bombarding energy. The width of the $\frac{1}{2}^-$ resonance, Γ, was corrected for the variation in P_1 in accordance with the single level formula $\Gamma = 2P_1\gamma^2$—Lane and Thomas, page 323 (1958). The level shift was also estimated, but since it amounted to less than a 1% change in the resonant denominator, it was neglected. Thus in the definition of the resonant phase shift, δR, given on page 38, the resonant energy, E_R, was taken to be a constant.

The energy dependence of the common phase shift φ_1 could not be determined from the analysis of Salisbury because of the fairly large scatter in the extracted phase shifts. The results of this analysis could, however, be used to place an upper limit on the magnitude of such an energy dependence. Using this upper limit for the energy dependence of φ_1, it was found that its effect on the predicted excitation function would amount to only 1-2% over the entire energy region of interest. Thus the estimated maximum effect of the energy dependence of φ_1 was only of the same order as the statistical uncertainity in the γ_2 data and was, in fact, of the same order as the effect of the probable error in the correction made to the raw photopeak yield for the energy dependence of the detection efficiency. The energy dependence of φ_1 was, therefore, simply neglected, and φ_1 was taken to be a constant over the energy range considered here.

Once the energy dependence of the parameters appearing in Eq. 2 had been determined, it was only necessary to specify the value of R, φ_1, and ξ at the mean bombarding energy E_p^{o*} in order to predict the shape of the excitation curve uniquely. Before this excitation curve could be compared with the experimental results, it was necessary to correct the calculated curve for the effects of the finite target thickness and beam resolution. This correction was carried out by folding the excitation curve given by Eq. 2 with the target composition—beam resolution curve shown in Fig. 14. After this folding had been carried out, the shape of the predicted excitation curve could be compared directly with the experimental data; however the absolute yield could not be predicted since the proper normalization of the bound state wave function was not known. Thus, in comparing the predicted and experimental excitation curves, the value of M_1^{*2} was considered to be a free parameter and was varied to obtain the best agreement with the experimental data. This empirical M_1^{*2} could then be used to obtain the empirical single particle reduced width for the .500-MeV $\frac{1}{2}^+$ state of F^{17}.

The resonant energy, E_R, was also considered to be a free parameter and was chosen so as to give the best agreement between the experimental data and the calculated excitation curve. The resonant energy quoted in the paper of Salisbury is 2.66 MeV in the laboratory system; however the energy scales used in the scattering experiment and the present experiment could differ by 5 keV and still be within the probable errors of the two

---

*Here again the superscript ^{o} will be used to denote the value of the quantity in question for the mean bombarding energy of 2.66 MeV with a target 9 keV thick for protons of this energy.

calibrations. Since the least squares fit between the observed and predicted interference anomaly was quite sensitive to the exact value of the resonant energy used in the calculation, it was necessary to vary this energy until the best fit was obtained. The resonant energy determined in this manner was always within 3-4 keV of the value quoted by Salisbury.

Of the three shape determining parameters R^o, φ_1, and ξ^o only the internal transition parameter, ξ^o, could be considered as completely free. The ratio R^o was uniquely determined once the cutoff radius r_o was chosen. There was, of course, considerable latitude in the choice of r_o; thus, instead of being uniquely determined, R^o was only restricted to a range of values corresponding to the range chosen for r_o. Using the formula $r_o = 1.45\ (16^{\frac{1}{3}} + 1)$, one obtains $r_o = 5.1$ f and a corresponding R^o value of .71; taking 4.6—5.6 f as a reasonable range of r_o, R^o was then limited to lie within the range $.55 \leq R^o \leq .85$. The value of φ_1 was not determined accurately by the analysis of Salisbury; however the analysis indicated that φ_1 was probably in the range .05—.10 rad. Since the hard sphere shift at this energy for radii in the range given above is approximately .20 rad, it seemed reasonable to limit φ_1 to lie in the range $0 \leq \varphi_1 \leq .15$ rad.

The value of the internal transition parameter ξ^o is completely unspecified until some sort of wave functions are assumed for the $\frac{1}{2}^-$ and $\frac{1}{2}^+$ levels of F^{17} so that the transition strength can be calculated. The $\frac{1}{2}^+$ state is presumably well described by a $2S_{\frac{1}{2}}$ single particle wave function; the $\frac{1}{2}^-$ state, however, is almost certainly not a single particle state. The excitation energy of 3.10 MeV for this state is much too low to allow

the state to be interpreted as a $2P_{\frac{1}{2}}$ single particle state, and the small single particle reduced width for the state as deduced from the elastic scattering data (Salisbury and Richards, page 2154, 1962) also suggests that a single particle description is not valid. This state, therefore, almost certainly involves configuration mixing of particles from the 1P levels of the O^{16} core into the 1D and 2S levels. It is clear that the calculation of the wave function for such a state would be a formidable task, and the transition strength derived from this wave function would be rather unreliable. However, since the $\frac{1}{2}^+$ state is presumably a rather pure single particle state while the $\frac{1}{2}^-$ state involves the excitation of particles out of the O^{16} core, the E1 transition probability between these two states should be very small. Therefore, an attempt was made to fit the experimental excitation curve with the restriction $\xi^o = 0$.

In principle, it would have been possible to obtain the value of ξ^o empirically by determining the value of this parameter which gave the best fit to the experimental data. In this case, however, it would have been impossible to have obtained a meaningful value for ξ^o in this manner since the fits obtained with $\xi^o = 0$ were quite good and in themselves non-unique. While it was not possible to determine the value of ξ^o empirically, an upper limit on the magnitude of this parameter could be determined. From Eq. 2 it can be seen that the maximum possible value of $|\xi^o|$ is severely limited if, in the predicted excitation curve, the rise before the resonance is to be smaller than the dip after resonance. Since the experimental data clearly indicates that this is the case, an upper limit on $|\xi^o|$ could be obtained by determining the value of $|\xi^o|$ for which reasonable agreement with the experimental data could no longer be obtained. The limit determined in this manner was $|\xi^o| < .8$. Using the

definition $\xi = \frac{T}{M_1}$, the definition of T in terms of the ratio $\frac{\Gamma_\gamma}{\Gamma}$, and the value of M_1 determined from the empirical normalization of $g_{\frac{1}{2}^+}(r)$; this limit corresponds to:

$$\Gamma_\gamma < .03 \text{ eV}$$

According to the data given by Wilkinson (1960), the average gamma-ray width for a E1 transition of 2.6 MeV is approximately 5 eV. Thus the internal transition strength is abnormally low lending support to the hypothesis that the single particle amplitude in the wave function of the $\frac{1}{2}^-$ state is quite small.

Very good agreement could be obtained between the experimental data and the excitation curves calculated with ξ taken to be zero. Even in this case, however, where there were only two shape determining parameters, the values of R^o and φ_1 giving the best agreement with the experimental data were not uniquely determined. For a given value of R^o the best agreement was obtained over a fairly narrow range of φ_1 values, but equally good agreement could be obtained with another set of R^o and φ_1. Thus the least squares fit to the experimental data defined a long narrow strip in R^o φ_1 space; this region of best agreement is shown schematically in Fig. 10 together with a curve giving R^o as a function of the cutoff radius r_o. This figure has been included to illustrate the fairly wide range of parameters for which equally good agreement with the experimental data could be obtained even though the internal transition parameter was arbitrarily taken to be zero. The extent and location of this region of best agreement would, of course, change if ξ were taken to be different from zero; thus the region illustrated in this figure

should not be interpreted as defining the only combinations of R^o and φ_1 for which good agreement with the experimental data was possible. The agreement obtained between the calculated excitation curve and the experimental data is illustrated in Fig. 8. The solid curve in this figure was calculated for $R^o = .71$ and $\varphi_1 = .05$ rad; this value of R^o corresponds to $r_o = 5.1$ f. The empirical normalization of the bound state function given by this least squares fit to the experimental data yielded a single particle reduced width for the $\frac{1}{2}^+$ state of:

$$\theta^2_{\frac{1}{2}^+sp} = .57 \pm .10 \qquad\qquad r_o = 5.1 \text{ f}$$

Where the definition of Lane (1958) has been used for θ^2_{sp}, that is

$$\theta^2_{\frac{1}{2}^+sp} = \frac{r_o^3}{2}\left\{g^{\frac{1}{2}}_b(r_o)\right\}^2$$

This result refers to the least squares fit obtained for $r_o = 5.1$ f, but the results obtained for r_o in the range 4.6--5.6 f were within $\pm$ 2% of the value obtained for $r_o = 5.1$ f.

C. Comparison With γ_1 Results

Integrating the γ_1 differential cross section given in Appendix IV over the detector in the manner previously described for γ_2, yields the following expression for the predicted γ_1 excitation function.

$$\sigma_{xtal} = \frac{18}{25} K \frac{E_{\gamma_1}^3}{E_p^3} \left[\begin{array}{l} 1.15\ N_1(N_1 - 2D_1\phi_1) + 1.87\ N_3(N_3 - 2D_3\phi_3) \\ \\ -\ .61\ N_1N_3(\cos\beta - \phi_1\sin\beta) + .61\cos\beta(N_1D_3\phi_3 + N_3D_1\phi_1) \end{array} \right] \qquad (3)$$

Where:

K is the same constant as in the case of γ_2

N_1 and D_1 are the two E1--P wave capture matrix elements

$$N_1 = \int_{r_o}^{\infty} g_b^{\frac{5}{2}^+}(r)\ F_1(kr) r^2 dr \qquad D_1 = \int_{r_o}^{\infty} g_b^{\frac{5}{2}^+}(r)\ G_1(kr) r^2 dr$$

N_3 and D_3 are the two E1--F wave capture matrix elements

$$N_3 = \int_{r_o}^{\infty} g_b^{\frac{5}{2}^+}(r)\ F_3(kr) r^2 dr \qquad D_3 = \int_{r_o}^{\infty} g_b^{\frac{5}{2}^+}(r)\ G_3(kr) r^2 dr$$

Here $g_b^{\frac{5}{2}^+}(r)$ is the bound Coulomb function for $\ell = 2$ and a binding energy of .598 MeV corresponding to the $\frac{5}{2}^+$ state of F^{17}; the other terms in the integrals are defined as in the case of γ_2.

ϕ_1 is defined as in the case of γ_2

ϕ_3 is the negative of the common $F_{\frac{5}{2}}$, $F_{\frac{7}{2}}$ potential phase shift.

$\beta = \sigma_3 - \sigma_1$ where σ_ℓ is the Coulomb phase shift as defined by Lane and Thomas, page 267 (1958).

In fitting this expression to the experimental γ_1 data, the values of r_o and ϕ_1 were taken to be those previously found to give a good fit to the γ_2 data. The potential phase shift-ϕ_3 was taken to be that given by a hard sphere of radius r_o; thus the only free parameter for a given choice of r_o was the normalization of the bound state function $g_{\frac{5}{2}^+}(r)$. The normalization was determined empirically from the least squares fit to the experimental data in exactly the same manner as for γ_2. Good agreement between the calculated excitation curve and the experimental data could be obtained over the entire range of r_o and φ_1 values obtained by the least squares fit to the γ_2 data. However, since the calculated excitation curve was very nearly a straight line and the γ_1 data had rather large statistical errors, the fact that good agreement could be obtained over a large range of parameters is not very surprising. Figure 9 shows the result of the least squares fit to the experimental data for $r_o = 5.1$ f and $\varphi_1 = .05$ rad.

The single particle reduced width for the $\frac{5}{2}^+$ state as deduced from the empirical normalization of the bound state function was:

$$\theta^2_{\frac{5}{2}^+sp} = .38 \pm .08 \qquad \text{for } r_o = 5.1 \text{ f}$$

The results for r_o in the range 4.6—5.6 f were within $\pm$ 10% of this value.

D. Total Capture Cross Section

Once the parameters giving the best fit to the two excitation curves had been determined, these could be used together with the expressions given in Appendix IV to compute the γ_1 and γ_2 capture cross sections as a function of the bombarding energy. These two cross

sections together with their sum representing the total cross section for the $O^{16}(p,\gamma)$ reaction are shown in Fig. 11; these cross sections were computed for the set of parameters r_o = 5.1 f, φ_1 = .05 rad, $\theta^2_{\frac{1}{2}}+sp$ = .57, and $\theta^2_{\frac{5}{2}}+sp$ = .38. The γ_1 cross section is approximately 3.7 μbarns, and the average γ_2 cross section is roughly 8.7 μbarns. The anomaly in the total capture cross section is approximately ± 20% of the nonresonant value.

The error common to the γ_1 and γ_2 cross sections due to the uncertainty in the photopeak detection efficiency and the oxygen content of the target has not been indicated in Fig. 11. This common error would simply multiply each of the curves by some factor but would not change their shape. In terms of this common multiplicative factor, the common error is estimated to be (1 ± .18). The error indicated on the γ_1 curve is due to the additional uncertainty in the γ_1 photopeak detection efficiency relative to the ThC" calibration; the error bar indicates the range over which the curve could be displaced parallel to the horizontal axis. The uncertainty in the photopeak efficiency actually results in a multiplicative error factor, but since the γ_1 cross section is nearly constant, this multiplicative factor can be approximated by an additive error. This same additive error is, of course, also present in the total cross section curve.

The effect of changing the parameters used in the computation of these cross sections from those determined for r_o = 5.1 f to those determined for some other value of r_o was found to be very small. The variation in the γ_2 cross section over the range of "best fit" parameters shown in Fig. 10 was found to be less than 1%; the variation in the γ_2

cross section over the same range of parameters was approximately 2%, and the variation in the total cross section was only about 1%.

If the total cross section curve of Fig. 11 is compared with the experimental curve given by Laubenstein et al. (1951), it can easily be seen that the scatter in their data is approximately of the same magnitude as the anomaly which they should have observed. Thus the fact that no anomaly was observed can be understood in terms of the rather poor statistical accuracy of their data and the relatively small size of the anomaly.

Using the empirical reduced widths obtained from the present experiment, the total capture cross section was computed for a bombarding energy of .616 MeV corresponding to the low energy measurements of Tanner (1959). In this calculation a r_o value of 5.1 f was used, and the $\ell = 3$ and $\ell = 1$ phase shifts were taken to be those given by a hard sphere of radius r_o. The γ_2 cross section was found to be .31 μbarns, and the γ_1 cross section was .04 μbarns. The total capture cross section given by this calculation was, therefore, .35 ± .03 μbarns. The experimental value given by Tanner is .29 ± .03 μbarns. Thus the calculated cross sections is in good agreement with the experimental value.

The exact value of the cross section calculated for a bombarding energy of .616 MeV was found to be strongly dependent upon the value or r_o; changing r_o by less than 5% from 5.1 f to 4.8 f, reduced the total cross section by approximately 10% from .35 to .32 μbarns. In contrast, the cross sections shown in Fig. 11 were found to be nearly independent of the value of r_o used in the computation. This apparent contradiction

is due to the fact that the parameters used in calculating the cross sections shown in Fig. 11 were obtained from a least squares fit to the experimental excitation curves; in particular, φ_1 was allowed to vary with R^o so as to give the best fit to the experimental data. This process resulted in φ_1 varying with r_o in such a manner that the calculated cross section was nearly independent of r_o.

The γ_2 cross section calculated for a bombarding energy of .616 MeV was very insensitive to the exact value of φ_1; the γ_1 cross section, while rather sensitive to the value of φ_1, was much smaller than the γ_2 cross section. Thus the total capture cross section at this bombarding energy was quite insensitive to any error made in assuming φ_1 was given by the hard sphere phase shift.

E. Conclusion

Thus, in summary, it has been found that an anomaly does exist in the γ_2 yield for bombarding energies corresponding to the region of the 3.10-MeV state of F^{17}, and that within the experimental error no anomaly exists in the γ_1 yield. It was possible to fit the observed γ_1 and γ_2 excitation curves with expressions computed on the basis of a simple extranuclear calculation of the capture matrix elements using reasonable values for the cutoff radius and the $\ell = 1$ potential phase shift. On the basis of the experimental data and the extranuclear model, it was possible to obtain the single particle reduced widths for the $\frac{5^+}{2}$ ground state and the $\frac{1}{2}^+$ .500-MeV state of F^{17}, and to establish an upper limit on the width of the gamma-ray transition from the $\frac{1}{2}^-$ 3.10 MeV state to the $\frac{1}{2}^+$ .500-MeV state. The values thus obtained were:

$$\theta^2_{\frac{1}{2}+sp} = .57 \pm .10 \qquad \theta^2_{\frac{5}{2}+sp} = .37 \pm .08 \qquad \Gamma_\gamma < .03 \text{ eV}$$

In addition, the total capture cross section was computed for a bombarding energy of .616 MeV and was found to be in good agreement with the experimental results of Tanner (1959).

The large value of the empirical single particle reduced widths for the $\frac{1}{2}^+$ and $\frac{5}{2}^+$ states is in good agreement with their respective identifications as nearly pure 2S and 1D single particle states. It is interesting to compare the empirical reduced widths with the reduced widths calculated from a simple single particle model using a square well interaction of radius r_o with the depth adjusted to give the correct binding energy for the state under consideration. The reduced width calculated for the 2S level on the basis of this model was within 10% of the empirical reduced width for the $\frac{1}{2}^+$ state. The reduced width calculated for the 1D state on the basis of this model was approximately 1.6 times the empirical reduced width for the $\frac{5}{2}^+$ state. A more realistic shape for the interaction potential would probably tend to reduce the value of the reduced width for the 1D state, and thus bring it into closer agreement with the empirical value. In any case the agreement of the model reduced widths with the empirical values is surprisingly good.

The ratio of the empirical reduced width for the $\frac{1}{2}^+$ state to that for the $\frac{5}{2}^+$ state is approximately 1.5. This is considerably smaller than the ratio of 4.8 estimated by Macfarlane and French (1960) on the basis of an analysis of the $O^{16}(d,n)$ stripping results. This discrepancy is not very alarming, however, in view of the very small binding energy of the $\frac{1}{2}^+$ state and the statement by Macfarlane and French that the simple Butler stripping theory used in their analysis is particularly unreliable for low binding energies. The ratio of 1.5 is in fairly good agreement

with the value of 2 given by Macfarlane and French for the ratio of the reduced widths of $\frac{1^+}{2}$ and $\frac{5^+}{2}$ levels in the mirror nucleus O^{17} as deduced from the $O^{16}(d,p)$ stripping results.

While the agreement of the extranuclear model with the existing $O^{16}(p,\gamma)$ data appears to be quite good, it would be extremely useful to have other measurements of the γ_1 and γ_2 cross sections available for further comparison. In particular, a series of fairly accurate measurements over a wide range of bombarding energy would allow the ability of the model to reproduce the data with a fixed value of the cutoff radius and a smoothly varying potential phase shift to be checked. The main difficulty encountered in such a detailed comparison of the experimental and calculated cross sections is that at the higher bombarding energies it becomes quite important to have fairly accurate values for the phase shifts involved. It is often extremely difficult to extract these phase shifts from the scattering data with sufficient accuracy to make such a detailed comparison possible.

An alternative approach, which might prove useful in the case of a closed shell target nucleus such as O^{16}, would be to try to represent the nonresonant scattering by means of some fairly realistic potential between the target nucleus and the captured proton. If a potential could be devised which reproduced the scattering data fairly well, then it could be used to provide a consistent set of phase shifts and to remove the artificial cutoff of the capture matrix elements at r_o. Although the phase shifts obtained from such a potential would probably not produce the best possible agreement with the scattering data, the use of such a model would allow the capture cross section to be computed in an unambiguous manner.

The capture cross section computed on the basis of this model could then be compared with the experimental data to provide a further check upon the validity of the potential. Of course a simple one particle potential could not be used to treat a resonant state. Thus, in the region of a resonance, some reasonably consistent method would have to be devised whereby the resonance could be treated by a formalism similar to R matrix theory while the nonresonant scattering was treated by means of the single particle potential.

APPENDIX I

Target Preparation and Analysis

The targets used in this experiment consisted of tungsten blanks which had been oxidized by heating them in an oxygen atmosphere by means of an induction furnace. The blanks were rectangles approximately 1" x $\frac{1}{2}$" cut from tungsten sheet; during the initial phases of the experiment .010" stock was used, but the target used to obtain the data presented here was made from .040" stock. The .010" stock could be sheared to form the blanks, but the .040" could not be sheared without shattering and was, therefore, cut into blanks by the use of very thin abrasive wheels. The blanks were polished to a mirror-like finish by the use of ordinary abrasive paper starting with 200 grade and gradually moving to finer grades until the final polishing stage using 4/0 paper was reached.

The polished blank was first cleaned in benzine and acetone to remove organic contaminants and then in hot concentrated HNO_3 followed by hot concentrated KOH. The blank was then rinsed several times with distilled water and placed in the oxidation chamber; this consisted of a quartz tube positioned within the field coil of a radio frequency induction furnace. To minimize the contact area between the blank and the walls of the tube, the blank was held between the ends of two smaller quartz tubes; these support tubes had shallow slots cut in their ends to receive the blank. Thus the only portion of the blank in contact with quartz was a narrow strip at each end. The outer quartz tube was inserted into a small vacuum chamber by means of an "O" ring placed around the mouth of the tube. The vacuum chamber was equipped with a large valve

so that it could be connected to or isolated from a high vacuum pumping line. The chamber was also provided with a mercury manometer and a needle valve inlet so that after the chamber had been evacuated and isolated from the pumping line, the desired amount of oxygen gas could be admitted.

After the blank had been placed in the quartz tube, the system was pumped on until a vacuum of approximately 10^{-4}--10^{-5} had been achieved. The induction furance was then used to heat the blank to a brilliant white heat in order to remove any remaining surface contaminants. After the target had cooled for 5-10 minutes, the valve to the pumping system was closed, and oxygen was admitted into the chamber by means of the needle valve.

Oxygen depleted in O^{18} was used in the oxidation of the blanks in order to reduce the background due to the neutrons produced in the $O^{18}(p,n)$ reaction. The oxygen was obtained by electrolysis of water depleted by a factor of approximately 2.7 in O^{18}; this water was obtained from the Weizmann Institute of Science, Rehovoth, Israel. The depleted oxygen was stored in a small stainless steel cylinder. In order to trap out possible contaminants in the gas, the cylinder was cooled to liquid nitrogen temperatures whenever any oxygen was removed from it for use in target preparation. Immersing the cylinder in liquid nitrogen also greatly facilitated admitting a small amount of gas into the oxidation chamber since the pressure dropped to the vapor pressure of the liquid phase at this temperature. The optimum pressure for oxidation was dependent upon the target thickness desired; for the targets used in the present experiment which were approximately 10 keV thick for 2.6 MeV protons, a pressure of 3-5 Torr was used.

The blank was oxidized by heating it to an orange-red heat in the oxygen atmosphere until the color of the oxide layer indicated that the desired thickness had been reached. It was found that a much more uniform target could be produced if the blank was heated in short bursts so that the target, while never cooling off completely, underwent a considerable variation in temperature. The improved uniformity in the oxide obtained with this method of heating was undoubtedly due to the fact that it produced a more uniform average temperature over the surface of the blank. There was considerable latitude in the oxygen pressure and oxidation temperature which could be used to produce a given oxide thickness. If too low an oxygen pressure was used, however, the oxide layer could not be made sufficiently thick, and too high an oxidation temperature tended to evaporate the oxide as soon as it was formed. In fact, the ability to evaporate a thin oxide layer proved to be quite useful in target preparation since it allowed one to remove a poor oxide layer without removing the blank from the oxidation chamber.

The thickness of the oxide layer was determined roughly from its color by the use of an empirical color code. The thinnest layer which could be produced by this method of oxidation had a brilliant transparent yellow color which changed to red, then to green, and then to blue as the oxide thickness increased. After the appearance of this first blue color, the oxide layer became redish blue with the blue becoming more predominant as the oxidation continued. At the appearance of the second pure blue color, which was much deeper and less transparent than the first, the oxide layer was found to be approximately 10 keV thick for 2.6 MeV protons. If the oxidation was continued past this second

blue stage, the target color changed to a deep purple which gradually became darker until the target was almost black. Targets having this deep purple color were found to be approximately 20 keV thick for 2.6 MeV protons, but as the oxide color changes only slowly with further oxidation, this "color code" would not be useful for evaluating targets thicker than 20 keV. The targets used in this experiment were approximately 10 keV thick for 2.6 MeV protons and were of the deep blue color described above.

After the desired thickness had been attained, the valve leading to the pumping system was opened, and the chamber was again pumped down to 10^{-4}--10^{-5} Torr. When this vacuum had been reached, the target was heated several times to a dull red heat in an attempt to stabilize the target against a large initial loss of oxygen. Although considerable difficulty had been experienced in trying to produce thin uniform targets with the .010" tungsten stock, the .040" tungsten stock allowed sufficiently uniform heating so that, except for a very narrow region along the edges, the targets showed a very uniform color. After being removed from the oxidation chamber, the targets were either placed immediately in the target chamber or stored in a vacuum jar. Sufficient Na would accumulate on a target stored in air to show a strong 1.63 MeV gamma ray from the Na^{23} (p,α) reaction; this gamma ray was not observed with targets stored in a vacuum.

In the initial runs using targets made from .010" tungsten stock, considerable difficulty was experienced with loss of oxygen from the target during the bombardment. In an early study the target was clamped at only one end so that the main body of the target blank was completely free;

in some of these runs the target spot would lose practically all of its oxygen after a few hours bombardment and take on the appearance of bare tungsten. To try to prevent this loss the targets were clamped against a copper backing which was connected with a cooling arrangement so that the target could be held at room temperature during the bombardments. With this system it was found that the severe loss no longer occurred, but there was still an occasional loss of oxygen during the course of a bombardment. Thus, in designing the target holder for the final system, provisions were made for maintaining the target at a temperature considerably below room temperature and assuring good thermal contact between the copper backing and the target blank. While this system greatly reduced the magnitude and frequency of the oxygen loss, a slight loss was still occasionally observed in the course of a 12-14 hour run. These losses did not take place gradually over the course of the run but rather in the period of a few minutes; they were never of sufficient magnitude to cause any change in the physical appearance of the target spot. It was conjectured that even though the oxide layer on the reverse side of the target was very thin, it might prevent good thermal contact between the target blank and the copper backing. To check this hypothesis, the layer was removed from a target by the use of abrasive paper; however this target showed the same loss under bombardment as the targets in which the layer had not been removed. When the thickness of the tungsten stock was increased from .010" to .040" in an effort to produce more uniform targets, the problem of the oxygen loss was apparently solved. No evidence of oxygen loss was found in any of the data taken with targets made from the .040" tungsten stock.

The behavior of the oxygen loss, especially its disappearance when the thick tungsten stock was employed, suggests that the loss was due to local heating of the beam spot. This explanation is also supported by the subsequent observation that no loss was experienced with targets made from the .010" stock when they were bombarded with a poorly focused beam even though the target cooling was so poor that the entire blank was glowing red hot. Similarly, when a bare tungsten blank was bombarded with a well focused beam, a small dimple was raised at the spot of bombardment even though the total energy dissipated in the target was extremely small. However, when the same blank was bombarded with a diffuse beam of sufficient magnitude to raise the blank to a white heat, no such dimple was formed. Unfortunately, a small beam spot was necessary in the present experiment in order to achieve adequate energy resolution and lateral position stability of the beam; thus the problem of oxygen loss was encountered.

During the course of the experiment, the target thickness was crudely determined by measuring the apparent width of the narrow $O^{18}(p,p')$ resonance at 2.71 MeV. In order to be able to compare the experimental results with the model calculations, however, it was necessary to determine the total oxygen content of the target and the approximate composition of the oxide layer as a function of the penetration depth. The target composition was determined by measuring the energy distribution of the protons scattered elastically from the tungsten nuclei in the oxide layer for the case in which the initial proton beam was essentially monoenergetic. These measurements were made using the electrostatic analyser and 16" magnetic spectrometer of the 3 MeV accelerator. The

capture data was taken with an angle of 40° between the incident beam and the normal to the target blank; therefore in the scattering measurements the magnetic spectrometer was set at 80° to the incident beam, and the target was oriented so that its normal was at 40° to the beam. Thus both the incident and scattered beam were at the same angle with respect to the target normal as the incident beam in the capture measurements. Since the atomic weight of tungsten is approximately 184, the energy of a proton scattered elastically from a tungsten nucleus differs by less than 1% from its incident energy. Thus, since the incident and scattered beam made the same angle with respect to the target normal and had very nearly the same energy, the target profile appropriate to the capture experiment was given by the scattering profile* with the energy scale divided by two.

The target profile was obtained by holding the acceptance energy of the magnetic spectrometer constant while the bombarding energy was varied. In order for a scattered proton to be passed by the spectrometer, its energy loss in the target had to be such that the initial energy minus this loss corresponded to an energy within the acceptance range of the magnet. Figure 12 shows a typical profile obtained in this manner; the bombarding energy here was 2.66 MeV. As the bombarding energy was raised from below the magnet setting, the first counts were due to protons in the high energy tail of the beam distribution scattering from the very front of the target into the low energy tail of the magnet acceptance. The yield increased rapidly as the bombarding energy was increased above this threshold due to the rapidly increasing overlap of the beam spread and magnet acceptance. As the bombarding energy was increased further, the rate of the increase in the yield became much smaller until finally

---

*This refers to the profile obtained after correction for the instrumental resolution.

a plateau was reached where an increase in the bombarding energy did not change the yield. The onset of this plateau indicated that the bombarding energy was just sufficient so that the least energetic particles in the beam could be scattered from the front edge of the target and lie within the low energy tail of the magnet acceptance. Increasing the bombarding energy above this point simply moved the lamina "sampled" by the magnet further into the target. If the oxide layer had been perfectly uniform this plateau would have been flat until the back of the layer was reached where the yield would have risen again to a new plateau due to scattering in the pure tungsten backing. Actually, the oxide layer was not uniform and did not end abruptly, but rather the ratio of oxygen to tungsten decreased gradually toward the back of the layer until the pure tungsten backing was reached. Thus in Fig. 12 the first plateau is not flat but rises gradually until the level of the second plateau is reached. Target profiles such as that shown in Fig. 12 were taken for bombarding energies of 2.66, 2.16, and 1.66 MeV.

The shape of the profile observed in the elastic scattering is the result of folding together the beam resolution, target composition, beam straggling in the target, and the acceptance function of the magnetic spectrometer. To extract the combination of the target composition and beam straggling appropriate to the capture experiment, it is useful to compare the expression for the scattering profile with that for the capture cross section. To do this let:

$q(E_B,E')$ be the function describing the energy spread of the incident beam such that for a bombarding energy E_B, $q(E_B,E')dE'$ is the fraction of the beam in the interval dE' at an energy E'.

$\omega(E',E'',x)$ be the function describing the energy loss and straggling of the beam in the target. It will be defined in such a way that the probability that a proton incident upon the target with an energy E' will be found at a depth x within the target to have an energy within the interval dE" at E" is given by: $\omega(E',E'',x)dE''$. For convenience the depth x will be measured in terms of the mean energy loss suffered by a proton in reaching this point rather than in terms of the actual physical depth.

$\rho_W(x)$ be the density of tungsten (oxygen) atoms such
$\rho_O(x)$ that the number of atoms per cm^2 in a lamina dx at a depth x is given by: $\rho(x)dx$

$S(E'',E_M)$ be the relative acceptance of the magnetic spectrometer for a proton of energy E" when set at an energy E_M.

$\sigma(E'')$ be the capture cross section for protons of energy E".

Then the scattering and capture yields are given by:

$$Y_{scatt.}(E_B,E_M) = K_1 \int_0^\infty \int_0^\infty \int_0^\infty q^E(E_B,E')\omega(E',E'',x)\rho_W(x)S(E'',E_M)\, dE'\, dx\, dE''$$

$$Y_{capt.}(E_B) = K_2 \int_0^\infty \int_0^\infty \int_0^\infty q^M(E_B,E')\omega(E',E'',x)\rho_O(x)\sigma(E'')\, dE'\, dx\, dE''$$

Where K_1 and K_2 are constants depending upon the bombarding charge, detection efficiency, etc., and the superscripts on the beam functions refer to the electrostatic and magnetic analysers. The scattering cross section for tungsten has been assumed to be constant over the energy range spanned by the oxide layer, and it has, therefore, been taken outside the integral and placed in K_1. This is clearly a valid approximation since the oxide layers under consideration here are only 10 keV thick for 2.6 MeV protons.

Denoting the number of tungsten and oxygen atoms per cm^3 at a depth x within the target by $n_W(x)$ and $n_O(x)$, and the atomic stopping cross sections for this bombarding energy by ϵ_W and ϵ_O, one obtains:

$$\rho_W(x) = \frac{n_W(x)}{n_W(x)\epsilon_W + n_O(x)\epsilon_O} \qquad \rho_O(x) = \frac{n_O(x)}{n_W(x)\epsilon_W + n_O(x)\epsilon_O}$$

Thus

$$\rho_O(x) = \frac{1 - \rho_W(x)\epsilon_W}{\epsilon_O}$$

Performing the integration over x in the two yield expressions and letting:

$$\int_0^\infty \omega(E',E'',x)\rho_W(x)\,dx = f_W(E',E'') \qquad \int_0^\infty \omega(E',E'',x)\rho_O(x)\,dx = f_O(E',E'')$$

Then using the relation between $\rho_O(x)$ and $\rho_W(x)$ given above one obtains:

$$f_O(E',E'') = \frac{1}{\epsilon_O}\int_0^\infty \omega(E',E'',x)\,dx - \frac{\epsilon_W}{\epsilon_O} f_W(E',E'')$$

Since the probability that a proton of incident energy E' will be found somewhere within the target to have an energy E" is unity for E" ≤ E'

$$\int_0^\infty \omega(E',E'',x)\,dx = 1 \qquad E'' \leq E'$$

$$= 0 \qquad E'' > E'$$

Thus

$$f_o(E',E'') = \frac{1 - \epsilon_W f_W(E',E'')}{\epsilon_o} E'' \leq E' \qquad (1)$$

Inserting the expressions for f_o and f_W in the yield expressions we obtain

$$Y_{scatt.}(E_B,E_M) = K_1 \int_0^\infty \int_0^\infty q^E(E_B,E') f_W(E',E'') S(E'',E_M)\,dE'\,dE''$$

$$Y_{capt.}(E_B) = K_2 \int_0^\infty \int_0^\infty q^M(E_B,E') \frac{1 - \epsilon_W f_W(E',E'')}{\epsilon_o} \sigma(E'')\,dE'\,dE''$$

Thus, because of the connection between f_o and f_W, it is not necessary to separate the effects of the straggling from the target composition; only the combined function f_W need be determined.

In order to obtain f_W from the scattering profile, it is necessary in general to know both the beam resolution function q^E and the spectrometer acceptance function S. The combined beam and spectrometer resolution was determined from the scattering profile measured for a tungsten blank having a very smooth mirror-like surface. The scattering profile

measured for this blank could be fit with an error function* to within the experimental error; this indicated that the combined resolution function could be taken to have a Gaussian form. It was then reasonable and consistent to assume that both q^E and S have Gaussian forms, for folding two Gaussians together produces another Gaussian. Both the front and rear slopes** of the target profile could be fit with error functions to within the experimental error; this fit is shown in Fig. 12 as the solid curve. The front slope of the target profile was identical to that observed with the smooth tungsten blank indicating that it was entirely due to the resolution of the beam and the magnetic spectrometer. Using the fact that folding a Gaussian with an error function produces another error function, it was then consistent to assume that f_W had the form of a step function followed by an error function leading to the pure tungsten plateau. Folding such a f_W with the Gaussian beam resolution would produce error function front and rear slopes, and the subsequent folding with the Gaussian magnet acceptance would again produce error function slopes. Thus, since such a form was both reasonable and consistent with the scattering profile, f_W was assumed to have the form of a step function followed by an error function leading to the pure tungsten plateau.

Once the form of f_W had been assumed, only the proper scale factor remained to be determined. This factor could be determined most easily

---

*Error function is taken here to mean a function of the form

$$f(x) = \int_{-\infty}^{x} e^{-\xi^2} d\xi$$

**The front slope is that leading to the oxide plateau; the rear slope is that leading from the oxide plateau to the pure tungsten plateau.

from Eq. 1 connecting $f_o(E',E")$ and $f_W(E',E")$; these two quantities are explicit functions only of the energy loss in the target (E'-E"). For values of (E'-E") much larger than the thickness of the oxide layer, $f_o(E',E")$ must be zero since there will be no probability of finding a particle with such a large loss inside the oxide region. From Eq. 1 this implies that in the region of the tungsten plateau, $f_W(E',E")$ must be equal to $\frac{1}{\epsilon_W}$; this result can also be obtained directly from the definition of $f_W(E',E")$. The values of ϵ_o were taken from the curves in Whaling (1958), and the values of ϵ_W were approximated by the values given for tantalum (Whaling, 1962). Since for tungsten Z = 74 while for tantalum Z = 73, approximating the stopping cross section for tungsten by the value for tantalum should be valid to within the 5% uncertainty quoted for the tantalum results. The function $f_o(E',E")$ obtained in this manner for a bombarding energy of 2.66 MeV is shown in Fig. 13.

After the function $f_o(E',E")$ had been determined, it was folded with the beam resolution for the magnetic analyser to form the combined beam resolution—target composition function $t(E_B,E")$. That is:

$$t(E_B,E") = \int_o^\infty q^M(E_B,E')\, f_o\,(E',E")\, dE'$$

Figure 14 shows this function for a bombarding energy of 2.66 MeV corresponding to the $f_o(E',E")$ of Fig. 13 and the magnetic analyser resolution of 3.0 keV described on page 14. Thus, to correct the theoretical capture cross section for the effects of the beam spread and target thickness, it was only necessary to fold it with the function $t(E_B,E")$.

$$Y_{capt.}(E_B) = K_2 \int_o^\infty t(E_B,E'')\ \sigma(E'')\ dE''$$

It was useful to determining the total number of oxygen atoms per cm^2 of beam;* this number could be obtained by observing.

$$\int_o^\infty \rho_o(x)\ dx = \text{number of oxygen atoms per } cm^2 \text{ of beam}$$

But

$$\int_o^\infty \omega(E',E'',x)\rho_o(x)\ dE''\ dx = \int_o^\infty f_o(E',E'')\ dE'' = \int_o^\infty \rho_o(x)\ dx$$

Thus this number was given by the area under the $f_o(E',E'')$ curve. This area was determined for the profiles taken at 2.66, 2.16, and 1.66 MeV, and the results, which agreed to within the experimental error, yielded.

$$\text{Oxygen atoms per } cm^2 \text{ of beam} = (1.17 \pm .17) \times 10^{18}$$

The target composition at the front edge of the target was given by the ratio $\frac{n_o}{n_W}$ determined from the target profile.

$$\frac{n_o}{n_W}\ (\text{front edge}) = \frac{\epsilon_W}{\epsilon_o}\left\{\frac{\text{Yield at front edge}}{\text{Yield at W plateau}} - 1\right\}$$

The front edge compositions determined from the target profiles taken at 2.66, 2.16, and 1.66 MeV agreed to within the experimental uncertainty and yielded.

$$\frac{n_o}{n_W} = 2.6 \text{ or in other words } WO_{2.6}$$

---

*This means the number of oxygen atoms contained within the volume swept out by 1 cm^2 of beam. As has been the case in the entire discussion of the target composition, the 40° angle between the target normal and the beam direction is automatically included.

APPENDIX II

Photopeak Corrections

In this appendix a detailed description will be presented of the method used to correct the raw γ_1 and γ_2 photopeak yields for the effects of γ_2—γ_3 summing and the contribution of the Compton distribution and the first escape peak of γ_1 to the photopeak region of γ_2. Let us consider first the process of γ_2—γ_3 summing.

A. γ_2—γ_3 Summing

The mean life of the .500-MeV state of F^{17} has been measured to be 4.45×10^{-10} sec (Kane, 1960). This mean life is a great deal shorter than the decay time of the NaI(Tl) scintillator; thus, if both γ_2 and the cascade γ_3 interacted with the scintillator, the two interactions would have been "summed" by the scintillator into a single light pulse. Since the .500-MeV state has $J = \frac{1}{2}$, there was no angular correlation between γ_2 and γ_3; thus the probability, that for a given γ_2 interaction with the crystal the corresponding γ_3 also interacted, is given by the total detection efficiency for γ_3.

Let:

$\eta_{\gamma_2}(E')$ be the spectral function for γ_2, that is the percentage of the total γ_2 counts* which are located in the channel of energy E'.

$\eta_{\gamma_3}(E')$ be the spectral function for γ_3.

ϵ_{γ_3} be the total detection efficiency for γ_3.

N_{γ_2} be the total number of γ_2 counts.*

---

*In these definitions "counts" refers to the number of counts present in a pure, single gamma ray spectrum.

Then the number of counts in the γ_2--γ_3 sum spectrum located at a channel energy E_s is given by:

$$N_s(E_s) = N_{\gamma_2}\, \epsilon_{\gamma_3} \sum_{E_s - E_{\gamma_3\,\max}}^{<E_{\gamma_2\,\max}, E_s>} \eta_{\gamma_2}(E')\eta_{\gamma_3}(E_s - E') \qquad (1)$$

Where $E_{\gamma\,\max}$ denotes the maximum energy occurring in the gamma-ray spectrum in question, and the symbol $<E_{\gamma_2\,\max}, E_s>$ means that the smaller of the two quantities is to be used. Since the effects of the summing were only of interest for the photopeak regions of γ_1 and γ_2, it was only necessary to determine $\eta_{\gamma_2}(E')$ down to $E' \approx E_{\gamma_2} - E_{\gamma_3\,\max}$, that is roughly down to the region of the first escape peak.

Since the energy of γ_3 was .500 MeV and its angular distribution was isotropic, the .478-MeV gamma ray of Be^7 source was used to obtain the total detection efficiency and the spectral function for γ_3. The spectral function η_{γ_3} was taken to be that measured for the .478-MeV gamma ray of Be^7 with the energy scale expanded so that the photopeak corresponded to an energy of .500 MeV. The spectrum of the .478-MeV gamma ray was obtained by placing a small Be^7 source on a .040" tungsten blank and positioning this blank in the target holder so that the source was in the same location as the beam spot during the accumulation of the capture data. The total detection efficiency for the .478-MeV gamma ray was determined by comparing the counting rate obtained when the Be^7 source was in the position described above with the counting rate obtained when the same source was located in a well determined "standard geometry" above the free counter assembly; the total detection efficiency for this free crystal situation was then taken from the curves of Heath (1957). Approximating

ϵ_{γ_3} by the total detection efficiency determined in this manner for the .478-MeV gamma ray of Be^7, the result was:

$$\epsilon_{\gamma_3} = .075 \pm .005$$

The spectral function η_{γ_2} was approximated by that measured for the 2.615-MeV ThC" gamma ray; here again, the source was placed on a .040" tungsten blank, and this was positioned in the target holder so that the source was in the same location as the beam spot during the capture runs. While several other gamma rays were present in the decay chain of the ThB source used for this measurement, the spectral function was only important for energies down to approximately 2 MeV, and in this region there were no other gamma rays of sufficient intensity to be troublesome. The 2.615-MeV gamma ray occurs as the final transition in a gamma cascade in Pb^{208} (Emery, 1960), and due to the rather large detection efficiency, there was considerable summing of this gamma ray with the .583-MeV gamma ray preceeding it in 87% of the cascades. In order to obtain the spectral function of the 2.615-MeV gamma ray, it was necessary to correct the observed ThC" spectrum for this summing contribution. In the calculation of this sum spectrum, the spectral function of the .583-MeV gamma ray was approximated by that measured for the .662-MeV gamma ray of Cs^{137} with the energy scale suitably contracted so that the photopeak corresponded to .583 MeV. This spectral function and the ThC" spectrum, crudely corrected for summing, were used to obtain a preliminary sum spectrum. This preliminary sum spectrum* was then normalized so that

---

*Reference to the γ_2-γ_3 sum spectrum shown in Fig. 15 may be found helpful in following this discussion. The 2.615—.583-MeV sum spectrum had much the same character as the sum spectrum η_s shown in Fig. 15. Of course, since it was necessary to correct the 2.615-MeV spectrum down to the region of the first escape peak, the sum spectrum extended to lower energies than that shown in Fig. 15.

the number of counts contained in its sum peak was equal to the number of counts observed in the sum peak of the raw ThC" spectrum. The first summing correction given by this normalized sum spectrum was then subtracted from the raw ThC" spectrum to yield the first corrected 2.615-MeV spectrum. This corrected 2.615-MeV spectrum was, in turn, folded with the .583-MeV spectrum to yield the final sum spectrum. This final sum spectrum was normalized in the manner previously described, and the final summing correction given by this normalized sum spectrum was then subtracted from the raw ThC" data. The final summing subtraction amounted to approximately 10% of the raw ThC" spectrum. The 2.615-MeV spectrum obtained after the subtraction of this final summing correction was then used to represent the spectral function η_{γ_2}.

After the two spectral functions η_{γ_2} and η_{γ_3} had been determined, they were inserted into Eq. 1, and the γ_2--γ_3 sum spectrum was calculated. The two spectral functions η_{γ_2} and η_{γ_3} and the spectral function for the γ_2—γ_3 sum spectrum, η_s, are shown in Fig. 15. For simplicity, these functions are presented in Fig. 15 in terms of a continuous energy distribution, and η_{γ_2} and η_{γ_3} have not been normalized so as to contain the same area. Thus, the vertical scale shown in Fig. 15 is completely arbitrary, and only the forms of the spectral functions but not their absolute value can be obtained from this figure. In order to facilitate comparison between the η_{γ_2} and η_s curves, they have been normalized so as to contain the same area. Thus since $\epsilon_{\gamma_3} = .075$, if the η_{γ_2} curve is taken to represent the observed γ_2 yield, then the summing contribution to the γ_1 yield is indicated by the η_s curve with the vertical scale reduced by a factor of approximately 13. To obtain a quantitative measure of the γ_2—γ_3

summing into the photopeak of γ_1, the photopeak of the η_{γ_2} spectrum and the sum peak of the η_s spectrum were approximated by Gaussians, and the photopeak summing factor was determined to be:

$$\frac{\text{Number of counts in sum peak Gaussian}}{\text{Number of counts in } \gamma_2 \text{ photopeak Gaussian}} \times \epsilon_{\gamma_3} = .041 \pm .003$$

Before this factor could be applied to the observed γ_2 photopeak yield,* it was necessary to correct this yield for the effects of γ_2—γ_3 summing into and out of the γ_2 photopeak region. To investigate this correction let:

r be the ratio between the fraction of η_{γ_2} lying in the photopeak region and the fraction of the η_s sum spectrum lying in the same area.

$N_{\gamma_2}^{orig}$ be the number of counts which would have been present in the γ_2 photopeak if there had been no summing.

$N_{\gamma_2}^{obs}$ be the number of counts observed in the γ_2 photopeak.

Then

$$N_{\gamma_2}^{obs} = \left(1 - \epsilon_{\gamma_3}(1-r)\right) N_{\gamma_2}^{orig}$$

But from the the η_{γ_2} spectrum and the η_s spectrum, one obtains $r = .87 \pm .05$,** and since $\epsilon_{\gamma_3} = .075 \pm .005$, we obtain:

---

*This refers to the photopeak yield due only to γ_2 and γ_2—γ_3 summing; it is assumed throughout this discussion that the correction to the raw γ_2 photopeak yield due to the Compton distribution and the first escape peak of γ_1 has already been applied.

**The uncertainty quoted here includes the variation in the value obtained for r depending upon whether the photopeak region of η_{γ_2} was taken to be that given by a Gaussian approximation to the photopeak or was taken to be equal to the interval used in the analysis of the capture data.

$$N_{\gamma_2}^{obs} = (.99 \pm .01) N_{\gamma_2}^{orig}$$

Thus this correction is very small since nearly as many counts are summed into the γ_2 photopeak region as are summed out of it.

B. The Compton Distribution and First Escape Peak of γ_1

In order to be able to correct the raw γ_2 photopeak yield for the counts actually belonging to the Compton distribution and the first escape peak of γ_1, it was necessary to determine the ratio between the number of counts in the γ_1 photopeak and the number of counts in that portion of the Compton distribution occupied by the γ_2 photopeak. This ratio was determined for several gamma rays having energies in the region of γ_1, and the ratio appropriate to γ_1 was then obtained by interpolation. Since the photopeak of γ_2 coincided almost exactly with the first escape peak of the γ_1 spectrum, this ratio was defined as:

$$\rho = \frac{\text{Counts in an interval } \Delta E \text{ centered about the first escape peak}}{\text{Counts in a Gaussian fit to the photopeak}}$$

The energy interval ΔE* was taken to be proportional to the energy of the first escape peak; that is:

$$\Delta E = \text{Constant } (E_\gamma - .511 \text{ MeV})$$

The constant was chosen so that for $E_\gamma = E_{\gamma_1}^{o} = 3.094$ MeV, ΔE corresponded to the 10 channel interval over which the γ_2 photopeak counts were summed.

In addition to ρ it was useful to determine the ratio δ defined in exactly the same manner except that only the counts due to the flat portion

---

*It should be noted that ΔE is used in this appendix to denote three separate energy intervals: the interval defined above, the interval over which the γ_2 photopeak counts were summed, and the interval over which the γ_1 photopeak counts were summed. Thus, in general ΔE will denote only an energy interval; the particular interval in question must be obtained from the context in which it is used.

of the Compton distribution were included in the ΔE sum. That is, the contribution of the first escape peak was not included in the determination of δ; instead the flat portion of the observed spectrum lying immediately below the first escape peak was simply extrapolated into the ΔE region. Finally, the ratio of the number of counts lying within Gaussian approximations to the first escape peak and the photopeak was determined; this ratio was denoted by τ. The method used to obtain these three ratios is illustrated in Fig. 16 for the 3.51-MeV gamma ray of the $C^{12}(p,\gamma)$ reaction at the 1.698-MeV resonance. From Fig. 16 it can be seen that $\delta + \tau$ is not exactly equal to ρ since counts are included in ρ which are due to the peak at the front edge of the Compton distribution. Figure 17 shows the results of a determination of these three ratios for the following gamma rays:

1.98-MeV γ of $O^{18}(p,p')$ at the 2.640-MeV resonance

2.365-MeV γ of $C^{12}(p,\gamma)$ at the .459-MeV resonance

2.615-MeV γ of a ThC" source (corrected for summing)

3.13-MeV γ of a S^{37} source

3.51-MeV γ of $C^{12}(p,\gamma)$ at the 1.698-MeV resonance

C. Final Results

Since the corrections to the raw γ_1 and γ_2 photopeak yields were interdependent, it was necessary to use an iterative procedure to determine them. For reasons of clarity, however, these corrections will be discussed separately and treated as if they were independent of each other. The results quoted will be those obtained in the final iteration.

1. Correction to γ_2

In order to determine the contribution of the Compton distribution and the first escape peak of γ_1 to the raw photopeak yield of γ_2, it was only necessary to multiply the factor ρ discussed in Part B by the number of counts contained in a Gaussian approximation to the γ_1 photopeak. The statistical fluctuations in the γ_1 photopeak counts were sufficiently large so that it would have been impossible to have obtained a meaningful Gaussian approximation to each of the γ_1 photopeaks. However, since the γ_1 yield showed only a very slight dependence upon the bombarding energy, the correction to the γ_2 photopeak yield should, in turn, also have only a small energy dependence. The correction was, therefore, determined for the average bombarding energy of 2.66 MeV, and then multiplied by a linear energy dependence determined from the approximate energy dependence of the γ_1 yield and the factor ρ. To determine the number of counts contained within a Gaussian approximation to the γ_1 photopeak, several runs were shifted so that the centers of their γ_1 photopeaks coincided, and these shifted spectra were added together to form a sum γ_1 photopeak. This sum photopeak was then approximated by a Gaussian, and the total number of counts contained within the Gaussian was determined. Since the runs were chosen to have bombarding energies symmetrically distributed about 2.66 MeV, the Gaussian count for a single run at this energy was taken to be that obtained by dividing the sum count by the number of runs used to obtain it. The correction to the raw γ_2 photopeak yield for a bombarding energy of 2.66 MeV was determined from this single run Gaussian count and the value of ρ for the corresponding γ_1 energy of 3.094 MeV to be 818 ± 35 counts. The linear approximation to the energy dependence of

this correction was obtained by fitting a straight line to the ρ curve shown in Fig. 17 and determining the best straight line fit to the γ_1 excitation curve. The result of this process was:

$$\gamma_2 \text{ correction } (E_p) = (818 \pm 35)\left\{1 + \frac{(.071 \pm .025)(E_p - E_p^o)}{100 \text{ KeV}}\right\}$$

$$\text{For } E_p^o = 2.66 \text{ MeV}$$

This correction amounted to approximately 18% of the raw γ_2 photopeak yield.

2. Correction to γ_1

In order to be able to use the photopeak summing factor discussed in Part A to correct the raw γ_1 photopeak yield for the counts due to γ_2-γ_3 summing, it was necessary to determine the number of counts contained within a Gaussian approximation to the γ_2 photopeak. In the analysis of the capture data, however, the γ_2 photopeak yield was determined by simply summing the counts contained within a given region ΔE centered about the photopeak. In order to be able to apply the photopeak summing factor, it was, therefore, necessary to determine the ratio* of the γ_2 photopeak yield obtained by a Gaussian approximation to the photopeak to that obtained by the simple "ΔE count" method.

It was necessary to correct the raw γ_2 photopeak counts for the contribution of the Compton distribution and the first escape peak of γ_1 before the ratio $\frac{G}{\Delta}$ could be determined. For the "ΔE count" this correction was simply that given by the product of the factor ρ and the number

---

*For simplicity this ratio will be denoted by $\frac{G}{\Delta}$ throughout the following discussion.

of γ_1 counts within a Gaussian approximation to the γ_1 photopeak. For the Gaussian approximation to the γ_2 photopeak, however, it was necessary to make this correction in a different manner. The constant background due to the flat portion of the γ_1 Compton distribution was determined from the factor δ and the γ_1 photopeak counts, and this constant background was subtracted from the region of the γ_2 photopeak before this was fit with a Gaussian. Since the first escape peak of γ_1 and the photopeak of γ_2 had very nearly the same energy, the contribution of the first escape peak was corrected for by simply subtracting the appropriate number of counts from total number of counts lying within the Gaussian approximation to the γ_2 photopeak. This correction was obtained from the factor τ and the γ_1 photopeak counts.

Here again, in order to obtain a more meaningful Gaussian approximation to the photopeak, three runs were shifted so that the centers of their γ_2 photopeaks coincided, and the resulting spectra were then added together. These runs were chosen so that their bombarding energies were symmetrically distributed about 2.66 MeV; thus the ratio $\frac{G}{\Delta}$ determined by this procedure was strictly valid only for the corresponding γ_2 energy of 2.594 MeV. The variation of this ratio over the limited range of γ_2 energies covered by the present experiment should, however, be very slight. Since, in addition, the summing correction to the γ_1 photopeak yield amounted to only 14% of the raw photopeak yield, the value of the ratio $\frac{G}{\Delta}$ determined for $E_{\gamma_2} = 2.594$ MeV was used over the entire range of γ_2 energies covered by the present experiment. The value of this ratio for $E_{\gamma_2} = 2.594$ MeV was found to be:

$$\frac{\text{Counts in Gaussian fit to the } \gamma_2 \text{ photopeak}}{\text{Counts from "}\Delta E \text{ count" method}} = \frac{G}{\Delta} = .94 \pm .04$$

Combining the above factor with the $\gamma_2 \rightarrow \gamma_3$ summing factor discussed in Part A one obtains:

$$\frac{\text{Counts in } \gamma_1 \text{ photopeak due to } \gamma_2 \rightarrow \gamma_3 \text{ summing}}{\text{Corrected } \gamma_2 \text{ photopeak counts } (\Delta E \text{ method})} = .038 \pm .005$$

This correction applies to the number of counts contained within a Gaussian approximation to the γ_1 photopeak, but as the $\frac{G}{\Delta}$ ratio for γ_1 was found to be $.97 \pm .05$, the correction was applied directly to the γ_1 photopeak yield as determined by the "ΔE count" method.

APPENDIX III

Determination of $S(\theta)$

In this appendix the method used to obtain the relative photopeak detection efficiencies for $\sin^2\theta$ and isotropic gamma-ray angular distributions will be discussed. Throughout the discussion the ratio of these two efficiencies will be denoted by $S(\theta)$.

Since only the photopeak counts were used in the present experiment, the scattering of gamma rays into the counter from the surrounding material could be neglected in the calculation of $S(\theta)$. Except for the gamma rays scattered through very small angles by the material immediately in front of the crystal face, any scattered gamma rays reaching the counter would have lost sufficient energy so that they would no longer contribute to the photopeak counts. Thus, in order to be able to calculate the relative photopeak detection efficiencies for various angular distributions, it was only necessary to determine the probability that a gamma ray emitted toward the counter in a given direction would contribute to the photopeak yield. To a good approximation both the crystal and the amount of material between the crystal face and the interior of the target chamber were symmetric about the central axis of the counter. Thus, it was only necessary to determine the probability that a gamma ray would contribute to the photopeak yield as a function of the angle between the direction of propagation and the central axis of the counter.

Before the theoretical angular distribution could be combined with the angular photopeak sensitivity of the counter, it was necessary to make a correction for the angular dependent absorption of the target

blank and the target holder. Here again, since only the photopeak counts were of interest, the absorption was calculated under the approximation that any scattering event removed sufficient energy from the photon so that it would no longer contribute to the yield. Using this approximation, the absorption in any direction could be determined from the amount of material passed through and the total attenuation coefficient for that material; these coefficients were taken from the tables of Grodstein (1957).

To determine the photopeak sensitivity of the counter as a function of the angle between the direction of the incident gamma ray and the counter axis, a ThC" source was mounted in a collimator in such a manner that by rotating the collimator this angle could be varied. The collimator consisted of cylinder of Mallory 1000 tungsten alloy 1" in diameter and 2" long which was mounted so that the axis of the cylinder coincided with the axis of the target chamber. A small ThC" source was placed within and on the axis of this collimator by means of a axial access hole; the collimating channel consisted of a radial hole having a .081" diameter. The crystal was mapped by determining the photopeak counting rate as a function of the angle between the collimation channel and the axis of the counter.

If the collimation could have been made truly effective so that only those gamma rays passing through the collimation channel could have contributed to the photopeak, this mapping would have been quite simple. In this case, however, because of the severe limitation imposed by the chamber design on the maximum diameter of the collimator, even the use of a tungsten alloy resulted in a photopeak attenuation factor of only 2.6 along a radius. Thus using the .081" collimating channel, the photo-

peak counting rate when the channel was aligned along the counter axis was only about 15% higher than with the channel at 90° to the counter axis. In order to achieve a reasonably accurate mapping, it was, therefore, necessary to accumulate a large number of counts at each angle so that the statistical error was quite small. This, in turn, necessitated quite long runs so that the decay of the source had to be carefully corrected for. Because of the strong absorption of the .583-MeV gamma ray in the collimator, there was no evidence of summing in the ThC" spectra. Hence the photopeak counts could be determined by the simple counting procedure used to obtain the raw γ_2 photopeak counts.

The result of this mapping is shown in Fig. 18; the error indicated here is just that due to counting statistics. It can be seen that, within the experimental error, the data is symmetric about $\theta = 90°$. The fact that the wings of the curve are at the same level indicates that the ThC" was well centered on the axis of the collimator. The smooth curve shown in Fig. 18 was drawn through the data points, and the background level due to the imperfect collimation was taken from the wings of this curve and is shown in Fig. 18 as the dashed base line.

The relative photopeak detection efficiencies for the $\sin^2\theta$ and isotropic angular distributions were determined by evaluating the two integrals.

$$\epsilon_{\sin^2\theta} = \iint_{\text{xtal}} \sin^2\theta(\alpha,\beta)\ \rho(\alpha,\beta)\ \chi(\alpha)\ \sin\alpha\ d\alpha\ d\beta$$

$$\epsilon_1 = \iint_{\text{xtal}} \rho(\alpha,\beta)\ \chi(\alpha)\ \sin\alpha\ d\alpha\ d\beta$$

Where

α and β are, respectively, the polar and azimuthal angles of a spherical polar coordinate system with the origin at the source location and the axis of the counter taken as the Z axis.

$\rho(\alpha,\beta)$ is the absorption in the target blank and target holder for a path given by (α,β)

$\chi(\alpha)$ is the angular photopeak sensitivity of the counter normalized to 1 at $\alpha = 0$. It is given by the curve shown in Fig. 18 using the ordinate plotted at the right; α is plotted along the upper border.

The integrals were taken over the counter solid angle as defined by the $\chi(\alpha)$ curve of Fig. 18. The result of this process for $S(\theta)$ was:

$$S(\theta) = .87 \qquad \text{For } E_\gamma = 2.615 \text{ MeV}$$

To determine the effect of a small error in the absorption on the above ratio, the absorption was taken to be zero and the ratio was recalculated. While the individual efficiencies increased by approximately 7%, $S(\theta)$ changed by only 1% to .86. This very slight dependence upon the absorption is physically reasonable since over most of the absorption region $\sin^2\theta \approx 1$ so that both distributions are affected about equally by the absorption.

To determine how sensitive $S(\theta)$ was to the exact shape of the $\chi(\alpha)$ curve, the ratio was computed for a $\chi(\alpha)$ derived on the basis of a simple attenuation model. In this model the probability that a gamma ray would contribute to the photopeak was taken to be proportional to the probability that it would be scattered within the crystal; thus this model assumed that once a gamma ray had been scattered within the

crystal, it would eventually contribute its full energy to the crystal. Thus if $d(\alpha)$ is the distance traversed through the crystal along a path given by the polar angle α, then in this model:

$$\chi(\alpha) = c\left[1 - e^{-\mu d(\alpha)}\right] \qquad \mu = \text{total attenuation coefficient for NaI}$$

The $\chi(\alpha)$ curve derived on the basis of this model was considerably flatter near the center of the crystal and dropped off more sharply near the edges than that of Fig. 18. In spite of this difference in shape, the value of $S(\theta)$ computed for the model $\chi(\alpha)$ was .88 or only about 1% different from the value obtained with the $\chi(\alpha)$ of Fig. 18.

The fact that $S(\theta)$ was not strongly dependent upon either the exact shape of the $\chi(\alpha)$ curve or the target absorption implies that this ratio should not be strongly dependent upon the energy of the gamma ray. Thus the variation of $S(\theta)$ over the range of γ_2 energies encountered in the present experiment was neglected, and the value determined for E_γ = 2.615 MeV was used. Since, as has been previously pointed out, even a rather large error in the value of $S(\theta)$ assumed for γ_1 would not cause a serious error in the predicted γ_1 excitation function, the value determined for E_γ = 2.615 MeV was also used for γ_1. Thus for both γ_1 and γ_2 the value of $S(\theta)$ was taken to be:

$$S(\theta) = .87 \pm .01$$

APPENDIX IV

Capture Calculations

In this appendix a brief derivation of the formulae used to fit the observed yield of the two capture gamma rays will be given. For γ_2 only E1 capture from the $\ell = 1$ partial wave will be considered; while for γ_1 E1 capture from both the $\ell = 1$ and $\ell = 3$ partial waves will be included. In general the notation for the capture matrix elements and angular distribution patterns will be that of Blatt and Weisskopf (1952); while the notation of Lane and Thomas (1958) will be used for the resonant phase shift.

The differential cross section for E1 capture with magnetic quantum number m is given by: (See Chapter XII of Blatt and Weisskopf)

$$\frac{d\sigma}{d\Omega} = \frac{16\pi}{9} \left(\frac{E_\gamma}{\hbar c}\right)^3 \frac{1}{\hbar v} |Q_{1m}|^2 Z_{1m} \qquad (1)$$

Where

E_γ is the energy of the capture gamma ray

v is the velocity of the proton in the laboratory system

Z_{1m} is an angular distribution factor given by:

$$Z_{1m}(\theta,\phi) = \tfrac{1}{2}\left[1 - \frac{m(m+1)}{2}\right] |Y_1^{m+1}|^2 + \tfrac{1}{2}\left[1 - \frac{m(m-1)}{2}\right] |Y_1^{m-1}|^2 + \frac{m^2}{2} |Y_1^m|^2$$

Q_{1m} is the capture matrix element which, neglecting the extremely small spin contribution, is given by:

$$Q_{1m} = \sum_{k=1}^{A} \epsilon_{eff}^k \int r_k \, Y_1^{*m}(\theta_k,\phi_k) \, \Psi_{final}^* \, \Psi_{initial} \, d\tau \qquad (2)$$

Here ϵ_{eff}^k is the effective charge of the kth nucleon corrected for the effect of recoil, and the summation is taken over all the nucleons. Since

the magnetic quantum number of the initial and final states could, in principle, be measured without affecting the present experiment, there can be no interference between the different Q_{lm}'s. Thus the complete expression for the differential capture cross section can be obtained by summing Eq. 1 over the appropriate m values.

In the present extranuclear calculation the contribution from configurations in which the captured proton is within the O^{16} nucleus will be neglected except for the resonant $\frac{1}{2}^-$ state. Thus, except for this one internal* contribution, the matrix elements will involve only the coordinates of the captured proton relative to the O^{16} core.

γ_2 Capture

Let us consider first the γ_2 capture from the $P_{\frac{1}{2}}$ and $P_{\frac{3}{2}}$ partial waves to the .500-MeV $\frac{1}{2}^+$ state of F^{17}. Then, assuming that the resonant phase shift for the $P_{\frac{1}{2}}$ partial wave is just that given by single level R matrix theory with $\frac{\Gamma_p}{\Gamma} = 1$ and treating the $\frac{1}{2}^-$ resonant state wave function by means of the phase-amplitude relation given on page 296 of the article by Lane and Thomas (1958), the initial wave function can be written as:

---

*Throughout this discussion "internal" will refer to those configurations in which the proton is within the O^{16} nucleus; "external" will refer to the configurations for which the proton is outside this nucleus.

$$\Psi^{\nu}_{int} = \frac{2\sqrt{3\pi}}{k} ie^{iw_1} \left[\sum_{JM\nu'} S^{J\nu}_{1M\frac{1}{2}\nu'} S^{J\nu}_{1O\frac{1}{2}\nu} Y^{M}_{1}(\theta,\phi)\, \chi^{\nu'}_{\frac{1}{2}} \quad X \right.$$

$$\left. \left\{ \frac{F_1(kr)}{r} + \sin(\delta^J_R - \phi^J) e^{i(\delta^J_R - \phi^J)} \left(\frac{G_1(kr) + iF_1(kr)}{r} \right) \right\} \right.$$

$$\left. + \sqrt{\frac{v\hbar}{\Gamma^{\frac{1}{2}}}} S^{\frac{1}{2}\nu}_{1O\frac{1}{2}\nu} e^{i(\delta^{\frac{1}{2}}_R - \phi^{\frac{1}{2}})} \sin\delta^{\frac{1}{2}}_R \Phi^{\nu}_{\frac{1}{2}-} \right]$$

Where

k is the wave number for the reduced mass particle.

w_1 is the difference between the Coulomb phase shifts for $\ell = 1$ and $\ell = 0$; that is, $w_1 = \sigma_1 - \sigma_o$. In general, $w_\ell = \sigma_\ell - \sigma_o = \sum_{b=1}^{\ell} \tan^{-1} \frac{\eta}{b}$ where η is the usual Coulomb parameter for the elastic scattering channel—see Lane and Thomas, page 269 (1958).

$S^{J\nu}_{1M\frac{1}{2}\nu'}$ is the ordinary Clebsch-Gordon coefficient using Wigner's notation; it is equal to the $C_{1\frac{1}{2}}(J,\nu;M,\nu')$ of Blatt and Weisskopf.

(r,θ,φ) are the coordinates of the proton relative to the O^{16} core.

$F_1(kr)$ and $G_1(kr)$ are the Coulomb functions for $\ell = 1$.

δ^J_R is the resonant phase shift given by $\delta^J_R = \tan^{-1} \frac{\frac{\Gamma}{2}}{E_R - E}$ for $J = \frac{1}{2}$; for all other J's it is zero.

ϕ^J is the potential scattering for the given J.

$\Phi^{\nu}_{1\frac{1}{2}}-$ is the internal wave function for the resonant $\frac{1}{2}^-$ state. The spherical harmonics contained within it are assumed to be of the form Y^m_1 rather than of the form $i^1 Y^m_1$ used by Lane and Thomas; the corresponding factor of i has been included in the amplitude of this state.

The final wave function for the $\frac{1}{2}^+$ state of F^{17} is given by

$$\Psi^s_{final} = g^{\frac{1}{2}^+}_b(r) \frac{\chi^s_{\frac{1}{2}}}{\sqrt{4\pi}} + \Phi^s_{1\frac{1}{2}+}$$

Where

$g^{\frac{1}{2}^+}_b(r)$ is the bound state Coulomb function for $\ell = 0$

$\Phi^s_{1\frac{1}{2}+}$ is the wave function for the internal region

Inserting these two wave functions into the expression given in Eq. 2 for Q^m_1 and using the Wigner-Eckart theorem to perform the summation over the magnetic quantum numbers, one obtains

$$Q^m_1 = \frac{\sqrt{3}\epsilon i e^{iw_1}}{k} \left[\sum_J S^{J\nu}_{lm\frac{1}{2}s} S^{J\nu}_{10\frac{1}{2}\nu} \left\{ M_1 + \sin(\delta^J_R - \phi^J) e^{i(\delta^J_R - \phi^J)} (M_2 + iM_1) \right\} + S^{\frac{1}{2}\nu}_{lm\frac{1}{2}s} S^{\frac{1}{2}\nu}_{10\frac{1}{2}\nu} T\, e^{i(\delta_R - \phi^{\frac{1}{2}})} \sin \delta_R \right]$$

Where

$\epsilon = e \frac{m_p m_{O16}}{m_p + m_{O16}} \left(\frac{1}{m_p} - \frac{8}{m_{O16}} \right)$ is the effective charge of the captured proton in the external region

$$M_1 = \int_{r_o}^{\infty} g_b^{1^+_{\frac{2}{2}}}(r) F_1(kr) r^2 dr \qquad M_2 = \int_{r_o}^{\infty} g_b^{1^+_{\frac{2}{2}}}(r) G_1(kr) r^2 dr$$

r_o is the cutoff radius corresponding to the "nuclear radius" of F^{17}

T is the parameter giving the strength of the transition taking place through the resonant $\frac{1}{2}^-$ state. It is given by the following integral over the internal region:

$$T = \frac{2\sqrt{\pi\,\hbar c}}{\epsilon S_{10\frac{1}{2}a}^{\frac{1}{2}a}} \left(\frac{2}{m_p c^2}\right)^{\frac{1}{4}} \frac{E_p^{\frac{1}{4}}}{\Gamma^{\frac{1}{2}}} \left[\sum_{n=1}^{A} \epsilon_{eff}^{n} \int_{\text{Int.Reg.}} r_n \, Y_1^{o*}(\theta_n, \phi_n) \Phi_{\frac{1}{2}}^{a*+} \Phi_{\frac{1}{2}}^{a-} \, d\tau \right]$$

Where E_p denotes the proton energy in the laboratory system. Using the time reversal invariance of the two internal wave functions, it can easily be seen that T must be real.*

Since $Z_{11} = Z_{1-1}$ and $S_{11\frac{1}{2}s}^{J\nu} S_{10\frac{1}{2}\nu}^{J\nu} = S_{1-1\frac{1}{2}-s}^{J-\nu} S_{10\frac{1}{2}-\nu}^{J-\nu}$ one need only consider the two matrix elements Q_{11} and Q_{10}. Then making the assumption that $\phi^{\frac{1}{2}} = \phi^{\frac{3}{2}} = \phi_1$ and that ϕ_1 is small enough so that only the first order terms in ϕ_1 need to be retained, one obtains.

$$|Q_{10}|^2 = \frac{3\epsilon^2}{k^2} \left[\begin{array}{l} M_1^2 - 2\, M_1 M_2 \phi_1 \\ + \frac{2}{3} \sin\delta R \cos\delta R \left(M_1 M_2 + \phi_1 (M_1^2 - M_2^2) + T\,(M_1 - \phi_1 M_2) \right) \\ + \frac{\sin^2\delta R}{9} \left((M_2 + T)^2 - 5\, M_1^2 + 2\, \phi_1 M_1 (T + 6\, M_2) \right) \end{array} \right]$$

*This is true even though the spherical harmonics have not been chosen according to the Huby phase convention (see Lane and Thomas, 269) since only one multipole is involved in the matrix element.

$$|Q_{11}|^2 = \frac{6\epsilon^2}{9k^2}\left[M_2^2 + M_1^2 + 2T(M_2 + \phi_1 M_1) + T^2\right] \sin^2\delta R$$

Summing over the final spin states and averaging over the initial spin states, one obtains the following expression for the differential cross section.

$$\frac{d\sigma}{d\Omega} = \frac{16\pi}{9}\left(\frac{E\gamma}{\hbar c}\right)^3 \left[|Q_{10}|^2 Z_{10} + |Q_{11}|^2 Z_{11}\right]$$

With $Z_{10} = \frac{3}{8\pi}\sin^2\theta$ and $Z_{11} = \frac{3}{8\pi}\left(1 - \frac{\sin^2\theta}{2}\right)$. Inserting the expressions for $|Q_{10}|^2$ and $|Q_{11}|^2$ into the above, one obtains

$$\frac{d\sigma}{d\Omega} = K \frac{E_\gamma^3}{E_p^{\frac{3}{2}}}\left[\sin^2\theta\left[M_1^2 - 2M_1M_2\phi_1 - \frac{2}{3}\sin^2\delta R\left(M_1^2 - 2\phi_1 M_1 M_2\right) + \frac{2}{3}\sin\delta R\cos\delta R\left(M_1M_2 + \phi_1(M_1^2 - M_2^2) + T(M_1 - \phi_1 M_2)\right)\right] + \frac{2}{9}\sin^2\delta R\left(M_2^2 + M_1^2 + 2T(M_2 + \phi_1 M_1) + T^2\right)\right]$$

With

$$K = \frac{1}{\sqrt{2}}\frac{e^2}{\hbar c}\frac{1}{(m_p c^2)^{\frac{1}{2}}}\frac{1}{\hbar c}\left(1 - \frac{8\,m_p}{m_{O^{16}}}\right)^2$$

E_p is in the laboratory system.

Integrating the differential cross section over 4π, yields the following expression for the total cross section.

$$\sigma = \frac{8\pi}{3} K \frac{E_\gamma^3}{E_p^{\frac{3}{2}}}\left[M_1^2 - 2M_1M_2\phi_1 + \frac{2}{3}\sin\delta R\cos\delta R\left(M_1M_2 + \phi_1(M_1^2 - M_2^2) + T(M_1 - \phi_1 M_2)\right) - \frac{\sin^2\delta R}{3}\left(M_1^2 - M_2^2 - 4\phi_1 M_1 M_2 - 2T(M_2 + \phi_1 M_1) - T^2\right)\right]$$

If that portion of the cross section due entirely to the internal transition is compared with the usual Breit-Wigner expression in terms of a gamma-ray partial width, the ratio $\frac{\Gamma_\gamma}{\Gamma}$ can easily be expressed in terms of the parameter T. The result of this comparison is:

$$\frac{\Gamma_\gamma}{\Gamma} = \frac{2\sqrt{2}}{9} \frac{e^2}{\hbar c} \left\{ \frac{m_{O16}}{m_p + m_{O16}} \right\}^2 \left(1 - \frac{8m_p}{m_{O16}} \right)^2 (m_p c^2)^{\frac{1}{2}} \left(\frac{E_\gamma}{\hbar c} \right)^3 \frac{T^2}{(E_p)^{\frac{1}{2}}}$$

γ_1 Capture

Let us now consider the γ_1 capture process proceeding from the $P_{\frac{3}{2}}$, $F_{\frac{5}{2}}$, and $F_{\frac{7}{2}}$ partial waves to the $\frac{5^+}{2}$ ground state of F^{17}. If the scattering phase shifts for the two F partial waves are assumed to be equal and given by $-\phi_3$, then the initial wave function can be written in the extranuclear approximation as:

$$\Psi^\nu_{int} = \frac{2i\sqrt{\pi}\, e^{iw_1}}{kr} \left[\begin{array}{l} \sqrt{3}\; Y^o_1 \chi^\nu_{\frac{1}{2}} \left(F_1(kr) - (G_1(kr)+iF_1(kr)) e^{-i\phi_1} \sin\phi_1 \right) \\ \\ -\sqrt{7}\, e^{i(w_3 - w_1)} Y^o_3 \chi^\nu_{\frac{1}{2}} \left(F_3(kr) - (G_3(kr)+iF_3(kr)) e^{-i\phi_3} \sin\phi_3 \right) \end{array} \right]$$

It should be noted that the above expression contains a $P_{\frac{1}{2}}$ contribution which is incorrect since it does not include the effects of the $\frac{1^-}{2}$ resonance. The $P_{\frac{1}{2}}$ partial wave cannot contribute to the matrix element for E1 capture to the $\frac{5^+}{2}$ state; thus this incomplete $P_{\frac{1}{2}}$ segment cannot affect the final results. Including it in the initial wave function does, however, simplify the calculation.

The final wave function can be written in the extranuclear approximation as:

$$\Psi^{s}_{final} = g^{5^+}_{\frac{5}{2}b}(r) \sum_{M'\nu'} S^{\frac{5}{2}\ s}_{2M'\frac{1}{2}\nu'} Y_2^{M'} \chi^{\nu'}_{\frac{1}{2}}$$

Here $g^{5^+}_{\frac{5}{2}b}(r)$ is the bound Coulomb function for $\ell = 2$. Inserting these two wave functions into Eq. 2 and using the Wigner-Eckart theorem to perform the summation over the magnetic quantum numbers one obtains:

$$Q_1^m = -\frac{ie^{iw_1}\epsilon\sqrt{6}}{k} S^{\frac{5}{2}\ s}_{2(s-\nu)\frac{1}{2}\nu} \left[S^{10}_{2(s-\nu)1m} \left\{ N_1 - (D_1+iN_1)e^{-i\phi_1} \sin\phi_1 \right\} + \frac{3}{2} e^{i\beta} S^{30}_{2(s-\nu)1m} \left\{ N_3 - (D_3+iN_3)e^{-i\phi_3}\sin\phi_3 \right\} \right]$$

Where

$$\beta = w_3 - w_1$$

$$N_1 = \int_{r_o}^{\infty} g^{5^+}_{\frac{5}{2}b}(r)\ F_1(kr)r^2dr \qquad D_1 = \int_{r_o}^{\infty} g^{5^+}_{\frac{5}{2}b}(r)\ G_1(kr)r^2dr$$

$$N_3 = \int_{r_o}^{\infty} g^{5^+}_{\frac{5}{2}b}(r)\ F_3(kr)r^2dr \qquad D_3 = \int_{r_o}^{\infty} g^{5^+}_{\frac{5}{2}b}(r)\ G_3(kr)r^2dr$$

Since the terms in Q_1^m are of the form $S^{\frac{5}{2}\ s}_{2(s-\nu)1m}\ S^{J_o}_{2(s-\nu)1m}$ which is invariant under the substitution $m \to -m$, $\nu \to -\nu$, $s \to -s$, we need only consider the three transitions $\nu = \frac{1}{2}$ to $s = \frac{3}{2}$ (Q_1^{-1}), $\nu = \frac{1}{2}$ to $s = \frac{1}{2}$ (Q_1^{0}), and $\nu = \frac{1}{2}$

to $s = -\frac{1}{2}$ (Q_1^1). Then retaining only the first order terms in ϕ_1 and ϕ_3, one obtains after some algebra.

$$|Q_1^1|^2 = \frac{18\epsilon^2}{25k^2}\left[\begin{array}{l} N_1^2 + N_3^2 - 2\,N_1D_1\phi_1 - 2\,N_3D_3\phi_3 \\ \\ + 2\,N_1N_3(\cos\beta - \phi_1\sin\beta) - 2\cos\beta(N_1D_3\phi_3 + N_3D_1\phi_1) \end{array}\right]$$

$$|Q_1^0|^2 = \frac{36\epsilon^2}{25k^2}\left[\begin{array}{l} N_1^2 + \frac{9}{4}\,N_3^2 - 2\,N_1D_1\phi_1 - \frac{9}{2}\,N_3D_3\phi_3 \\ \\ - 3\,N_1N_3(\cos\beta - \phi_1\sin\beta) + 3\cos\beta\;\; N_1D_3\phi_3 + N_3D_1\phi_1 \end{array}\right]$$

$$|Q_1^{-1}|^2 = 2|Q_1^1|^2$$

But averaging over the initial spins and summing over the final spins, the differential cross section is given by.

$$\frac{d\sigma}{d\Omega} = \frac{16\pi}{9}\left(\frac{E_\gamma}{\hbar c}\right)^3 \frac{1}{\hbar v}\left[|Q_1^1|^2Z_{11} + |Q_1^0|^2Z_{10} + |Q_{1-1}|^2Z_{1-1}\right]$$

Inserting the expressions given above for the $|Q_1^m|^2$'s into this formula and making use of the fact that $Z_{1-1} = Z_{11}$ together with the expressions previously given for Z_{11} and Z_{10}, one obtains.

$$\frac{d\sigma}{d\Omega} = \frac{18}{25} K \frac{E_\gamma^3}{E_p^3} \left[N_1^2 + N_3^2 - 2N_1D_1\phi_1 - 2N_3D_3\phi_3 + 2 N_1N_3(\cos\beta - \phi_1\sin\beta) - 2\cos\beta \; N_1D_3\phi_3 + N_3D_1\phi_1 + \sin^2\theta \left[\frac{N_1^2}{6} + N_3^2 - \frac{N_1D_1\phi_1}{3} - 2N_3D_3\phi_3 - 3N_1N_3(\cos\beta - \phi_1\sin\beta) + 3\cos\beta \; N_1D_3\phi_3 + N_3D_1\phi_1 \right] \right]$$

Integrating this differential cross section over 4π, yields the following expression for the total cross section.

$$\sigma = \frac{24}{5} \pi K \frac{E_\gamma^3}{E_p^3} \left[\frac{2}{3} \left[N_1^2 - 2N_1D_1\phi_1 \right] + N_3^2 - 2N_3D_3\phi_3 \right]$$

Here again

$$K = \frac{1}{\sqrt{2}} \frac{e^2}{\hbar c} \frac{1}{(m_p c^2)^{\frac{1}{2}}} \frac{1}{\hbar c} \left(1 - \frac{8 m_p}{m_o 16} \right)^2$$

Matrix Element Computation

Before the capture matrix elements M_1, M_2, N_1, D_1, N_3, D_3, and the hard sphere phase shifts and penetration factors could be calculated, it was necessary to compute the four free Coulomb functions F_1, G_1, F_3, G_3, and the two bound Coulomb functions $g_b^{\frac{1}{2}+}(r)$ and $g_b^{\frac{5}{2}+}(r)$. While tables of F_ℓ and G_ℓ exist, they do not extend to sufficiently large radii to be useful for the computation of the matrix elements, and tables of the bound Coulomb functions apparently do not exist. This it was necessary to compute these functions.

The computation was carried out by transforming the differential equation which these functions satisfy into a finite difference equation. This difference equation was then used to continue the functions through the required radius range once the proper initial values were determined. The initial values for the F_ℓ functions were determined from a power series representation valid for small radii; the power series used was that given by Hull and Breit, page 411 (1959). The initial values of the G_ℓ's and the bound state functions were determined from JWKB expressions which are valid for large values of the radius. The JWKB expressions used for this purpose were those given by Tombrello and Phillips, page 226 (1961).

Difference intervals of .1 fermi were used, and the functions were computed from 3 to 100 fermis. The F_ℓ and G_ℓ functions computed in this manner were checked against the tables of Bloch (1951), and the bound state functions were checked against values computed from the integral representation of these functions (see for example page 349 of the article by Lane and Thomas, 1958). In all cases the functions were found to be accurate to within 1%. The matrix elements were computed from the calculated functions by numerical integration using the trapezoidal rule and .1 fermi intervals. The error in these matrix elements is estimated to be less than 2%.

REFERENCES

Blatt and Weisskopf, 1952, Theoretical Nuclear Physics (John Wiley and Sons, New York).

I. Bloch, M. H. Hull, Jr., A. A. Broyles, W. G. Bouricius, B. E. Freeman, and G. Breit, 1951, Revs. Modern Phys. 23, 147.

R. Christy and I. Duck, 1961, Nuclear Phys. 24, 89.

G. Emery and R. Kane, 1960, Phys. Rev. 118, 755.

Gladys White Grodstein, 1957, X-ray Attenuation Coefficients From 10 keV to 100 MeV (National Bureau of Standards Circular 583, Washington, D.C.).

R. L. Heath, 1957, Scintillation Spectrometry Gamma-Ray Spectrum Catalogue (Phillips Petroleum Co., Idaho Falls).

M. H. Hull, Jr. and G. Breit, 1959 "Coulomb Wave Functions" Handbuch der Physik (Springer-Verlag, Berlin) Vol XLI/1.

J. V. Kane, R. E. Pixley, R. B. Schwartz, and A. Schwarzschild, 1960, Phys. Rev. 120, 162.

M. Lal, 1961, Ph.D. Thesis, University of British Columbia.

A. M. Lane and R. G. Thomas, 1958, Revs. Modern Phys. 30, 257.

A. M. Lane, 1960, Revs. Modern Phys. 32, 520.

R. A. Laubenstein, M. J. W. Laubenstein, L. J. Koester, and R. C. Mobley, 1951, Phys. Rev. 84, 12.

T. Lauritsen and F. Ajzenberg-Selove, 1962, Nuclear Data Sheets Sets 5 and 6, 1961 (National Academy of Sciences - National Research Council, Washington, D.C.).

M. H. Macfarlane and J. B. French, 1960, Revs. Modern Phys. 32, 567.

S. R. Salisbury and H. T. Richards, 1962, Phys. Rev. 126, 2143.

N. Tanner, 1959, Phys. Rev. 114, 1060.

T. A. Tombrello and G. C. Phillips, 1961, Phys. Rev. 122, 224.

W. Whaling, 1958, "The Energy Loss of Charged Particles in Matter" Handbuch der Physik (Springer-Verlag, Berlin) Vol XXIV.

W. Whaling, 1962, Private Communication.

D. H. Wilkinson, 1960, "Analysis of Gamma Decay Data" Nuclear Spectroscopy Part B (Academic Press, New York), 853.

Table I. The number of photopeak counts determined from an analysis of the raw capture spectrum obtained at the stated bombarding energy; these bombarding energies refer to the laboratory coordinate system. The yields quoted here have been corrected for only the crystal, tungsten blank, and $O^{18}(p,n)$ backgrounds. The error attached to the individual data points is just that due to counting statistics and the probable error in the background subtraction. The error listed at the bottom of the table is common to all the data points and indicates the amount by which all the yields could simultaneously be increased or decreased. See text p. 24.

TABLE I

Raw Photopeak Yields

E_p (Lab) in MeV	γ_1 Counts	γ_2 Counts
2.574	951 ± 48	4536 ± 79
2.578	999 ± 46	4601 ± 78
2.593	927 ± 49	4620 ± 81
2.606	1077 ± 51	4754 ± 81
2.612	1017 ± 53	4722 ± 82
2.626	1061 ± 53	4856 ± 83
2.632	1097 ± 54	4874 ± 84
2.635	1094 ± 54	4920 ± 84
2.641	1002 ± 56	5055 ± 86
2.645	996 ± 61	5045 ± 91
2.651	1033 ± 78	5116 ± 104
2.655	1043 ± 82	5123 ± 107
2.661	1051 ± 68	4872 ± 95
2.665	977 ± 60	4134 ± 84
2.671	1011 ± 55	3362 ± 76
2.675	931 ± 53	3201 ± 74
2.681	952 ± 55	3346 ± 75
2.685	993 ± 53	3453 ± 75
2.691	972 ± 54	3620 ± 77
2.695	1086 ± 55	3805 ± 78
2.701	999 ± 55	3960 ± 79
2.715	1006 ± 55	4076 ± 80
2.721	970 ± 56	4140 ± 81
2.742	998 ± 57	4430 ± 84
2.746	1049 ± 57	4263 ± 82
2.763	976 ± 60	4378 ± 86
Common Error	± 40	± 70

Table II. The photopeak yields of Table I corrected for the γ_2—γ_3 summing into the photopeak of γ_1, the counts contributed by the Compton distribution and the first escape peak of γ_1 to the photopeak region of γ_2, and the variation of the photopeak detection efficiency of the counter with the energy of the gamma ray. Again in this case, the error attached to the individual data points is just that due to counting statistics and the probable error in the background subtraction. The error listed at the bottom of the table is common to all the data points and indicates the amount by which all the yields could simultaneously be increased or decreased. See text p. 26.

TABLE II

Corrected Photopeak Yields

E_p (Lab) in MeV	γ_1 Counts	γ_2 Counts
2.574	783 ± 49	3665 ± 77
2.578	838 ± 48	2744 ± 76
2.593	762 ± 50	3762 ± 79
2.606	908 ± 52	3920 ± 79
2.612	852 ± 53	3882 ± 81
2.626	895 ± 53	4042 ± 82
2.632	933 ± 54	4055 ± 83
2.635	928 ± 55	4129 ± 83
2.641	834 ± 57	4254 ± 85
2.645	831 ± 62	4259 ± 90
2.651	866 ± 80	4319 ± 104
2.655	877 ± 83	4342 ± 107
2.661	897 ± 69	4076 ± 95
2.665	853 ± 61	3351 ± 84
2.671	918 ± 56	2558 ± 76
2.675	844 ± 53	2412 ± 74
2.681	863 ± 55	2546 ± 76
2.685	901 ± 54	2669 ± 76
2.691	876 ± 56	2826 ± 78
2.695	986 ± 57	3032 ± 79
2.701	892 ± 57	3180 ± 80
2.715	901 ± 57	3335 ± 82
2.721	864 ± 57	3374 ± 83
2.742	887 ± 60	3687 ± 87
2.746	950 ± 60	3532 ± 85
2.763	873 ± 63	3646 ± 89
Common Error	± 50	± 80

Figure 1. The energy level diagram of F^{17} as taken from the compilation of Lauritsen and Ajzenberg-Selove (1962). The capture gamma ray to the $\frac{5}{2}^+$ ground state will be denoted by γ_1; the capture gamma ray to the $\frac{1}{2}^+$ .500-MeV state will be denoted by γ_2, and the cascade gamma ray from the $\frac{1}{2}^+$ state to the $\frac{5}{2}^+$ state will be denoted by γ_3.

FIGURE 1

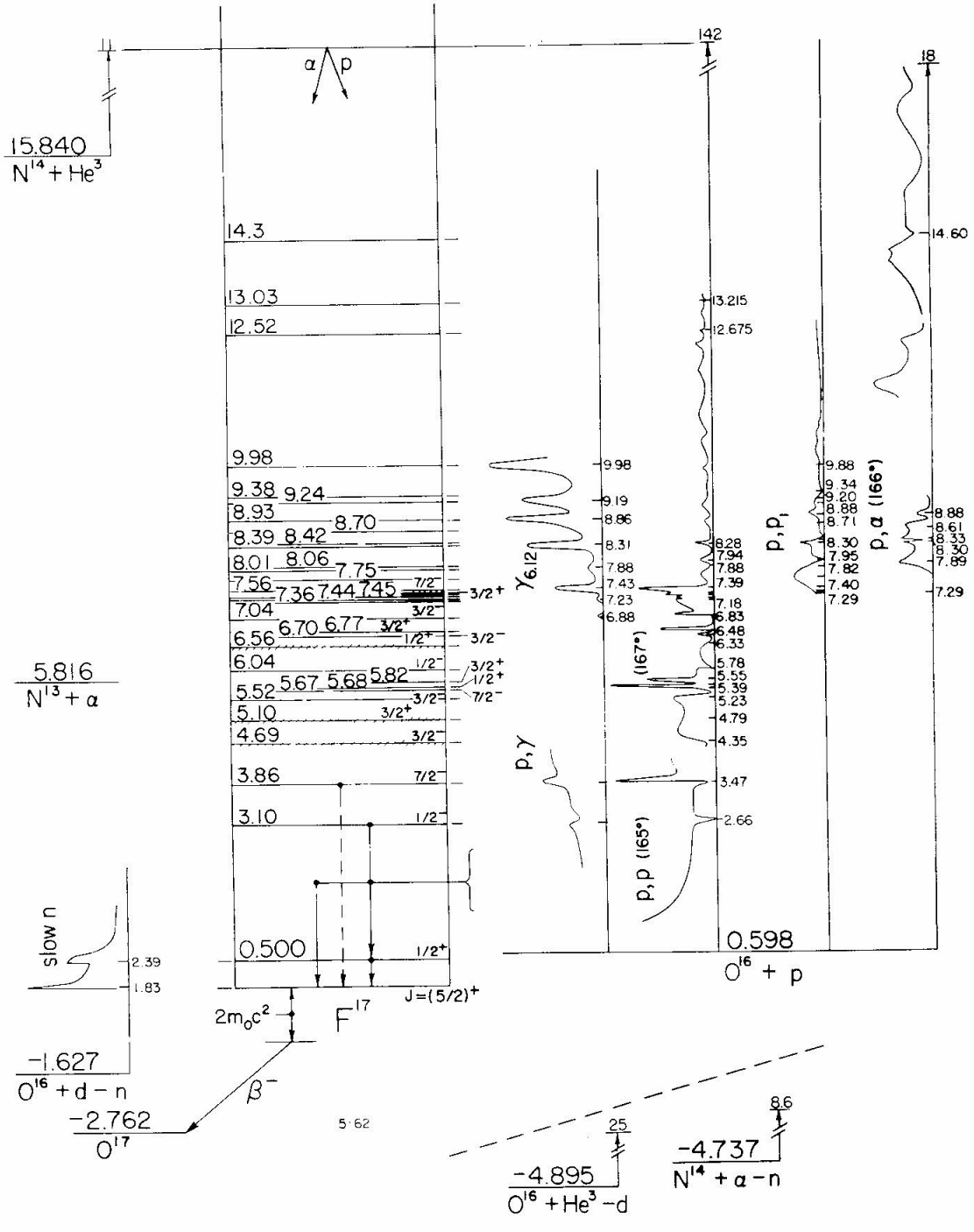
15.840
N14 + He3
α
p
14.3
13.03
12.52
9.98
9.38
9.24
8.93
8.70
8.39
8.42
8.01
8.06
7.75
7.56
7.36
7.44
7.45
7/2-
3/2+
7.04
3/2-
6.56
6.70
6.77
3/2+
1/2+
3/2-
6.04
1/2-
3/2+
1/2+
5.52
5.67
5.68
5.82
3/2-
7/2-
5.10
3/2+
4.69
3/2-
3.86
7/2-
3.10
1/2-
0.500
1/2+
J=(5/2)+
2m0c2
F17
β-
5.816
N13 + α
slow n
2.39
1.83
-1.627
O16 + d - n
-2.762
O17
5·62
142
13.215
12.675
γ6.12
9.98
9.19
8.86
8.31
7.88
7.43
7.23
6.88
(167°)
p, γ
p, p (165°)
3.47
2.66
0.598
O16 + p
p, p1
9.88
9.34
9.20
8.88
8.71
8.30
7.95
7.82
7.40
7.29
18
14.60
p, α (166°)
8.88
8.61
8.33
8.30
7.89
7.29
25
-4.895
O16 + He3 - d
8.6
-4.737
N14 + α - n

Figure 2. A section of the target chamber and counter assembly taken in the plane defined by the beam axis and the central axis of the counter. The target assembly is shown in the orientation used to obtain the capture data; the normal to the target blank is at an angle of 40° with respect to the beam axis. See text p. 5.

FIGURE 2

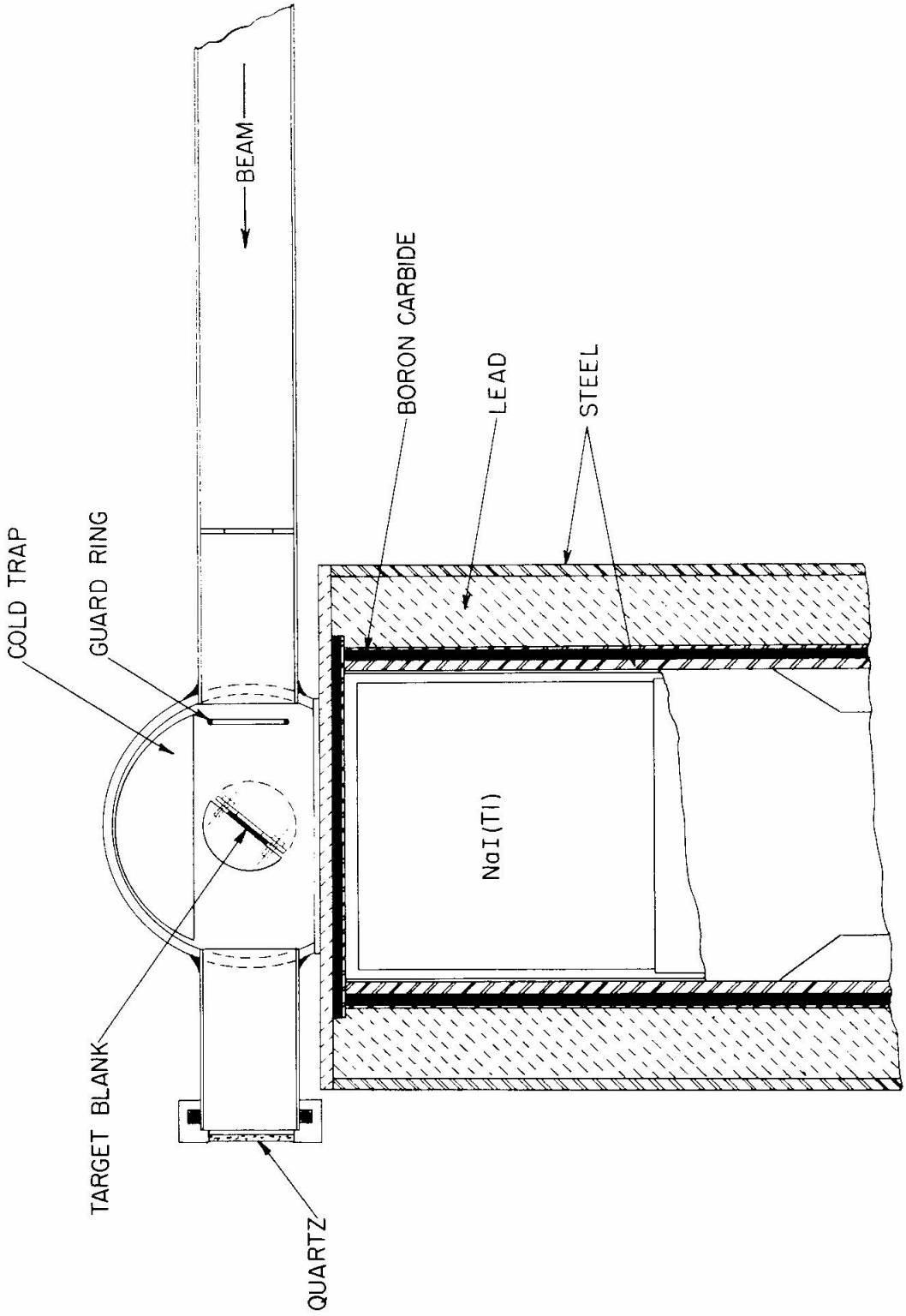
BEAM
BORON CARBIDE
LEAD
STEEL
COLD TRAP
GUARD RING
NaI(Tl)
TARGET BLANK
QUARTZ

Figure 3. A section of the target chamber and counter assembly taken in the plane defined by the vertical axis of the target chamber and the central axis of the counter. For clarity the target assembly is shown rotated so that the normal to the target is along the beam direction and is shown in a face view rather than in section. See text p. 5.

FIGURE 3

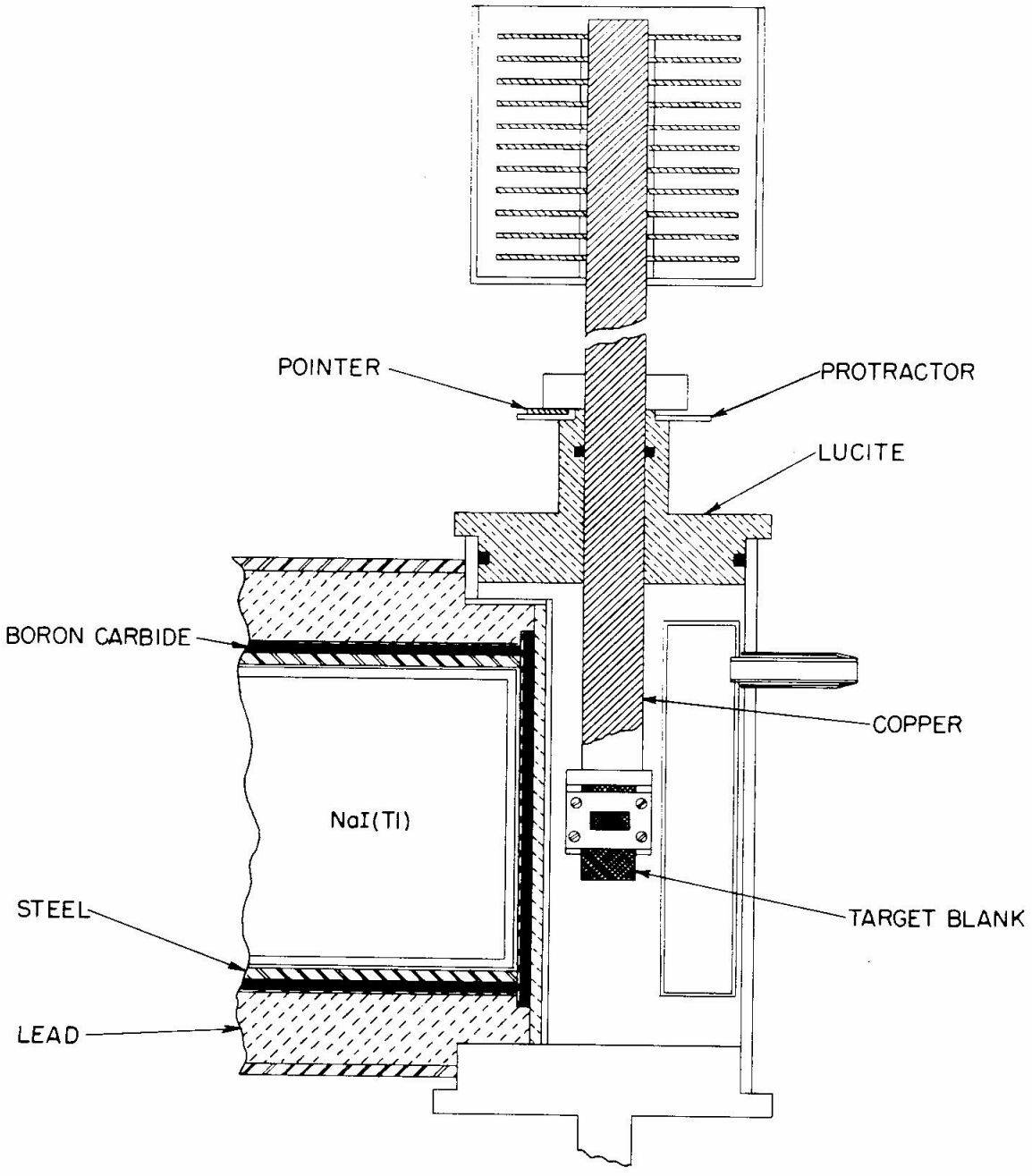
POINTER
PROTRACTOR
LUCITE
BORON CARBIDE
COPPER
NaI(Tl)
STEEL
TARGET BLANK
LEAD

Figure 4. A typical pulse height spectrum obtained with a tungsten oxide target approximately 9 keV thick for 2.66 MeV protons. This spectrum was obtained for a proton bombarding energy of 2.632 MeV and a total bombarding charge of 3.78 mCoul. In addition to the two $O^{16}(p,\gamma)$ capture gamma rays, γ_1 and γ_2, the .871-MeV gamma ray from the $O^{17}(p,p')$ reaction and the 1.98-MeV gamma ray from the $O^{18}(p,p')$ reaction are quite prominent. The scale has been reduced by a factor of 10 in the region of the latter two gamma rays. See text pp. 20, 22.

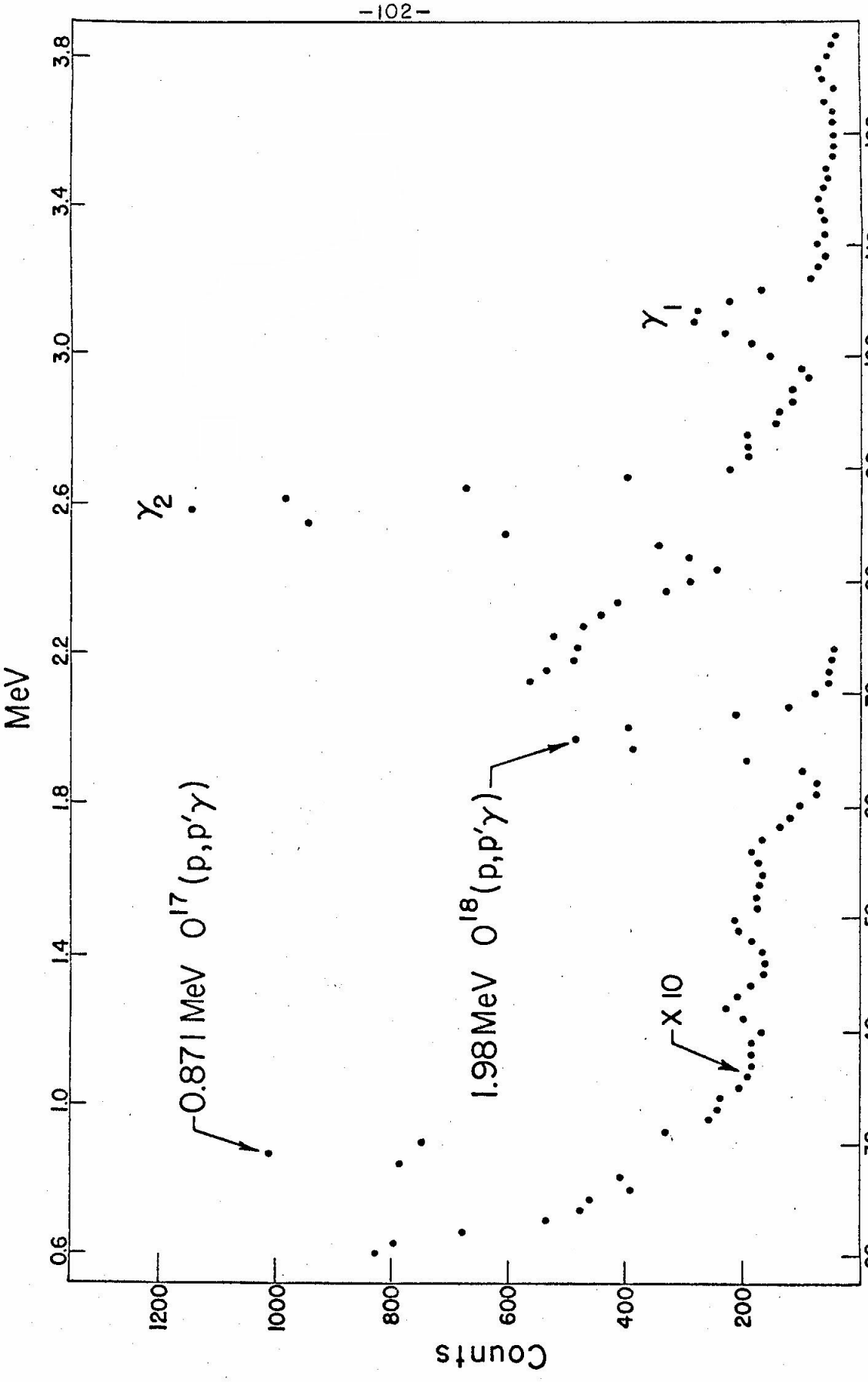
MeV
0.6
1.0
1.4
1.8
2.2
2.6
3.0
3.4
3.8
Channel
20
30
40
50
60
70
80
90
100
110
120
Counts
200
400
600
800
1000
1200
γ_2
γ_1
0.871 MeV $O^{17}(p,p'\gamma)$
1.98 MeV $O^{18}(p,p'\gamma)$
X 10

FIGURE 4

Figure 5. The gamma-ray spectrum resulting from proton bombardment of a bare tungsten blank taken from the same stock as that used to produce the oxide targets. The data points represent 5-channel sums located at the center of the 5-channel interval over which the sum was taken. The solid curve was used for subtracting the tungsten blank background from the capture spectra. See text pp. 20, 21.

Figure 6. The gamma-ray spectrum resulting from the capture by the NaI(Tl) scintillator of the neutrons produced by the $O^{18}(p,n)$ reaction. This spectrum was obtained with a very thin tungsten oxide target made from oxygen gas highly enriched in O^{18}. The yield from the $O^{18}(p,n)$ reaction was so large that the background due to the tungsten blank is completely negligible. As in Fig. 5 the data points represent 5-channel sums located at the center of the 5-channel interval over which the sum was taken. The solid curve was used to subtract the $O^{18}(p,n)$ background from the capture spectra. See text pp. 10, 20, 21.

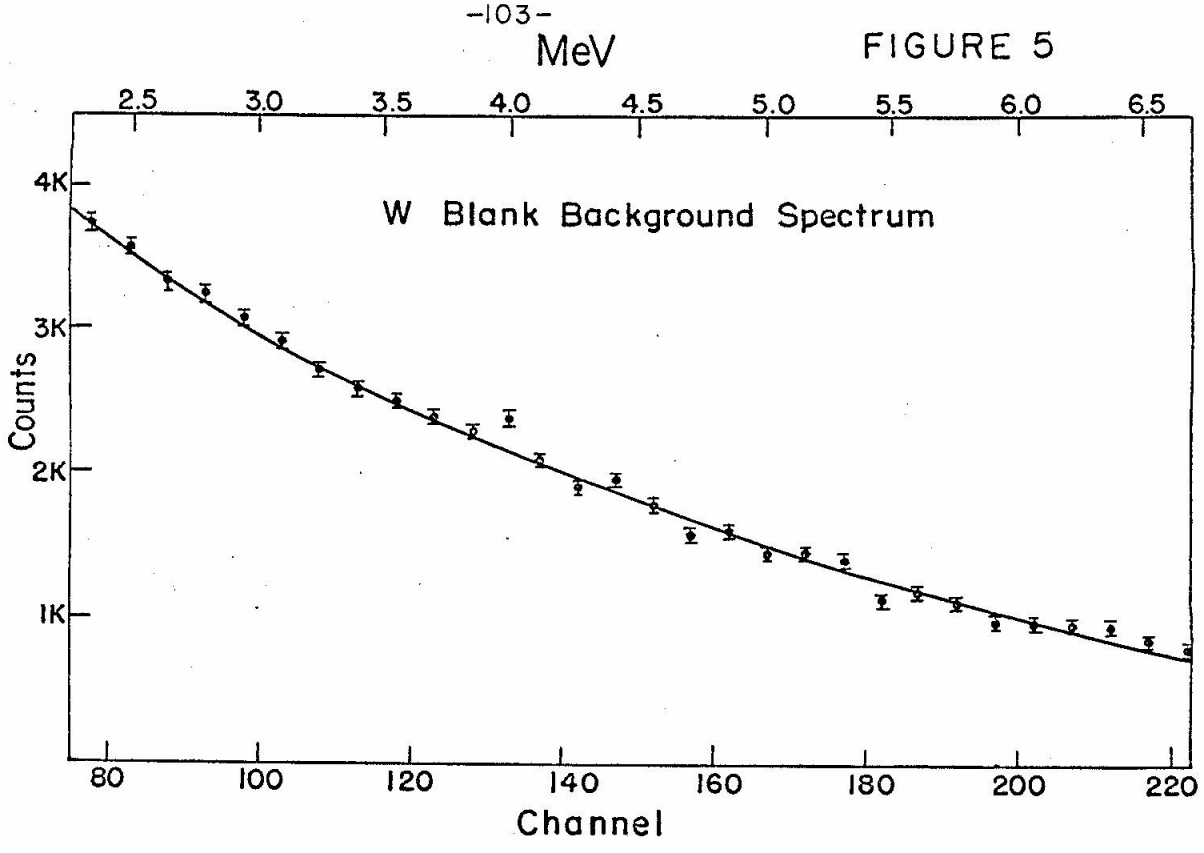

FIGURE 5

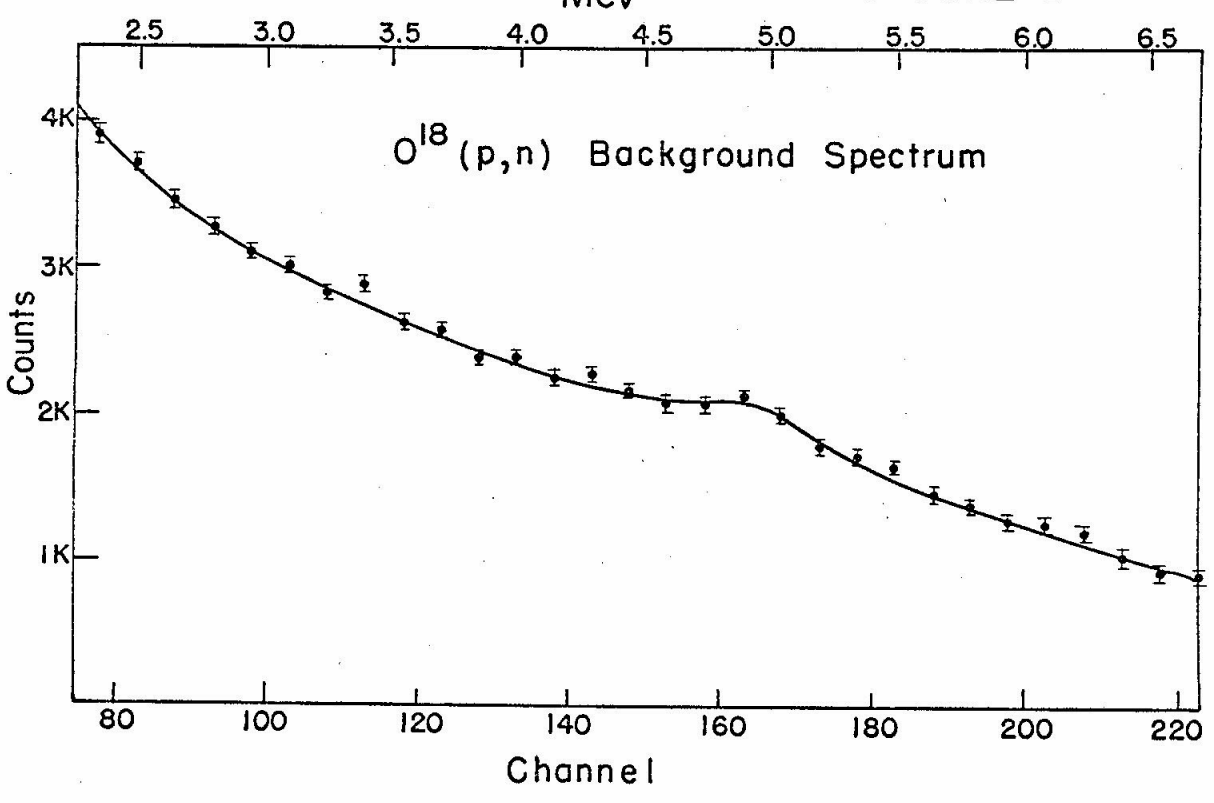

FIGURE 6

Figure 7. The γ_1 and γ_2 photopeak region of the spectrum shown in Fig. 4 after subtraction of the tungsten blank, $O^{18}(p,n)$ and crystal backgrounds. More of the high energy background has been shown than in Fig. 4, and a displaced 0 ordinate has been used in order to illustrate the subtraction results. The graphical determination of the center of the γ_2 photopeak distribution is shown by the dotted lines. The regions over which the photopeak counts were summed to obtain the raw photopeak yields are indicated by the solid lines. See text p. 22.

FIGURE 7

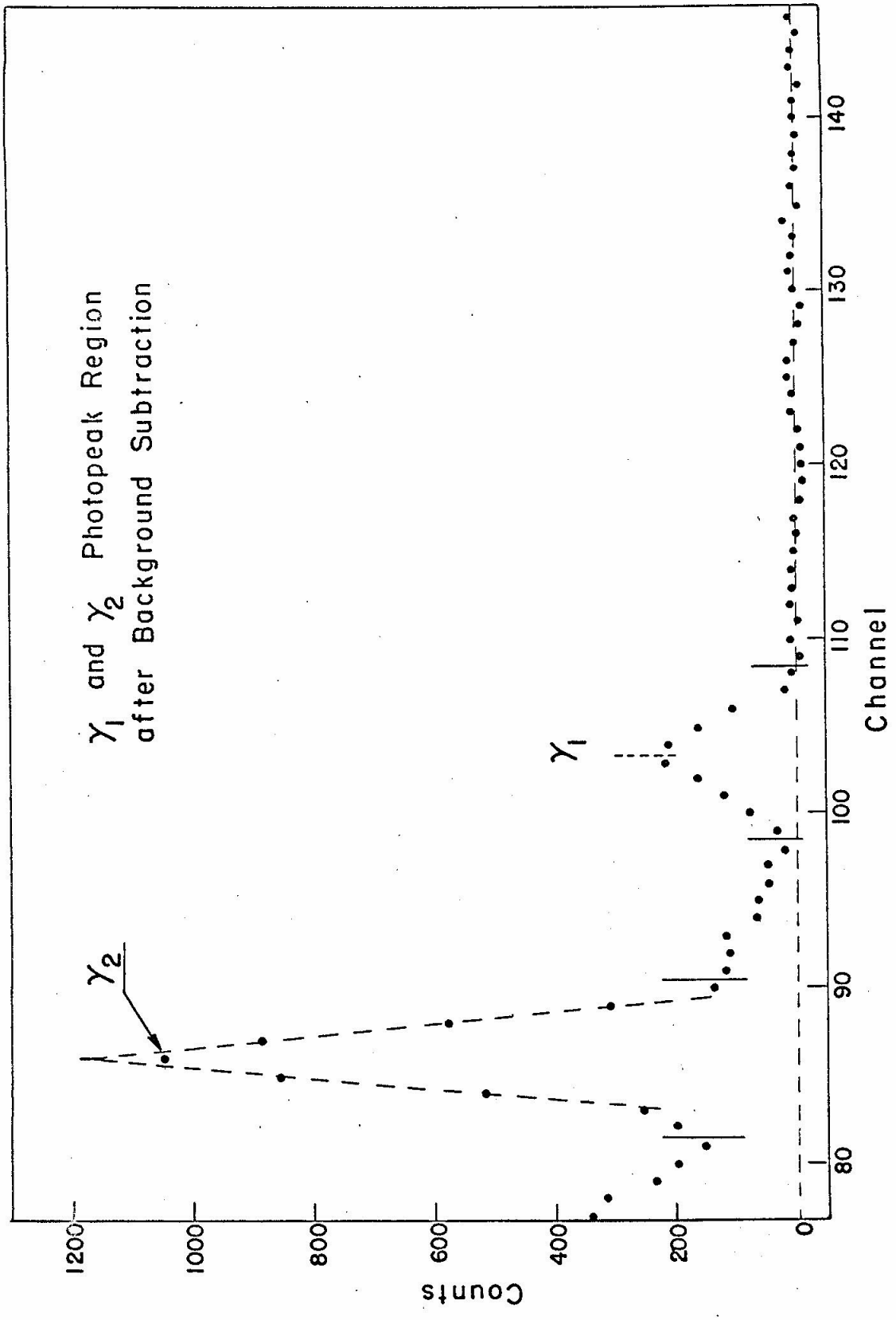
γ_1 and γ_2 Photopeak Region
after Background Subtraction
γ_2
γ_1
Counts
Channel
0
200
400
600
800
1000
1200
80
90
100
110
120
130
140

Figure 8. The corrected γ_2 photopeak yield as a function of the bombarding energy. The raw photopeak yield has been corrected for the counts due to the Compton distribution and first escape peak of γ_1 and for the energy dependence of the photopeak detection efficiency. The error indicated is just the statistical error plus the estimated error in the background subtraction. The error common to all the data points is given by the single error bar below the excitation curve; it indicates the range over which the empirical excitation curve could be shifted vertically. The solid curve is the excitation curve calculated from the extranuclear model for the parameters r_o = 5.1 f, φ_1 = .05 rad, $\theta^2_{\frac{1}{2}}$+sp = .57. See text pp. 4, 26, 46.

FIGURE 8

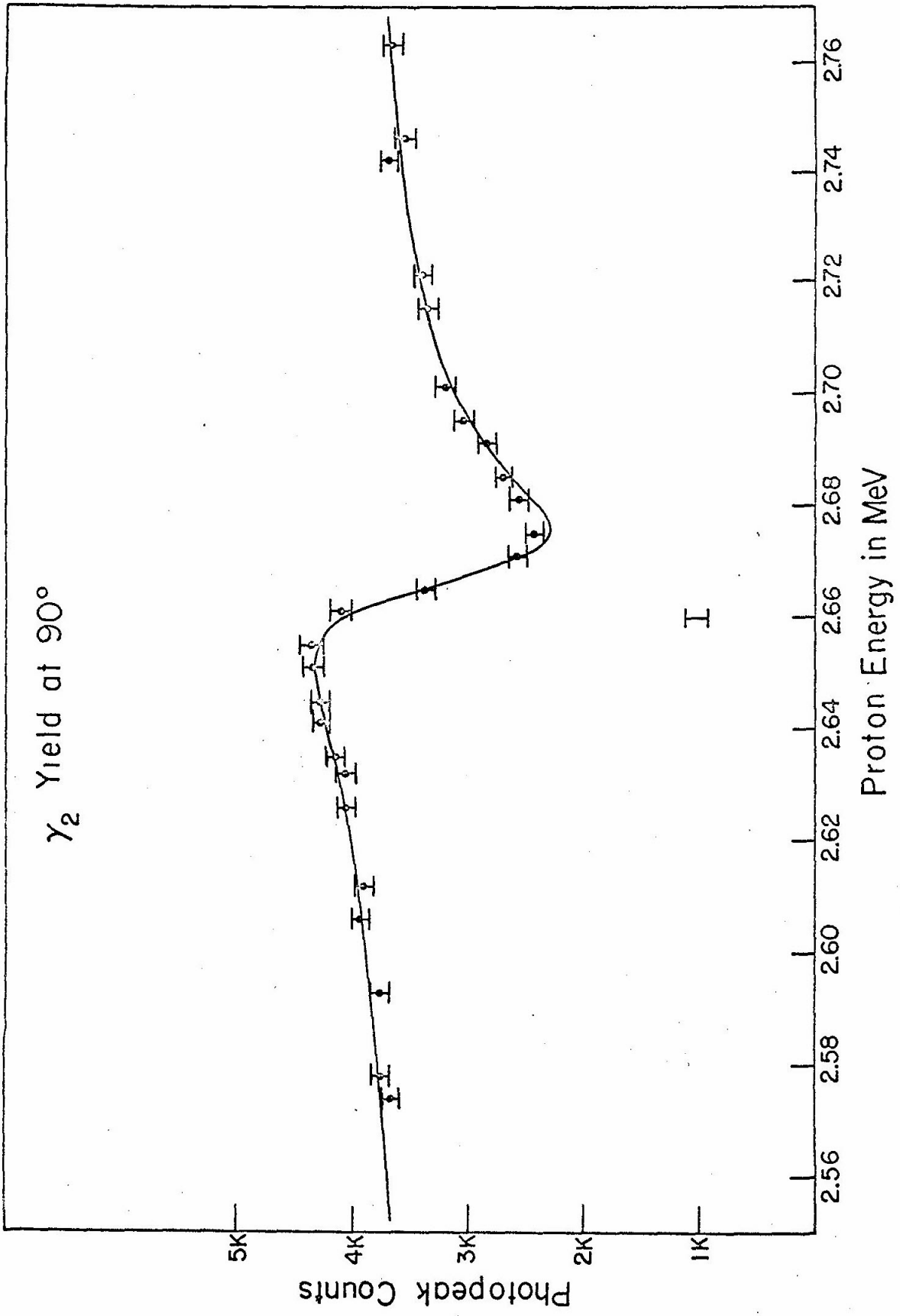
γ_2 Yield at 90°
I
Photopeak Counts
5K
4K
3K
2K
1K
2.56
2.58
2.60
2.62
2.64
2.66
2.68
2.70
2.72
2.74
2.76
Proton Energy in MeV

Figure 9. The corrected γ_1 photopeak yield as a function of the bombarding energy. The raw photopeak yield has been corrected for the effects of γ_2--γ_3 summing and the energy dependence of the photopeak detection efficiency. The error indicated is just the statistical error plus the estimated error in the background subtraction. The error common to all the data points is given by the single error bar below the excitation curve; it indicates the range over which the excitation curve could be shifted vertically. The solid curve is the excitation curve calculated from the extranuclear model for the parameters r_o = 5.1 f, φ_1 = .05 rad, $\theta^2_{\frac{5^+}{2}}$sp = .38. See text pp. 4, 26, 48.

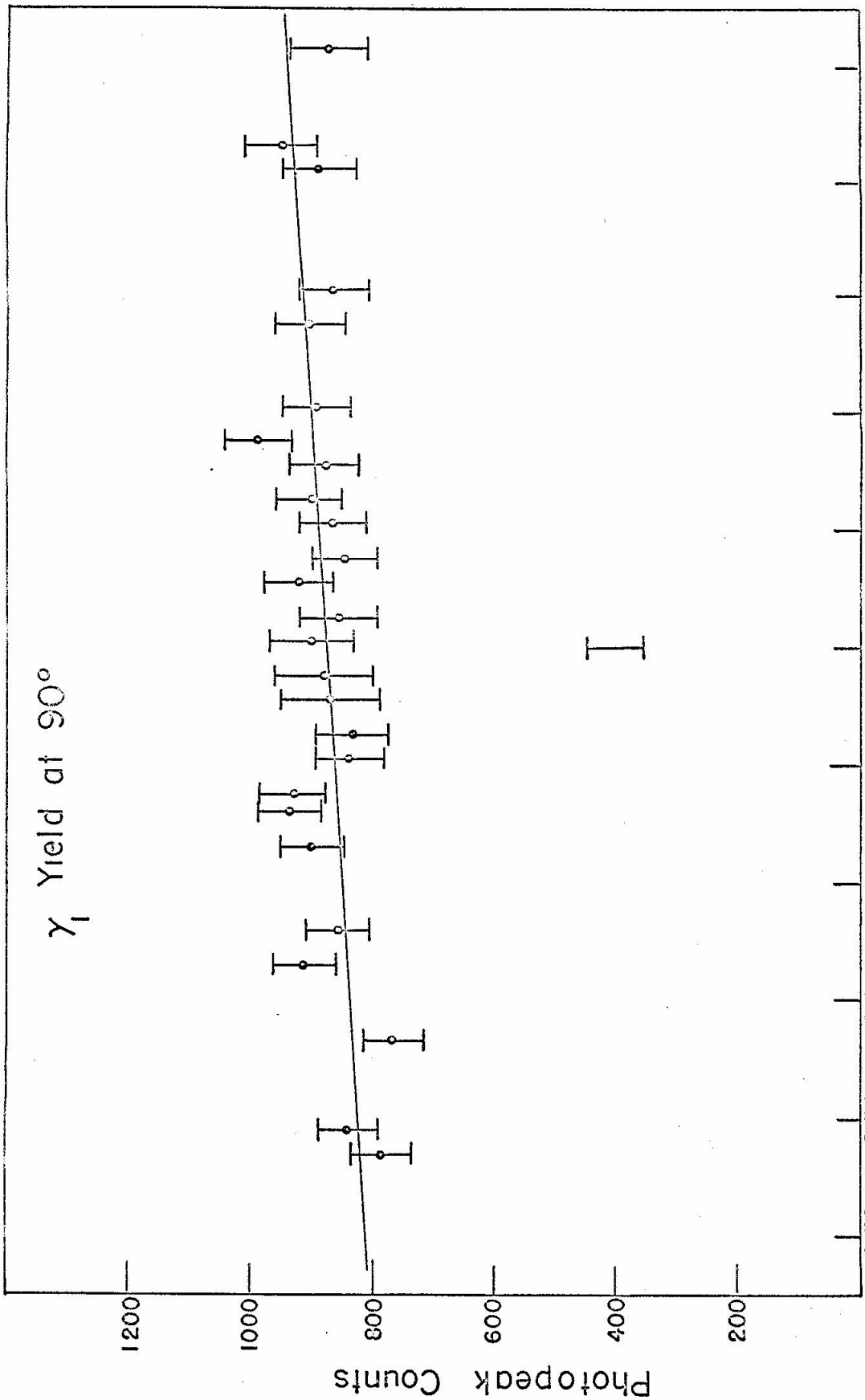
γ_1 Yield at 90°
Photopeak Counts
1200
1000
800
600
400
200
2.56
2.58
2.60
2.62
2.64
2.66
2.68
2.70
2.72
2.74
2.76
Proton Energy in MeV

FIGURE 9

Figure 10. The region of best agreement between the experimental γ_2 excitation curve and the curve calculated for the case in which the internal transition parameter ξ is taken to be zero. The region of best agreement is given in terms of the common $P_{\frac{1}{2}}$, $P_{\frac{3}{2}}$ potential phase shift $-\varphi_1$ and the ratio $R = \frac{M_2}{M_1}$ of the two capture integrals evaluated at the mean bombarding energy of 2.66 MeV. The upper curve gives the value of R^o for a given choice of cut off radius r_o for the capture integrals. The region illustrated is that over which the least squares sum was essentially constant; at the dashed boundary this sum had increased by approximately 1.0 from its minimum value. Outside the dashed boundary the least squares sum increased quite rapidly.

The region shown in this figure is meant only to be illustrative of the nonuniqueness of the least squares fit to the experimental data even when the parameter ξ had arbitrarily been taken to be zero. It should not be interpreted as defining the only set of parameters R^o and φ_1 for which good agreement with the experimental data could be obtained. For ξ different from zero, the region of best agreement would have a different location and shape. See text pp. 45, 49.

FIGURE 10

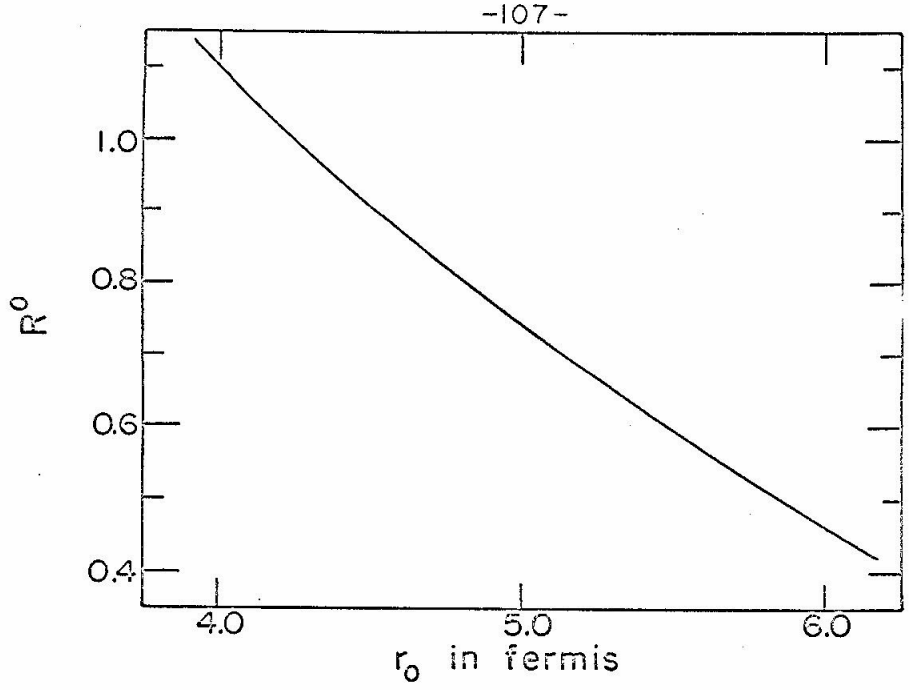
1.0
0.8
0.6
0.4
R^o
4.0
5.0
6.0
r_o in fermis

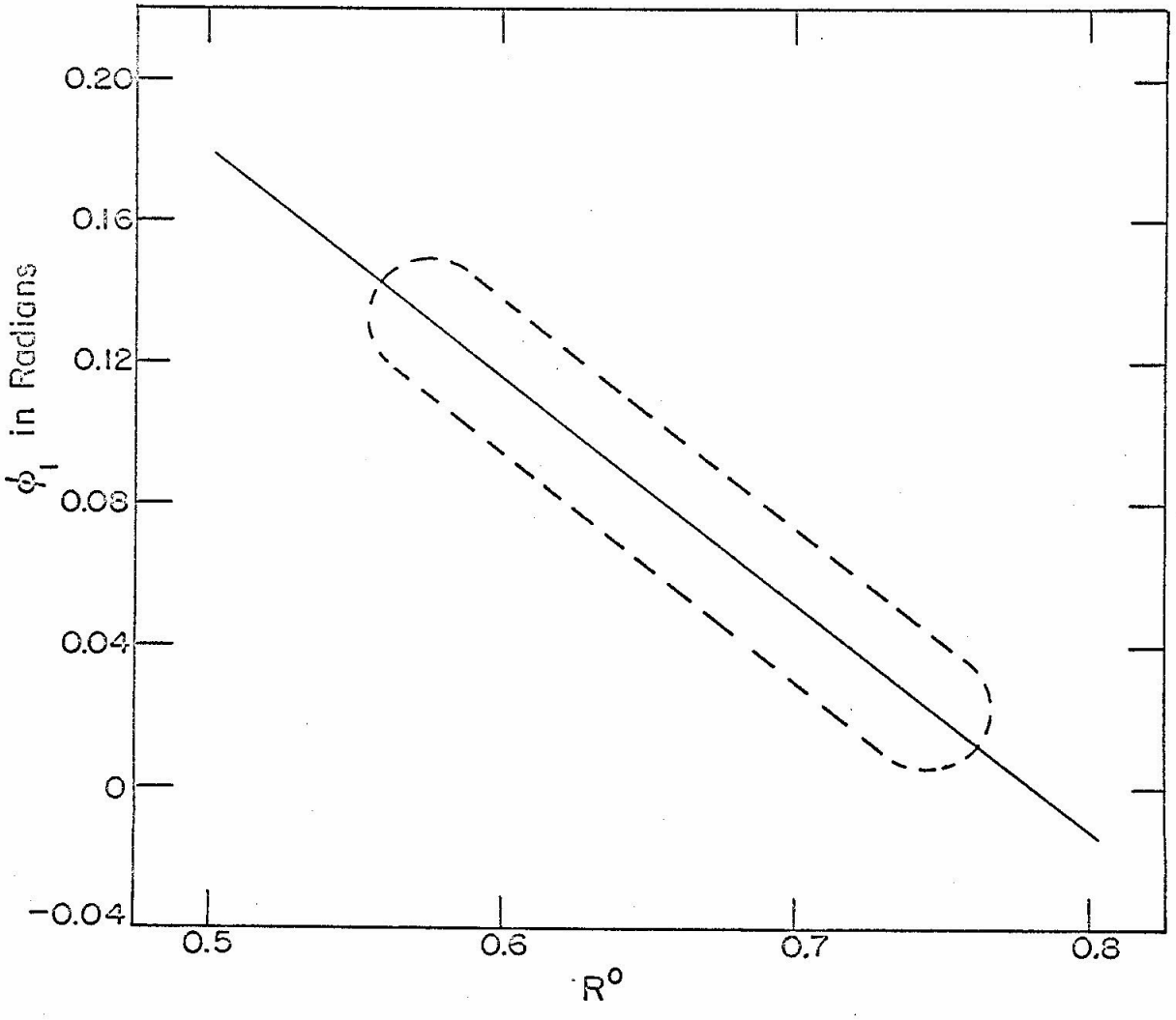
0.20
0.16
0.12
0.08
0.04
0
-0.04
ϕ_1 in Radians
0.5
0.6
0.7
0.8
R^o

Figure 11. $O^{16}(p,\gamma)$ capture cross sections computed on the basis of the extranuclear model; the free parameters used in calculating these cross sections were taken to be those giving the best fit to the empirical excitation curves. The parameters used were $r_o = 5.1$ f, $\varphi_1 = .05$ rad, $\theta^2_{\frac{1}{2}^+ sp} = .57$, and $\theta^2_{\frac{5}{2}^+ sp} = .38$. The error in these computed cross sections due to the common error in the two empirical reduced widths resulting from the uncertainty in the photopeak detection efficiency and the oxygen content of the target has not been indicated. This common error would simply change the vertical scale, but would not alter the shape of the curves; in terms of this common multiplicative factor, the uncertainty is estimated to be $(1 \pm .18)$. The error indicated on the γ_1 curve and the total cross section curve indicates the range through which these curves could be shifted vertically. This error is due to the additional uncertainty in the γ_1 photopeak detection efficiency relative to the ThC" calibration. See text pp. 49, 50, 51.

FIGURE 11

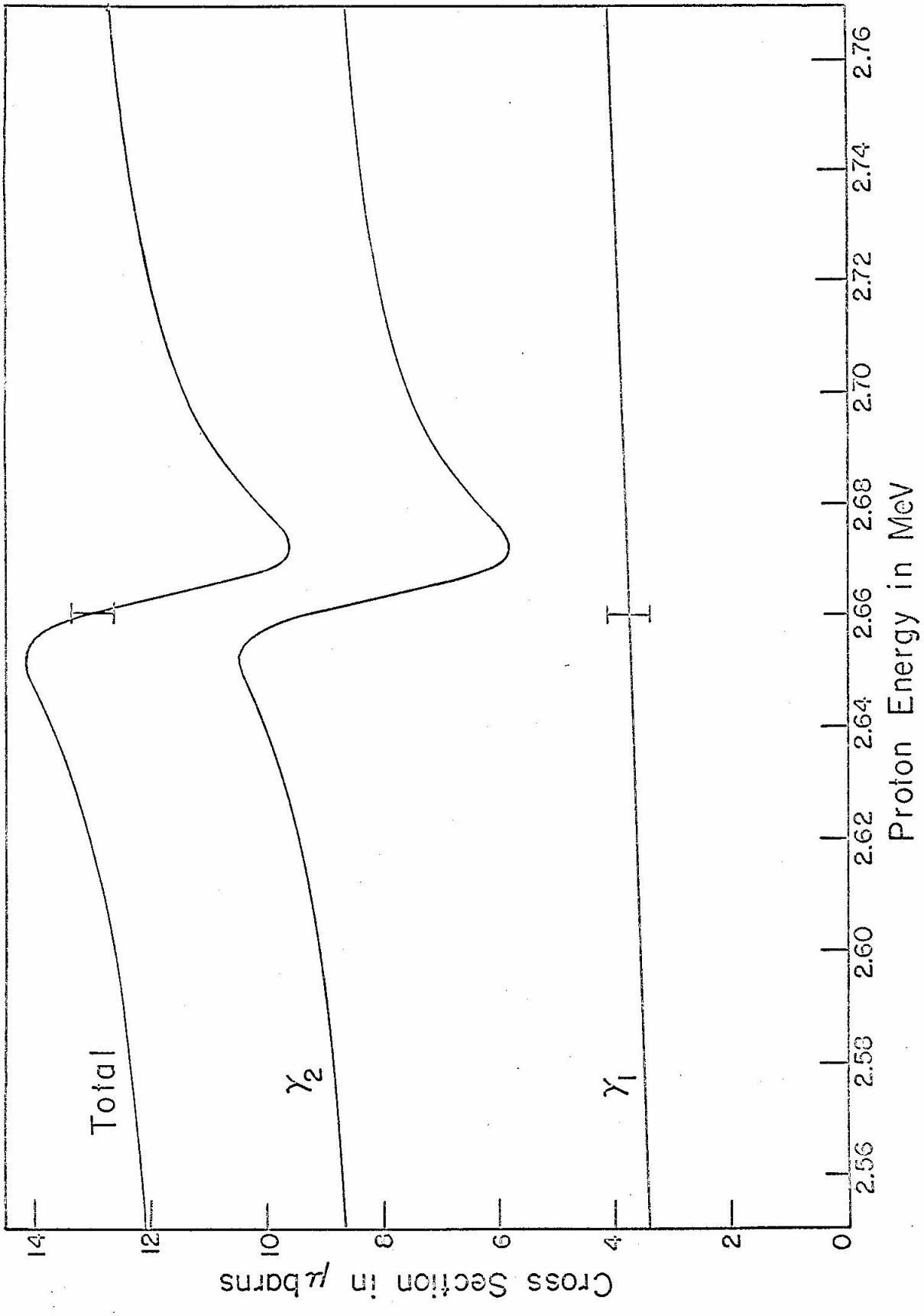
Total
γ_2
γ_1
Cross Section in μbarns
0
2
4
6
8
10
12
14
2.56
2.58
2.60
2.62
2.64
2.66
2.68
2.70
2.72
2.74
2.76
Proton Energy in MeV

Figure 12. The scattering profile for the tungsten oxide target used to obtain the capture data presented in this thesis. This profile was obtained by measuring the number of scattered protons passed by the magnetic spectrometer, for a fixed bombarding charge, as a function of the bombarding energy. The acceptance energy of the magnetic spectrometer was held constant at 2.66 MeV, and the spectrometer was positioned so that it accepted protons scattered from the target at an angle of 40° with respect to the target normal. The incident beam also made an angle of 40° with respect to the target normal. The horizontal scale gives the difference between the bombarding energy and the fixed setting of the magnetic spectrometer; the vertical scale indicates the number of protons detected at the exit of the spectrometer for a fixed bombarding charge. The curve drawn through the data points represents the superposition of two error functions; this curve was used in the analysis of the scattering profile. See text pp. 61, 62, 66.

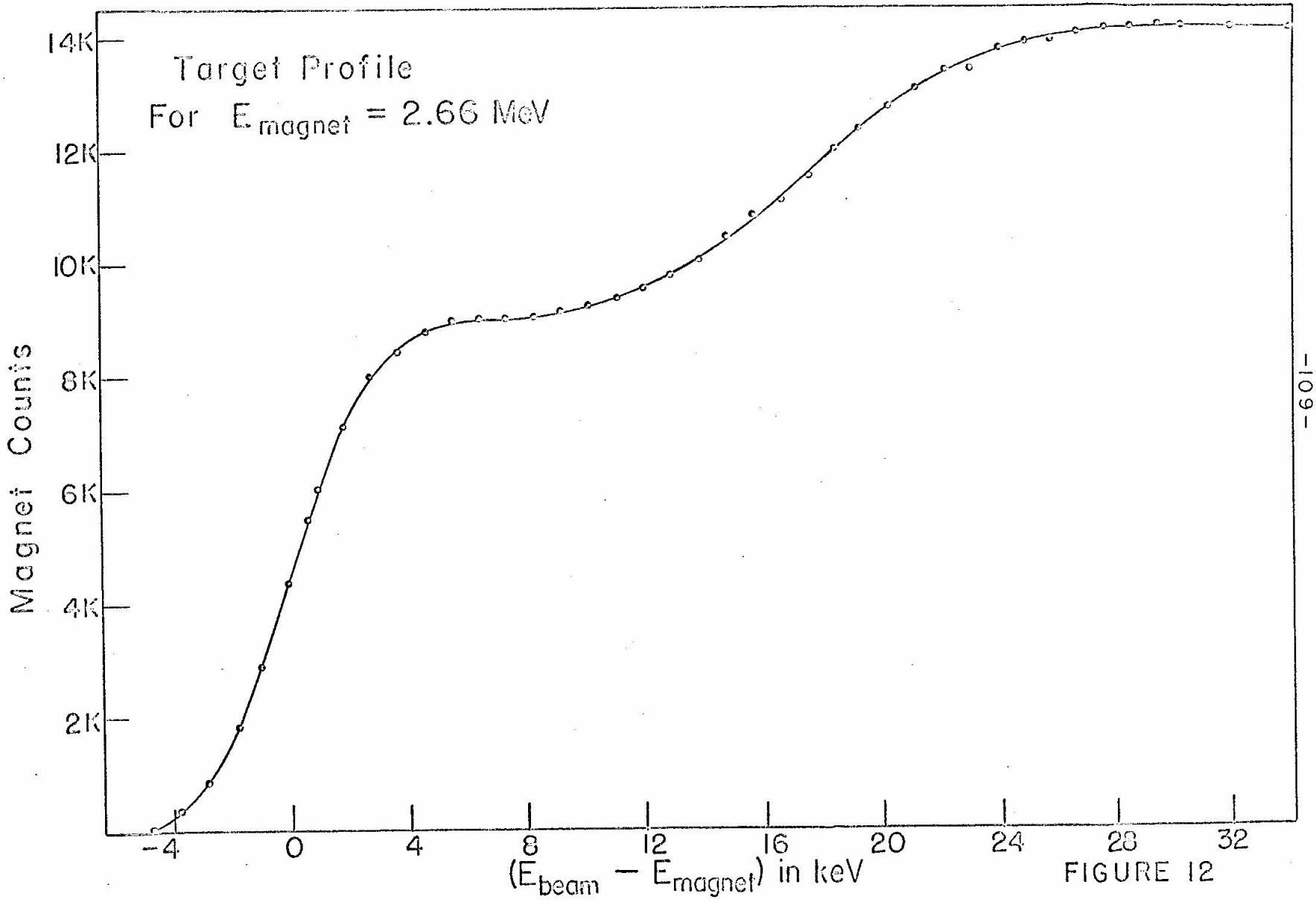
Target Profile
For E_{magnet} = 2.66 MeV
14K
12K
10K
8K
6K
4K
2K
Magnet Counts
-4
0
4
8
12
16
20
24
28
32
$(E_{beam} - E_{magnet})$ in keV

FIGURE 12

Figure 13. The oxygen composition--straggling function for the tungsten oxide target used to obtain the capture data. This function was determined for bombarding energies in the region of 2.66 MeV from an analysis of the scattering profile shown in Fig. 12. The function is defined in such a manner that if $\sigma(E'')$ is the capture cross section at the energy E" and K_2 is a constant giving the detection efficiency and the beam charge, then for a mono-energetic beam of energy E' the yield is given by:

$$Y(E') = K_2 \int_0^\infty f_o(E',E'')\sigma(E'')dE''$$

The function $f_o(E',E'')$ is explicitly dependent only upon the energy difference E' - E"; thus the horizontal scale in the figure is given in terms of this quantity. See text p. 67.

Figure 14. The function given by folding the function $f_o(E',E'')$ of Fig. 13 with the beam resolution of the magnetic analyser used to obtain the capture data; the resolution used in this folding was 3.0 keV (f.w.h.m.). The function is defined in such a way that to correct the theoretical expression for the capture cross section for the effects of the finite target thickness and beam resolution, it was only necessary to fold it with this function. Thus for a bombarding energy E_B:

$$Y(E_B) = K_2 \int_0^\infty t(E_B,E'')\sigma(E'')dE''$$

See text pp. 42, 67.

FIGURE 13

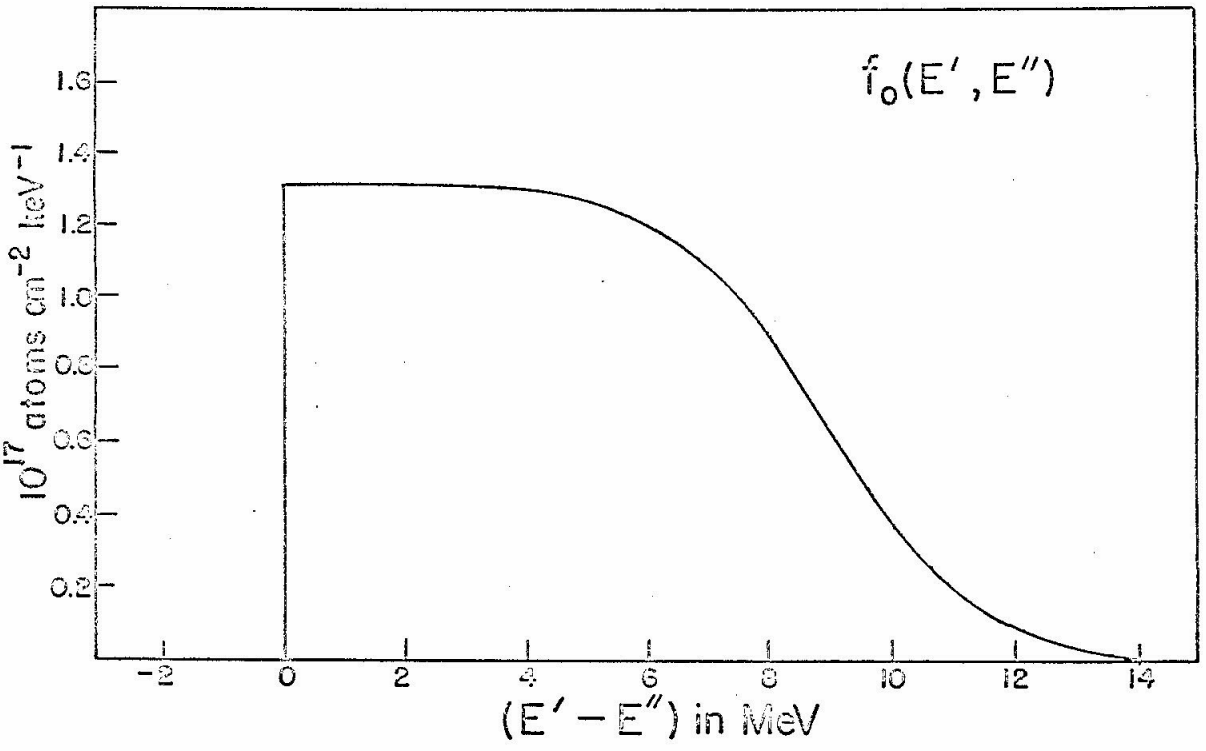

FIGURE 14

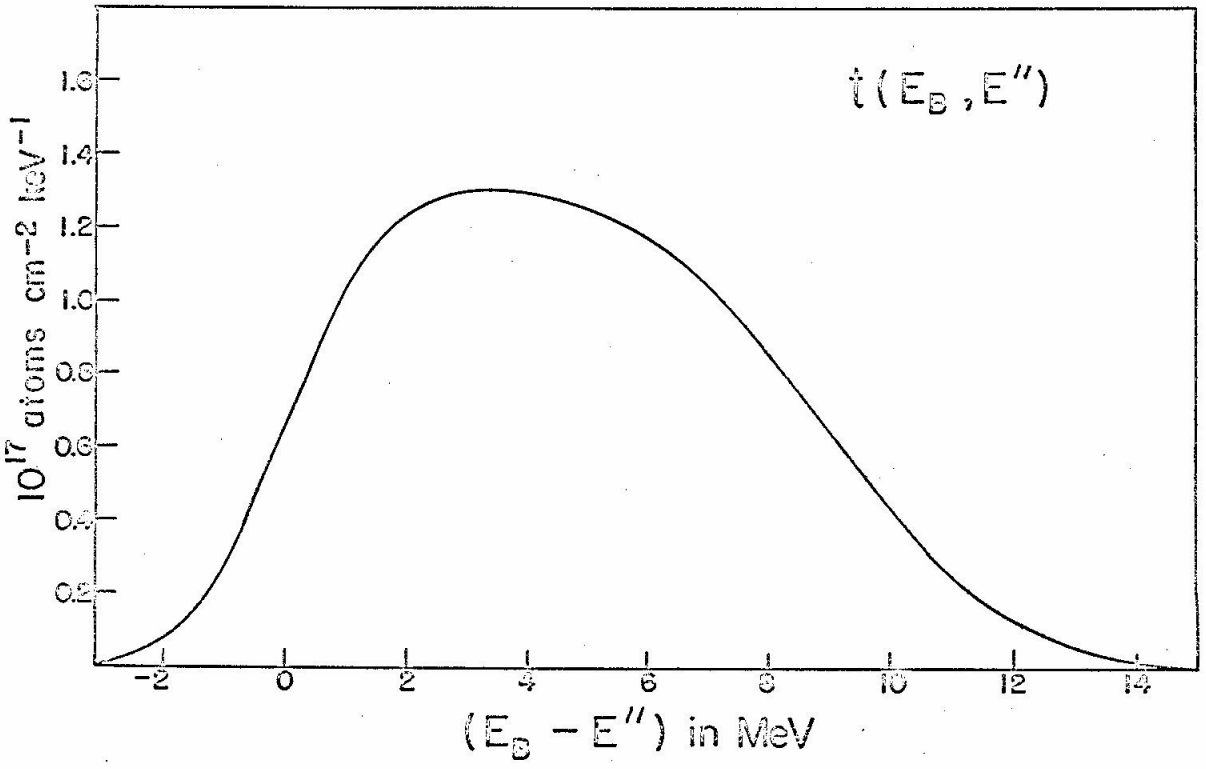

Figure 15. The spectral functions for γ_2 and γ_3 and the sum spectrum η_s resulting from the folding of η_{γ_2} with η_{γ_3}. For simplicity η_{γ_3} and η_{γ_2} have not been normalized to contain the same area; η_{γ_2} and η_s, however, have been normalized to contain equal areas. The sum spectrum η_s shown in the figure is valid only down to the dashed vertical line; beyond this point the rapid decrease in the dashed portion of η_s is due to the fact that only the limited portion of the γ_2 spectrum shown in the figure was folded with η_{γ_3} to obtain η_s. See text pp. 71, 72.

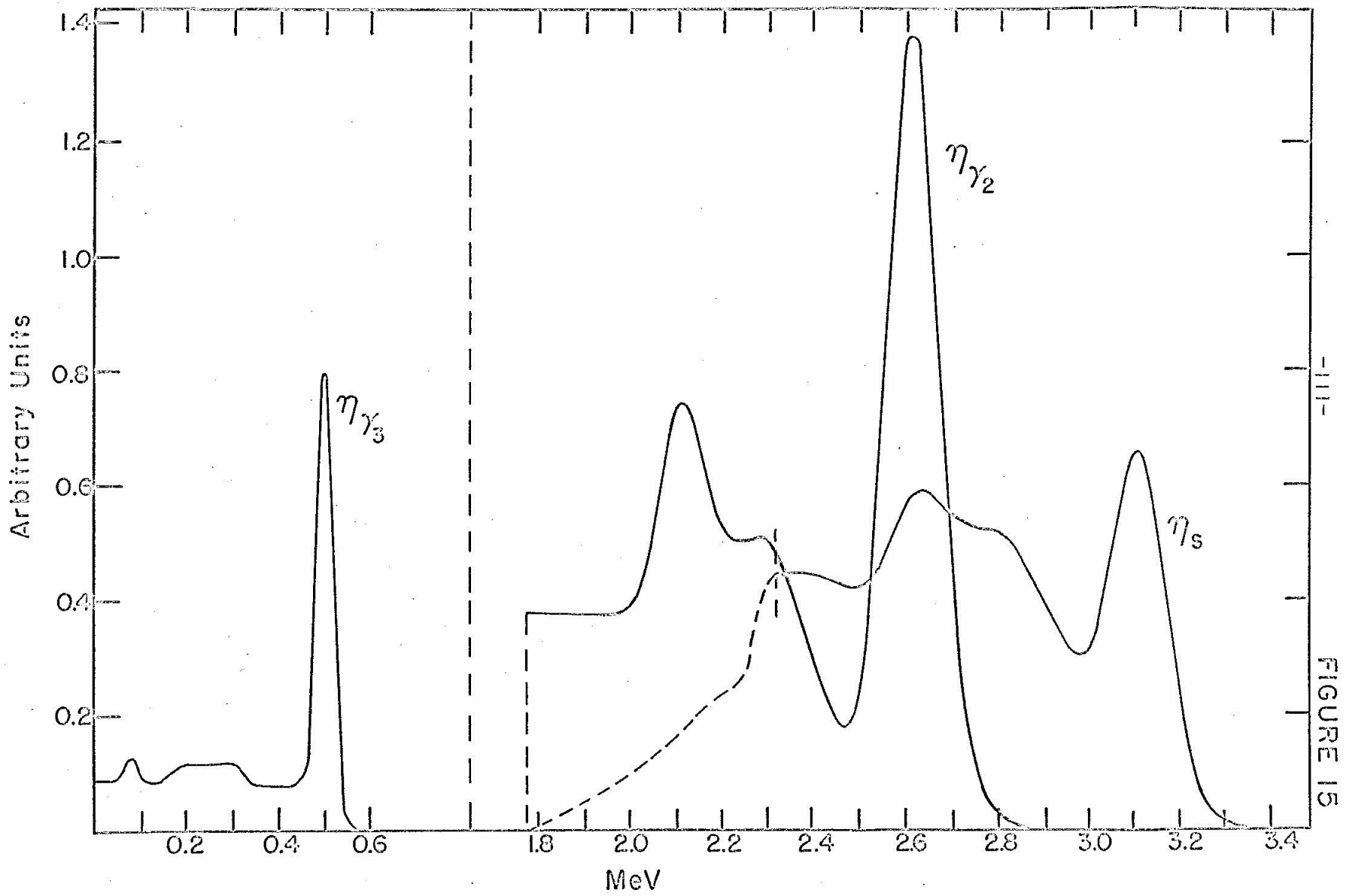
1.4
1.2
1.0
0.8
0.6
0.4
0.2
Arbitrary Units
η_{γ_3}
η_{γ_2}
η_s
0.2
0.4
0.6
1.8
2.0
2.2
2.4
2.6
2.8
3.0
3.2
3.4
MeV

FIGURE 15

Figure 16. Illustrates the method used to obtain the three ratios ρ, δ, and τ for the 3.51-MeV gamma ray from the $C^{12}(p,\gamma)$ reaction at the 1.698-MeV resonance. The interval ΔE in this case corresponds to the 11.7 channel interval shown between the two solid vertical lines. The Gaussian approximations to the photopeak and the first escape peak are shown in the figure as dashed curves, and the extrapolation of the flat Compton background into the ΔE interval is shown as the horizontal dashed line. ρ is given by the ratio of the number of counts lying within ΔE to the number of counts within the Gaussian approximation to the photopeak. δ is given by the ratio of the number of counts in ΔE due to the extrapolated flat Compton background to the number of counts in the Gaussian photopeak. τ is given by the ratio of the number of counts in the Gaussian first escape peak to the number of counts in the Gaussian photopeak.

See text p. 75.

FIGURE 16

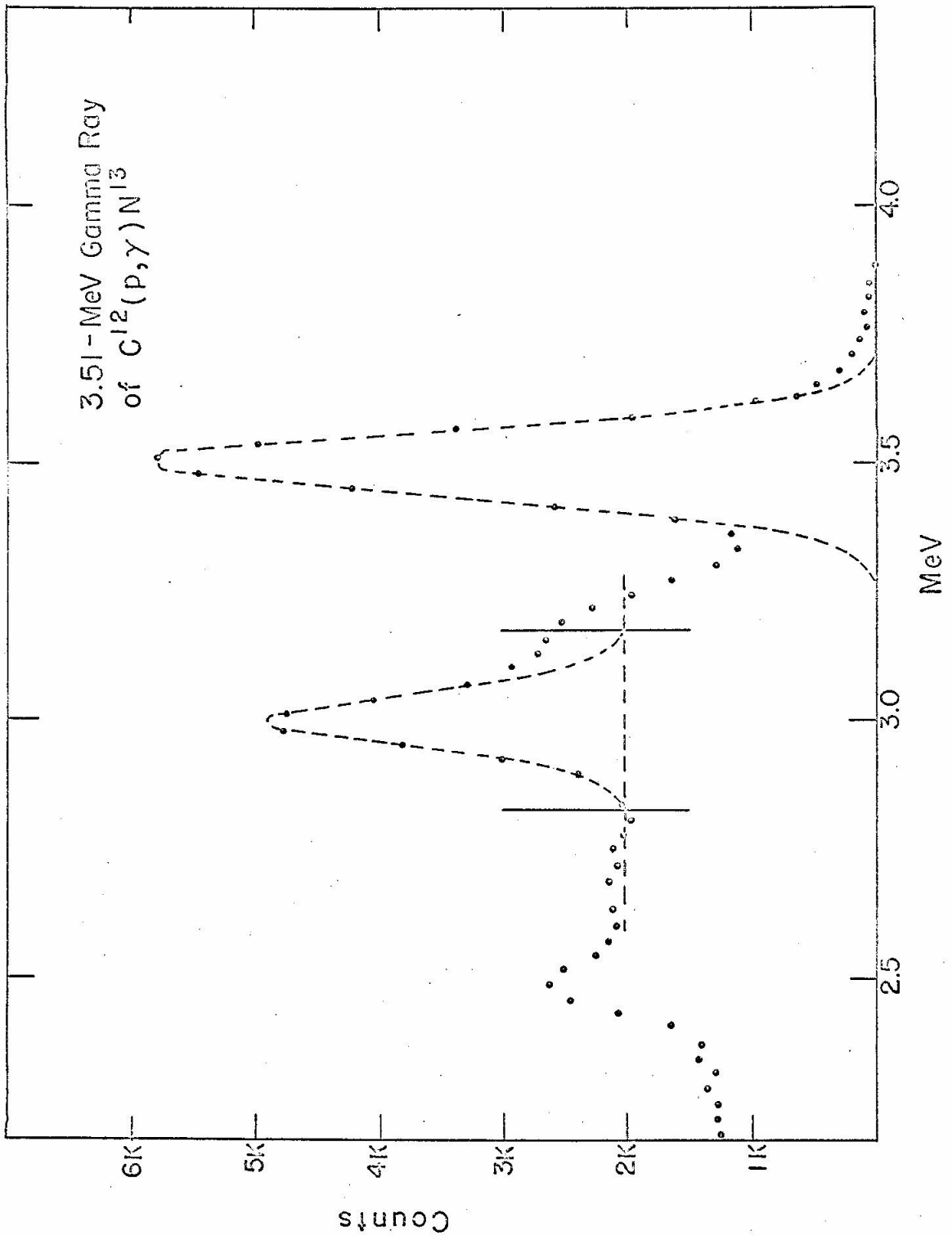
3.51-MeV Gamma Ray
of $C^{12}(p,\gamma)N^{13}$
Counts
6K
5K
4K
3K
2K
1K
2.5
3.0
3.5
4.0
MeV

Figure 17. The ratios ρ, δ, and τ as a function of the gamma ray energy. The definition of these three ratios is illustrated in Fig. 16 for the 3.51-MeV gamma ray of the $C^{12}(p,\gamma)$ reaction. The data points were obtained for the following gamma rays:

1.98-MeV γ of $O^{18}(p,p')$ at the 2.640-MeV resonance

2.365-MeV γ of $C^{12}(p,\gamma)$ at the .459-MeV resonance

2.615-MeV γ of a ThC" source (corrected for summing)

3.13-MeV γ of a S^{37} source

3.51-MeV γ of $C^{12}(p,\gamma)$ at the 1.698-MeV resonance

See text pp. 75, 77.

FIGURE 17

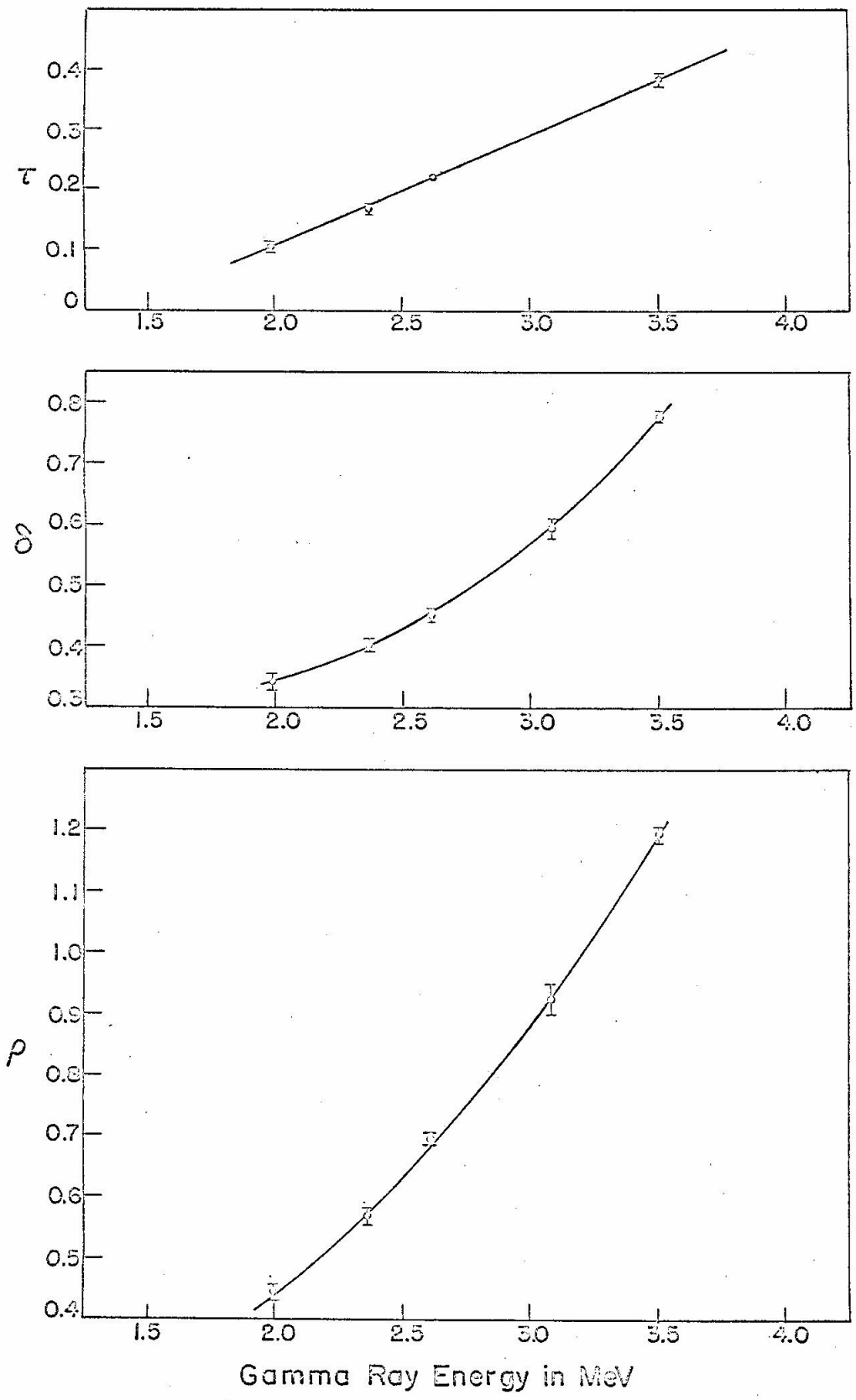
τ
0.4
0.3
0.2
0.1
0
1.5
2.0
2.5
3.0
3.5
4.0
σ
0.8
0.7
0.6
0.5
0.4
0.3
ρ
1.2
1.1
1.0
0.9
0.8
0.7
0.6
0.5
0.4
Gamma Ray Energy in MeV

Figure 18. Angular photopeak sensitivity of the detector as determined by the mapping with the 2.615-MeV gamma ray of ThC". The mapping was performed with the collimation channel in the plane defined by the beam axis and the central axis of the counter; the angle θ is the standard polar angle between the beam axis and the collimation channel. The number of photopeak counts obtained at a given angle θ is indicated by the vertical scale on the left. The error indicated on the data points is just that due to counting statistics. The background level due to the imperfect collimation is indicated by the dashed base line. The angular sensitivity function $\chi(\alpha)$ is given by the smooth curve drawn through the data points and the vertical scale on the right; the angle α is plotted along the top of the figure. See text pp. 82, 83, 84.

FIGURE 18

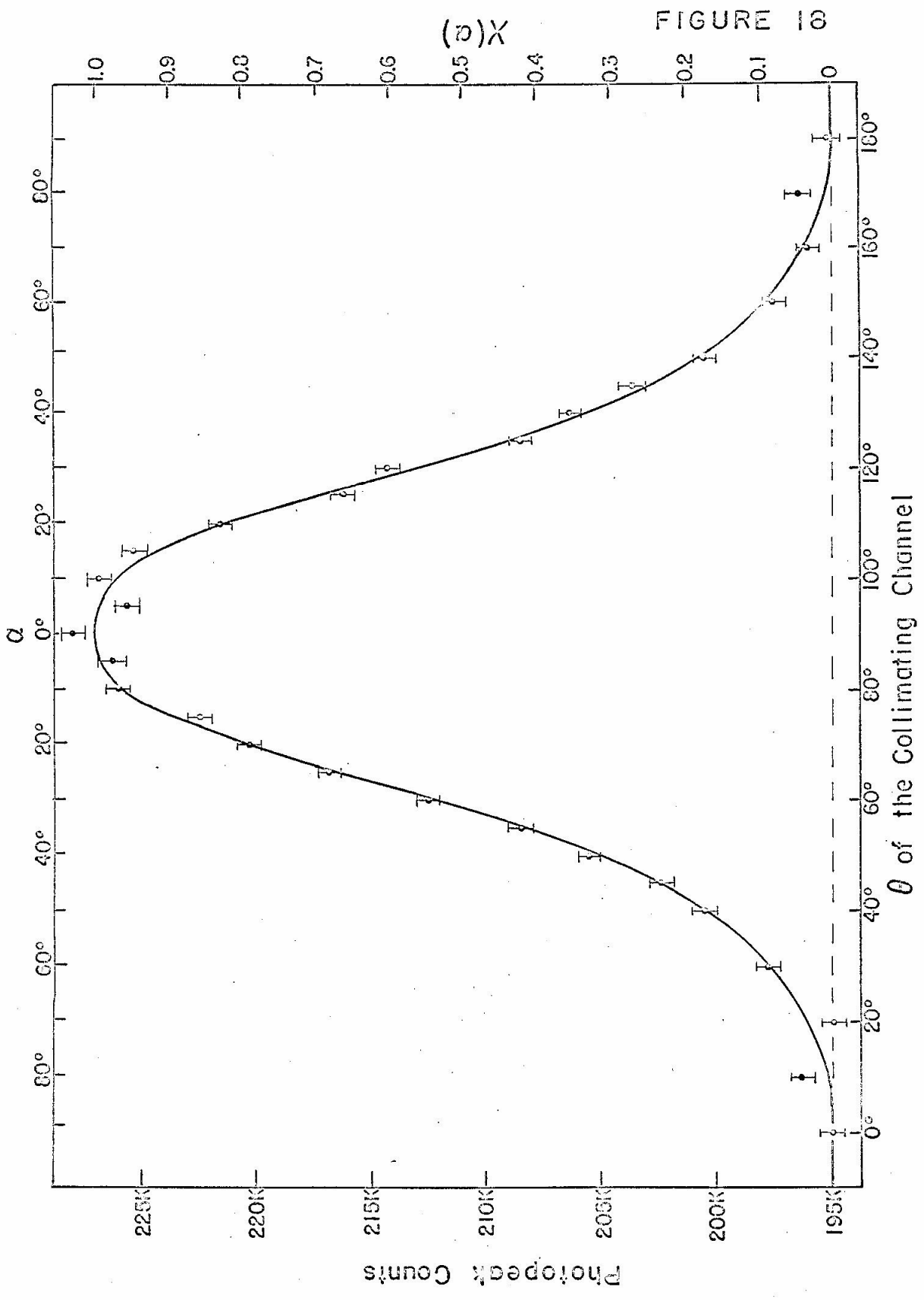
χ(α)
1.0
0.9
0.8
0.7
0.6
0.5
0.4
0.3
0.2
0.1
0
α
60°
40°
20°
0°
20°
40°
60°
θ of the Collimating Channel
0°
20°
40°
60°
80°
100°
120°
140°
160°
180°
Photopeak Counts
225K
220K
215K
210K
205K
200K
195K